Shock Wave Behavior of Particulate Composites

Thesis by

Michael B. Rauls

In Partial Fulfillment of the Requirements

for the Degree of

Doctor of Philosophy

California Institute of Technology

Pasadena, California

2015

(Defended May 4, 2015)

To Michael J. and Dorothy Rauls and Dominic Schiavone

"Just do the thing."

G. Ravichandran

Acknowledgments

The success I have found in my graduate career is due in no small part to the mentoring and assistance of a great many people. First and foremost of them is my advisor, Professor G. Ravichandran. I am very appreciative that he gave me the opportunity to dive into a project in which I had very little background and take my own time to learn and figure my way through. While it may have been slightly frustrating once in a while to run into issues in the lab only to be told to "try something," it was the best bit of advice or guidance I have ever gotten. After going through the research process, it may be more appropriate to say that I have a Ph.D. in the field of 'using things for something other than their intended purpose'. That must be the philosophy portion of the degree, and for leading me to that approach to problem solving, I am eternally grateful to Ravi. His life advice has also been quite enlightening, and I feel very privileged to have had the opportunity to get to know him. It is not an exaggeration to say that I would not have stayed to complete my thesis if I didn't have him as my advisor.

I also owe my gratitude to the members of my thesis committee who offered many positive suggestions and a multitude of great advice. Dr. Kaushik Bhattacharya helped me fine tune the experimental matrix I came up with to extract interesting pieces of information, which may eventually be useful to the modeling community. Dr. Dennis Kochmann was infinitely helpful in making sense of my simulation results and is personally responsible for my understanding of continuum mechanics. Dr. Christopher Neel was instrumental in my transition from undergrad race car mechanic to shock physicist. He took a lot of his time over the course of the summer of 2013 to be my mentor for my internship at Eglin Air Force Base. He explained in excruciating detail how to run a plate impact experiment, demonstrated what good data should look like, motivated me to take the extra time to

do things correctly in the laboratory, and answered my questions. If not for him, I'd still be making targets and not getting any results.

Dr. Lalit Chhabildas is the mastermind behind the Air Force's Center of Excellence, and is who motivated and promoted my work on shock in particulate composites. Seeing his dedication to the field of shock physics along with his encouragement during my internship at Eglin AFB was instrumental in getting me started in the field. It is his vision that graduate students and the Air Force laboratories should have more interaction and share in the research process — the sharing of knowledge was quite beneficial to myself, as well as the scientists I had the pleasure of working with. I very much appreciate the opportunity he set up for me to learn from the best, and try to pass on my results to those who could benefit from them.

Adam Iverson at NSTec graciously volunteered his time at conferences and on trips to Caltech to guide me in the fabrication of my PDV interferometer that I used to acquire all of my experimental data. I asked him for a quote one day to buy one, and he suggested I build my own. Ravi just told me to "Do the thing". After some consultation and a lot of reading, Adam helped me design and build a turn-key PDV system that actually worked the first time I turned it on, as well as the whole way through my thesis project with no drama. He saved me untold amounts of time and frustration, and for that I am grateful.

I would also like to thank Dr. Chris Lynch, Dr. Rod Clifton, Dr. John Borg, Dr. Wolfgang Knauss and Dr. Guillaume Blanquart for the conversations we had about shock physics, polymers, and grad school, and for their immense help in sorting out the problems that came up with unsurprising regularity. Petros Arakelian and Ali Kiani were a wealth of knowledge, and were always available if I had a complicated mechanical question or needed the confidence boost to just try something on the mill, lathe, or gun.

The Ravi group past and present has been an immense help both in my research as well as outside of the lab. Dr. Jacob Notbohm, Dr. Christopher Kovalchick, Dr. Shuman Xia, Dr. Justin Brown, and Dr. Mike Mello were instrumental in preparing me early on in my graduate career with fantastic discussions, advice, and group philosophy. It was also a pleasure to work along side my

fellow group members: Matt Newman, Zach Sternberger, Laurence Bodelot, Aaron Albrecht, Aaron Stebner, Owen Kingstedt, Nikhil Karanjgaokar, Stan Wojnar, Victoria Stolyar, and Kristen John. Cheryl Gause kept me sane with her guidance in administrative and travel matters, as well as being around to chat when I should have been working.

I would like to thank my friends and family for sticking with me through the good and bad times that accompany the research process. In particular, I owe a large debt of gratitude to my parents, P.C. MacDonald, Philip Arnold, Reeve Dunne, Esteban Hufstedler, Oliver Shafaat, Jeff LaJeunesse, and Merit Schumaker. Having them around for consultation, conversation, softball, mountain bike riding, and general mayhem got me to a point at the end where I could genuinely say that every new day was better than the last.

Finally, I would like to acknowledge my funding sources — especially that from the Air Force Research Laboratory Center of Excellence in High-Rate Deformation Physics of Heterogeneous Materials for their generous material and technical support. I would also like to acknowledge the Department of Defense (DoD) through the National Defense Science & Engineering Graduate Fellowship (NDSEG) Program.

Abstract

Material heterogeneity at some scale is common in present engineering and structural materials as a means of strength improvement, weight reduction, and performance enhancement in a great many applications such as impact and blast protection, construction, and aerospace. While the benefits of transitioning toward composites in practical applications is obvious, the methods of measurement and optimization required to handle spatial heterogeneity and bridge length scale differences across multiple orders of magnitude are not. This is especially true as loading rates transition into the shock regime. Composite materials, such as concrete, have advantages afforded to them by their microstructure that allow them to dissipate and scatter impact energy. The mechanical mismatch between constituent phases in composites (mortar and cement paste in concrete, crystals and binder in polymer bonded explosives, ceramic powder and epoxy in potting materials, etc.) provides the interfaces required for shock wave reflection. The degree to which a shock is disrupted from its accepted form as a propagating discontinuity in stress and particle velocity is highly dependent upon the size, shape, and density of the interfaces present.

The experimental and computer aided simulations in this thesis seek to establish a scaling relationship between composite microstructure and shock front disruption in terms of particulate size and density through the use of multi-point heterodyne velocity interferometry. A model particulate composite has been developed to mimic the wave reflection properties of materials such as Ultra High Performace Composite (UHPC) concrete and polymer bonded explosives, while also being simple to source and manufacture repeatably. Polymethyl Methacrylate (PMMA), a thermoplastic polymer, and silica glass spheres satisfy the manufacturing constraints with a shock impedance mismatch of 4.1, when placed in-between the shock impedance of UHPC concretes (~ 10) and polymer bonded

explosives (~ 2). The flexibility afforded by the model composite allows for the use of mono-disperse bead particle diameter distributions centered at 5 discrete diameters centered in the range associated with high scattering effectiveness (5-50 times the shock thickness in the pure matrix material). Shock front disruption is measured at multiple points on the rear surface of a plate impact target to observe shock spreading and spatial heterogeneity in material response due to random particle placement.

Shock rise times are reported for composites of 30% and 40% glass spheres by volume, with glass spheres of 100 μm, 300 μm, 500 μm, 700 μm, and 1000 μm diameter. Composites with single mode as well as bi-modal bead diameter distributions are subjected to plate impact loading at an average pressure of 5 GPa. In single mode composites, a linear dependence of shock wave rise time on particle diameter is observed, with a constant of proportionality equal to the bulk shock speed in the material. Bi-modal bead diameter composites were fabricated in order to achieve higher volume fractions without composite degradation. The addition of a second phase to a base 30% glass by volume composite mix results in significant increases in shock wave rise time for base mixes of 500 μm beads, while a point of maximum scattering effectiveness is observed for base mixes of 1000 μm.

A comprehensive two dimensional series of CTH hydrocode simulations has been completed in tandem with experiments. An evaluation of the discrepancies in simulation and experimental results is presented. Shock disruption mechanisms and matrix/interface damage effects are discussed as possible sources of error and potential avenues for model improvement. The scaling arguments and model deficiency corrections made in this thesis have the potential to drive the development of new approaches of modeling shock waves in heterogeneous materials as well as optimization of microstructure for maximum shock front disruption.

Contents

List of Figures

List of Tables

Chapter 1

Introduction

1.1 Background

Shock waves and high pressure phenomena are a common occurrence, both in scientific situations and nature [17] [13]. Structures designed for habitation and transportation are often subjected to shock and blast loading, both intentionally and unintentionally. Automobile accidents and the use of military hardware generate high pressures within the components of these structures at extremely high strain rates. Further, remotely operated vehicles could be subjected to high pressures. Understanding geologic materials and elements in planetary formation processes is also critical to the development of other man-made high pressure projects such as fusion for energy generation. These problems span many orders of magnitude in pressure, strain rate, and system size.

The most common impact phenomena that the average person will witness in their lifetime is an automobile accident. In the most extreme case of a wreck at highway speeds of 65 miles per hour (60 $^{m}/_{s}$), characteristic wave interaction times are in the 10's of milliseconds (10^{-3} s) to seconds and pressures in structural materials can reach up to approximately 1 GPa. As applications move away from those encountered in the civilian world to those found in military and defense situations, the time scales that characterize wave propagation decrease, and pressures can be higher. Ballistic impact and blast are common in war zones. Small arms projectiles and armor interactions, blast wave and building interactions, and kinetic penetrator and bunker interactions are characterized by stresses in the range of 1 - 10 GPa, with events lasting in the 10's of microseconds (10^{-6} s). Typical

ballistic impact speeds of 1 - 2 $^{km}/_{s}$ and blast wave speeds up to 6 - 10 $^{km}/_{s}$ are required to generate these pressure levels.

Pressure levels and impact velocities only increase as one leaves the surface of the earth. Pressures at the center of the earth approach 350 GPa at very high temperature. The phase and properties of the iron core and other geologic materials at this pressure are unknown [57]. Planetary impacts may generate such extreme pressures as well, with typical impact speeds of 5 - 10 $^{km}/_{s}$ for micro and normal meteorites, and up to 20 - 50 $^{km}/_{s}$ in the case of interplanetary impacts and comet strikes.

Generating such extreme pressures in the laboratory to characterize materials or optimize their performance under high pressure loading is difficult, and requires specialized equipment. In the static loading regime, diamond anvil cells are used. Diamond anvil cells use cut and polished diamond surfaces, typically 1 mm^2 in area in a loading frame made to be as rigid as possible. The high elastic modulus and yield strength of the perfect crystal diamond anvils allows for static generation of up to 600 GPa in extremely small samples. The diamond anvil compression loading technique is adequate for homogeneous materials, but is not amenable to the study of composite materials with length scales of any appreciable size, nor does it allow for the study of wave propagation.

To that end, larger samples may be characterized at high pressures by accelerating projectile plates at target plates and monitoring the response using a variety of guns and electro-magnetic accelerators. These facilities are capable of applying high pressure, but also generate extremely high strain rates and are limited in the duration of time that the high pressure state can be maintained. Larger and multi-stage guns are required to increase the pressure magnitude and pulse duration. At the university level, single-stage gas guns, propellant guns, and two-stage light gas guns are commonly used in high pressure research. Single stage gas guns are capable of impact velocities up to approximately 1 $^{km}/_{s}$. Higher velocities and larger, more massive projectile assemblies require the use of propellant guns. Projectiles of approximately 100 g may be accelerated to 1 - 2 $^{km}/_{s}$ in this manner. Two stage stage gas guns employ sequential high pressure reservoirs filled with a light gas to drive 2 - 4 in (50 - 100 mm) diameter projectiles at velocities from 2 - 7 $^{km}/_{s}$.

If the pressures encountered in planetary collisions are desired, gas guns with additional stages can

be fabricated to drive projectiles. At some point, accelerating massive projectiles becomes cost and capability prohibitive. Electromagnetic shock generation mechanisms may be employed to generate high pressure shock waves without accelerating projectiles. In laser driven shock experiments, an ablator is vaporized with a short duration high energy laser pulse, and the expanding gasses generate a force on the surface that drives a stress wave into the target material. Pressure pulses may be shaped by modifying the pulse shape and duration of the incident laser beam [33]. At the highest pressure levels required for nuclear fusion research, electromagnetic compression of test specimens is undertaken at facilities like the Z-Machine at Sandia National Laboratories. A massive bank of capacitors is discharged onto the surface of a cylindrical specimen in the presence of a magnetic field. The induced electromagnetic force then implodes the cylinder, reaching particle velocities of 20 - 60 $^{km}/_{s}$ [32]. While the velocities and pressures attainable are extremely high, the experiments at these states are again limited in size and loading duration.

The goal of driving materials to high pressures is to characterize the state of pressure, temperature, and other thermodynamic properties. Special loading geometries such as the plate impact configuration allow scientists to make assumptions about the stress state in the target so that difficult to measure material state variables may be estimated [17]. In shock wave experiments, the states accessible for a given loading magnitude define a specific material dependent relationship called a Hugoniot. Measurement of the Hugoniot state is typically completed in pressure and/or velocity space.

1.2 Motivation

The focus of this study will be in the range of strong shock waves, but in the pressure range proscribed by ballistic impact phenomena and blast, where shock wave interaction and reflection drive the bulk material response. Since the bulk of construction and structural materials in use at present may be considered highly heterogeneous, it is critical that the impact response of these materials as a function of their level of heterogeneity is well understood. The model system in this study is based on concrete, and other particulate composite materials of similar constitution. These materials

are characterized by the presence of hard, high modulus inclusions embedded in a relatively soft, compliant substrate. Other materials that share these characteristics in common use are potting compounds for electronic devices subjected to shock loading as well as high explosives.

The inclusions vary in size from 100 μm for Ultra High Performance Composite (UHPC) concretes [63] up to 10's of mm in mean particle diameter for the coarser grades of concrete [39] [54] [55]. It is clear from the examination of the previous examination of shock wave propagation in composites that the size and number density of inclusions control the shock wave structure as it propagates into the composite, as well as the resulting Hugoniot state. Due to the difficulty in fabricating many of the above composites, a single model particulate composite has been developed as a repeatable stand-in. The model particulate, its fabrication process, and mechanical properties are described in Section 3.1. The composite system property chosen to enforce similarity between the various engineering materials and the model composite is the shock impedance mismatch ratio, R, of the constituent materials [26]. The impedance mismatch ratio of the materials of interest falls within the range of 2 - 10 [18] [61].

The shock impedance mismatch ratio determines the amount of energy reflected at each interface that a stress wave encounters as it propagates into a composite medium. For composites with R values described above, up to 40% - 60% of the incident energy may be reflected [26]. When the high interface densities of concrete and polymer bonded explosives are considered, it is clear that wave reflections and scattering at interfaces dominate the shock wave structure development. It is therefore desirable to employ wave scattering to maximize shock front disruption and lower particle acceleration in composite defensive structures such as armor and bunkers.

Changing impedance mismatch in engineering composites may not be possible due to chemical constraints and material availability; however, particle size and density are readily tunable. Previous work in the composite area has focused mostly on Hugoniot response of composites with small particulates (potting compounds) or composites with large, poly-disperse inclusion diameter distributions (polymer bonded explosives and concrete). Isolating the particle size dependence on shock front disruption is therefore critical to future tuning of particulate composites in engineering practice.

A model composite has been developed to mimic the interface properties of the materials of interest while being simple to manufacture repeatably with no settling or agglomeration of the particulates. The choice of materials for the model composite allows for the precise tuning of the particle size without sacrificing particle distribution. Silica glass spheres and polymethylmethacrylate (PMMA) powder mix evenly across all diameters used. Furthermore, the use of glass spheres simplifies the composite geometry for modeling and length scale determination.

An overview of the theory of shock wave propagation in solids is presented in Chapter 2. The conservation equations (mass, momentum, and energy) are discussed to provide insight into the choice of the experimentally observed quantities, as well as methods for estimating shock pressure states. Previous experimental and simulation based work on particulate composites is also presented. Hugoniot determination is discussed for polydisperse particulate size distributions, and for composites with small particle diameters.

Chapter 3 describes the model particulate composite designed to fill space left open by the previous work: low impedance mismatch composites with monodisperse particle diameter distributions up to 1 mm mean diameter. Compression molding and heat treating techniques are discussed. The composites are prepared and loaded in a powder driven plate impact facility described in Section 3.2.1. Rear surface particle velocity time histories during impact loading are extracted with heterodyne velocimetry. Interferometry theory and error analysis conclude Chapter 3.

Lagrangian shock hydrocode simulations were performed in order to improve experiment planning and offer additional insight into the underlying physics of wave propagation in composites. The simulation models, parameters, and geometries are presented in Chapter 4.

The shock structure dependence on particulate volume fraction and mean diameter is examined and a quantitative statistical representation of the degree of shock front disruption is presented in Chapter 5. Composites with volume fractions of 30% and 40% particulate with mono-disperse diameter distributions averaging 100, 300, 500, 700, and 1000 μm were subjected to plate impact loading to pressures of approximately 5 GPa. Wave profiles are presented and shock thickness analysis have been performed in Section 5.1.2.2. The scaling of shock front thickness as a function

of mean particle diameter is discussed.

More complex composites were fabricated with bi-modal bead diameter distributions in order to gauge the effectiveness of current shock hydrocode simulations and offer insight into the shock wave response of materials with polydisperse particulate diameter distributions. Rise times and wave structures are examined in Section 5.2. Examination of the shock wave response of these controlled composite geometries may allow for faster optimization of the microstructure of materials used in protective applications.

Chapter 2

Background: Theory and Prior Work

2.1 Shock Waves

The study of shock waves is nearly synonymous with the study of impact. Impact response is primarily wave dominated and results in damage to a structure, or its constituent materials. While the end result of an impact is obvious — twisted metal, fragments, and craters — the underlying phenomena that dominate these effects are not well understood. Understanding the initial wave pulse generated by impact or blast is critical to understanding the final outcome. While it may seem like an oversimplification of real world impact problems to focus on a plate impact problem, isolating the material microstructural effects on wave propagation is fundamental to understanding the effect of impact events [38]. At high rates of deformation, the waves generated by impact events can be considered as shock waves — propagating discontinuities of pressure, particle velocity, and density [17] [13]. The propagation speed of shock fronts is generally faster than the bulk sound speed associated with elastic waves. This chapter covers the basic principles of impact and the mechanics used in the analysis of experimental data in this study.

2.1.1 Normal Shock Jump Equations

Before characterizing the structure and disruption of shock waves in heterogeneous materials, it is important to understand the relationship between the shocked and unshocked states of a material

for a given pressure. The relationships between shocked and unshocked states are known as shock jump conditions, and can be derived from the conservation laws of mass, momentum, and energy. Jump conditions are generated by considering the kinematic restrictions imposed by the assumption of a 1D plate impact geometry. We may "monitor" the deformation of a deformable body (target plate or half space for simplicity) as a collection of material configurations (positions, velocities, stresses, etc.) as a function of time after impact [17]. We assume an initial pre-impact configuration and call it the reference configuration, with the material particles occupying coordinates defined by $\mathbf{X}$, in a cartesian coordinate frame. Bold symbols or subscripts (Einstein notation) indicate vector or tensor quantities, and are used interchangeably. Quantities in the reference configuration have capital indices, while deformed configuration indices are in lower case. When the body is deformed, a mathematical mapping of the material in the reference state to a later deformed configuration is described with the functions $\mathbf{x}$ as follows in Equation 2.1 and illustrated in Figure 2.1:

$$\mathbf{x} = \mathbf{x}(\mathbf{X}, t) \tag{2.1}$$

The deformation mapping gives the location in space, $\mathbf{x}$, at a given time of a particle originally at

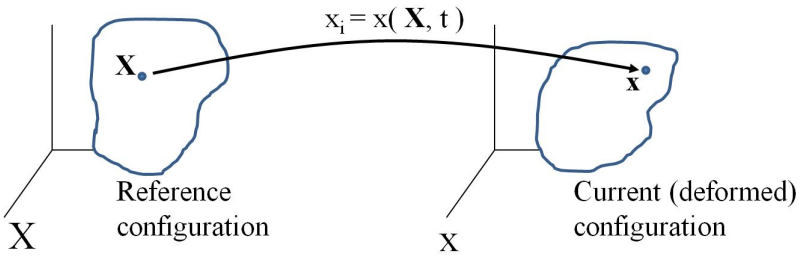

Figure 2.1: Deformation mapping of a reference configuration to a deformed configuration.

position $\mathbf{X}$ in the reference configuration. This description of motion is also known as the material, or Lagrangian reference frame, and follows what happens to a specific particle. If we desire to know what is happening at a specific point in space, we may write our equations in terms of $\mathbf{x}$:

$$\mathbf{X} = \mathbf{X}(\mathbf{x}, t) \tag{2.2}$$

The relationship between the two reference frames can be examined in differential form, as the change of a line element d$\mathbf{X}$ is deformed into its current shape d$\mathbf{x}$ in the current configuration:

$$d\mathrm{x}_i = F_{iJ} dX_J \tag{2.3}$$

The quantity $\mathbf{F}$ is defined as the deformation gradient. If no deformation occurs, $\mathbf{F}$ is the identity tensor. The deformation near a point $\mathbf{X}$ is entirely described by the deformation gradient. A second useful form for describing the deformation is the right Cauchy Green tensor, with components C_{IJ}:

$$C_{IJ} = F_{iI} F_{iJ} \tag{2.4}$$

The right Cauchy Green tensor is symmetric. Volume changes may be quantified by examining the change in volume of an infinitesimal triad to a parallelopiped in the deformed configuration. The change in volume from the reference to the deformed configuration is given by:

$$\frac{dv}{dV} = J = det(\mathbf{F}) \tag{2.5}$$

In impact phenomena, time dependent deformations are required to compute stresses and analyze mechanical processes. In the case of planar impact and shock propagation, the deformation may be described in the Lagrangian form by the following:

$$\mathrm{x}_1 = X_1 + U(X_1, t),\ \mathrm{x}_2 = X_2,\ \mathrm{x}_3 = X_3 \tag{2.6}$$

Geometry and coordinates are as follows: X_1 coincides with the direction of motion of the flyer plate and subsequent displacement, with a corresponding orthongonal basis of unit vectors $\mathbf{e}_i$. The x_2 and x_3 axes are also coincident, as shown in Figure 2.2. As expected from examining the plate impact "experimental" set up, a particle at location $\mathbf{X}$ is displaced from its original position at time $t = 0$ by an increment U in the positive x_1, or down range, direction. Equation 2.3 is used to obtain the

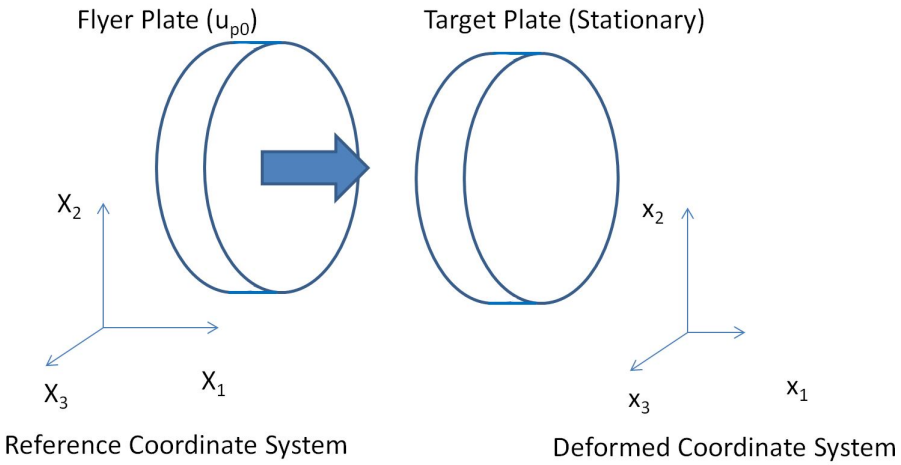

Figure 2.2: Coordinate system description in the context of a plate impact experiment.

deformation gradient, $\mathbf{F}$:

$$\mathbf{F} = \begin{bmatrix} 1 + \frac{\partial U(X_1,t)}{\partial X_1} & 0 & 0 \\ 0 & 1 & 0 \\ 0 & 0 & 1 \end{bmatrix} \tag{2.7}$$

In the present coordinate system, the deformation is described in the principal directions. If an alternate coordinate system is used it is evident that the material is sheared as it is also compressed. Due to the symmetry of the planar impact problem, the directions of maximum shear lie on planes 45˚ to the x1 direction. A closer examination of the material stress state is therefore warranted.

Traction is defined as a force per unit area, $\mathbf{T}$ on a plane passing through a point $\mathbf{x}$. The plane is described by its normal vector, $\mathbf{n}$. Information about the stress state on any plane passing through $\mathbf{X}$ is contained in the second Piola-Kirchhoff stress tensor, T_{IJ}. Extraction of the tractions is simply:

$$T_i(\mathbf{X}, t) = T_{IJ} n_J \tag{2.8}$$

From this, the pressure seen by a material under stress can be defined as:

$$p = -\frac{1}{3} T_{II} \tag{2.9}$$

Summation is implied by the repeated indices. Due to the symmetry of the loading, the stress tensor

has the following form:

$$\sigma = \begin{bmatrix} T_{11} & 0 & 0 \\ 0 & T_{22} & 0 \\ 0 & 0 & T_{22} \end{bmatrix} \tag{2.10}$$

The maximum shear stress is given by one half of the difference of the principal stresses.

$$\tau_{max} = \frac{1}{2}(T_{11} - T_{22}) \tag{2.11}$$

While it is important to understand the role of material strength in impact studies, the value of τ_{max} in the present study is generally so low as to be negligible. The shear stress is typically on the order of the yield stress in the material of interest (tens of MPa for polymers), while the material is loaded to pressures of several GPa — a difference of three orders of magnitude. Consequently, shear stresses will be neglected in the following analysis.

In the plate impact experiment, a flyer plate (or half space to simplify the analysis by neglecting unloading waves from the edges) with normal $\mathbf{e}_1$ strikes the target plate with initial velocity $u_{p0}\mathbf{e}_1$. All particle motion is then constrained to the $\mathbf{e}_1$ direction, as described above by the deformation gradient, $\mathbf{F}$. The impact drives a shock wave into the target, which can travel faster than the speed of sound in the material. At sufficiently high loading rates, these shock waves can be thought of as moving discontinuities of pressure, particle velocity, and density [17]. Initially, we will make several assumptions to aid analysis of shock waves:

1. Analyze shocks as continuous waves as their rise time becomes arbitrarily small [28];

2. Assume that shock waves travel at a constant speed, U_s, once their structure develops [17];

The Rankine-Hugoniot Jump conditions define the possible thermodynamic states that may be reached across a shock that meet the constraints set by mass, momentum, and energy conservation laws [13] [17] [28]. The jumps in stress, strain, particle velocity, and energy will be the variables in this analysis. The kinematic shock jump condition is derived from the continuity of displacement across a planar propagating shock front. This is equivalent to starting from the conservation of mass

formulation. Variables would simply be in terms of specific volume as opposed to strain.

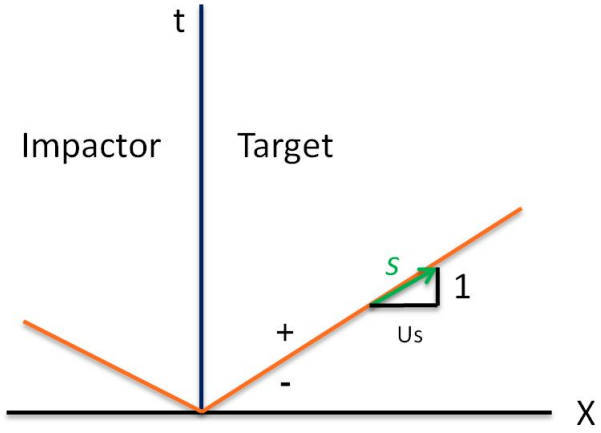

Figure 2.3: X-t diagram for a 1D planar plate impact.

Figure 2.3 shows the distance (X) - time (t) diagram for a flyer plate (impactor) striking a target plate. When the two plates collide at X=0, shock waves propagate into both the flyer and target plates. As time passes after impact at t=0 the wave front location, demarcated by the orange lines, advances into the two plates. Material below the shock front line (-) is undisturbed and its state given by the initial conditions, while the material above the line (+) is compressed. Let the function $\mathbf{U}(\mathbf{X}, t)$ be the displacement of a particle originally at point $\mathbf{X}$ in the reference configuration at a time t. The displacement, $\mathbf{U}$, is continuous across the shock front [17]. Define the coordinate system s that contains the points along the shock front. Material continuity immediately on each side of the shock front then gives:

$$\mathbf{U}^{+}(\mathbf{X}(s), t(s)) = \mathbf{U}^{-}(\mathbf{X}(s), t(s)) \tag{2.12}$$

We demand continuity everywhere along the shock front and for all time, so the above may be differentiated with respect to the shock front, s:

$$\frac{d\mathbf{U}^{+}}{ds} = \frac{d\mathbf{U}^{-}}{ds} \tag{2.13}$$

which can be expressed as a total derivative:

$$\frac{\partial \mathbf{U}^+}{\partial \mathbf{X}}\frac{d\mathbf{X}}{ds} + \frac{\partial \mathbf{U}^+}{\partial t}\frac{dt}{ds} = \frac{\partial \mathbf{U}^-}{\partial \mathbf{X}}\frac{d\mathbf{X}}{ds} + \frac{\partial \mathbf{U}^-}{\partial t}\frac{dt}{ds} \tag{2.14}$$

and leads to:

$$\frac{\partial \mathbf{U}^+}{\partial \mathbf{X}}\frac{d\mathbf{X}}{dt} + \frac{\partial \mathbf{U}^+}{\partial t} = \frac{\partial \mathbf{U}^-}{\partial \mathbf{X}}\frac{d\mathbf{X}}{dt} + \frac{\partial \mathbf{U}^-}{\partial t} \tag{2.15}$$

The differential quantities above are none other than the scalar definitions for strain, particle velocity, and shock velocity when the assumptions of one-dimensional strain are applied:

$$\begin{aligned} \frac{\partial \mathbf{U}}{\partial \mathbf{X}} &= \epsilon \\ \frac{d\mathbf{X}}{dt} &= U_s \\ \frac{\partial \mathbf{U}^-}{\partial t} &= u_p \end{aligned} \tag{2.16}$$

In the following expressions, jump notation will be used. The difference between the magnitude of the quantity post shock minus the magnitude pre-shock will be denoted with $[\cdot]$. Then,

$$[\epsilon]U_s = [u_p] \tag{2.17}$$

The next condition to consider is the one that arises from the conservation of momentum across a shock front. A control volume containing the shock front must be created, as shown in Figure 2.4. The conservation of momentum for a body enclosed in a volume V_0 can be written:

$$\iiint_{V_0} \mathbf{b}\rho_0 \,\mathrm{d}V_0 + \iint_{A_0^+ + A_0^-} \mathbf{T}^0 \cdot \mathbf{n}_0 \,\mathrm{d}A_0 = \frac{d}{dt}\iiint_{V_0} \rho_0 \mathbf{v}(\mathbf{X}, t) \,\mathrm{d}V_0 \tag{2.18}$$

Equation 2.18 is nothing more than Newton's Second Law for a control volume in a continuum solid. $\mathbf{b}$ is the body force acting on the mass contained in the volume V_0, $\mathbf{T}^0 \cdot \mathbf{n}_0$ is the traction acting on the planes A_0, and ρ_0 is the density of the undeformed solid, while $\mathbf{v}$ is the velocity in the infinitesimal volume element dV_0. The derivative of a changing quantity ($\mathbf{f}(\mathbf{X}, t)$) inside of a volume

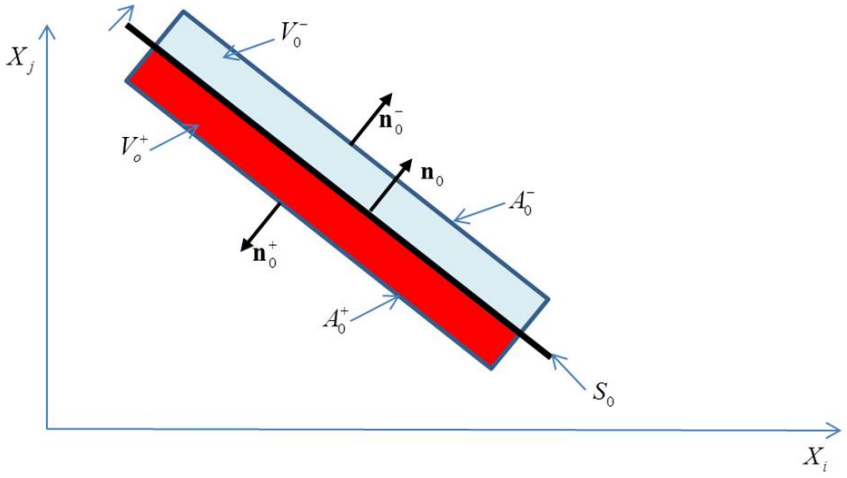

Figure 2.4: Control volume construction for moving shock front. Adapted from [28].

integral can be rearranged using the Reynolds' transport theorem [7]:

$$\iiint_{V_0} \mathbf{f}(\mathbf{X},t)\,\mathrm{d}V_0 = \iint_{S_0} (\mathbf{f}^+(\mathbf{X},t) - \mathbf{f}^-(\mathbf{X},t))U_s\,\mathrm{d}S_0 = \iint_{S_0} [\mathbf{f}]U_s\,\mathrm{d}S_0 \tag{2.19}$$

The terminology is identical to that used in Equation 2.18. The right hand side of the Reynolds' transport theorem is obtained when the thickness of the cylinder making up the control volume is shrunk to zero. Volume integrals disappear, and all that remains are the areas A_0 on the + and - sides of the moving interface. For convenience, the speed of the moving interface is labeled U_s for ease of comparison to a shock front. The shrinking volume limit may then be applied to Equation 2.18. Body forces can be disregarded as volume is sent to zero, the tractions on the surfaces parallel to the shock front remain and approach S_0, and the time varying volume integral can be rewritten as a jump in the velocity associated with the volume element across the shock front:

$$\iint_{S_0} \left((\mathbf{T}^0 \cdot \mathbf{n}_0)^+ + (\mathbf{T}^0 \cdot \mathbf{n}_0)^-\right)\,\mathrm{d}S_0 = \iint_{S_0} \rho_0 U_s[\mathbf{v}]\,\mathrm{d}S_0 \tag{2.20}$$

By construction, the unit normals on either side of the shock front are opposite in direction. Furthermore, a local condition may be extracted by examining the integrands above, since they are

both computed over the same surface, S_0.

$$[\mathbf{T}^0] \cdot \mathbf{n}_0 = -\rho_0 U_s [\mathbf{v}] \tag{2.21}$$

The planar plate impact geometry allows us to rewrite some of the terms above due to the assumption of 1D strain. Particle motion is constrained to the X_1 direction, and therefore the jump in velocity across the shock remains in the X_1 direction and is nothing other than u_p. $\mathbf{T} \cdot \mathbf{n}$ is oriented normal to the plane, and can be simplified to the normal stress in the X_1 direction.

$$[\sigma] = \rho_0 U_s [u_p] \tag{2.22}$$

The remaining jump condition is derived using the conservation of energy. The control volume described in Figure 2.4 may be used again, but instead of writing the momentum balance, the balance between the rate of work done by tractions and rate of energy change in the body may be computed:

$$\iiint\limits_{V_0} \rho_0 \mathbf{b} \cdot \mathbf{v} \, \mathrm{d}V_0 + \iint\limits_{A_0^+ + A_0^-} (\mathbf{T}^0 \cdot \mathbf{n}_0) \cdot \mathbf{v} \, \mathrm{d}A_0 = \frac{d}{dt} \iiint\limits_{V_0} \rho_0 \left[e + \frac{1}{2} \mathbf{v} \cdot \mathbf{v} \right] \mathrm{d}V_0 \tag{2.23}$$

Heat flux into and out of the control volume is neglected since the volume will be made infinitesimally small, and the shock moves so fast that we may assume the process to be adiabatic. As above, body force and the surfaces not parallel to the shock front disappear in the limit of volume going to zero and areas A_0 approaching S_0. The Reynolds' transport theorem may again be used to simplify the energy equation and provide a uniform basis of integration:

$$\iint\limits_{S_0} \left(((\mathbf{T}^0 \cdot \mathbf{n}_0) \cdot \mathbf{v})^+ + ((\mathbf{T}^0 \cdot \mathbf{n}_0) \cdot \mathbf{v})^- \right) \mathrm{d}S_0 = \iint\limits_{S_0} \rho_0 U_s \left[e + \frac{1}{2} \mathbf{v} \cdot \mathbf{v} \right] \mathrm{d}S_0 \tag{2.24}$$

A simpler form of the above equation may be reached with jump notation and substitution of the

conditions derived from the conservation of momentum and then mass:

$$\rho_0 U_s[e] = U_s \frac{\sigma^+ + \sigma^-}{2}[\epsilon] \tag{2.25}$$

We are left with three equations (2.17, 2.22, and 2.25) comprised of five unknowns: U_s, u_p, σ, ϵ, and e. What remains then is determining a constitutive relationship between two of the five unknowns such that the remaining quantities my be solved for once a single quantity concerning the shocked state is observed. A common constitutive equation is the Hooke's law for the case of continuum linear elasticity, which relates the state of stress in a material to the state of strain. In the case of a shock, a locus of material states across shocks of varying strength is known as the "Hugoniot", named after Henri Hugoniot (1851-1887), a French artillery officer [27].

Constitutive equations may be determined experimentally for individual materials, or derived from theoretical first principles. Since shock processes are by definition not continuous, only the initial and final states must be known; shock constitutive equations are therefore more commonly known as Equations of State (EoS). Equations of state my be defined with any of the two unknowns in the shock jump equations.

Hugoniot curves are most commonly defined in the Pressure (equivalently stress) - Volume space, Pressure - Particle Velocity space, or the Shock Speed - Particle Velocity space. A graphical example in the Pressure - Volume space is presented below in Figure 2.5.

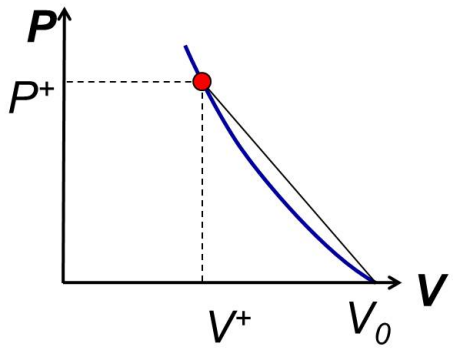

Figure 2.5: Illustration of a Hugoniot curve showing locus of states permissible across a shock wave in pressure (P)-volume (V) space.

In the simplest case, a shock propagates into an undisturbed material with a reference state described by state variables with subscripts 0. The material properties jump across the shock front from the reference state to some other state, P^+ and V^+. The straight line connecting the two states is defined as the Rayleigh line with a slope of $\rho_0 U_s^2$. It is a gross oversimplification that the material follows the path traced by the Rayleigh line during a shock process. The sharp jump in state variables and entropy in such a short period of time makes it very difficult to understand the exact material state within the shock front, so the states along the Rayleigh line serve only to better illustrate the magnitude of the shock jump. The points defining the Hugoniot curve are pressure levels required to compress a material to a certain volume, V, and are material dependent.

It is common in the shock physics community to report the locus of states in terms of shock and particle velocities, which are more readily measured in experiments. Over the course of may years of experiments, a pattern in velocity space Hugoniots has been observed: the shock velocity for most materials is linearly related to the particle velocity [17] [13]. Over an applicable pressure range, it is sufficient to write the Hugoniot as follows:

$$U_s = C_0 + s u_p + h.o.t. \tag{2.26}$$

where C_0 is the bulk sound velocity in the material, and s is a material parameter which is in the range of 1 - 2 for most materials [13]. Hugoniot data has been collated in this form for many materials [11]. It is therefore common to use at least one material that has been characterized in a shock experiment, so that quantities such as stress in the material under examination may be computed. The Hugoniot curves of condensed matter tend to be linear in the $U_s - u_p$ space, and the higher order terms may be neglected. In some cases, a quadratic term may be necessary to reduce the error in curve fitting to experimental data. As will be seen in Section 2.3, heterogeneous materials such as sand and composites can depart from the linear approximation to the Hugoniot. A piecewise linear Hugoniot has been observed for granular media as loading progress through compaction, pore collapse, and crushing regimes [23] [22].

The means of acquiring the data for creating material Hugoniot curves is discussed in the next section.

2.1.2 Planar Plate Impact

The generation of plane waves of one dimensional strain may be undertaken in one of several ways. Before the construction of large bore guns for plate impact, it was common to use plane wave generators and specially shaped explosive charges to drive a planar shock wave through a material of interest [49]. Time of arrival of the shock wave, its transit time, and particle velocity were then recorded with shorting pins spaced at various distances from the rear surface. Explosively accelerated plates and foils have also been used to generate high compressive stresses in target materials of interest [13].

As technology has advanced, so has the need to generate higher pressures in the laboratory to explore loading conditions and material response in situations found in ballistic impact, defense, planetary impact, and confinement fusion. While explosively driven shocks are still employed from time to time, more repeatable methods have become commonplace, which also allows for a more precise and varied choice of drive pressure. Smooth bore propellant and gas guns up to 4 in (100 mm) are common in university and government facilities for impact speeds up to approximately 1800 $^{m}/_{s}$ (gas gun) or 2200 (powder gun). The addition of multiple stages to gas guns may increase their capability to drive projectiles to even higher velocities.

The fundamental problem with guns is that a relatively large amount of mass must be accelerated, which limits the maximum velocities that may be economically achieved. To overcome that limitation, laser driven flyers are used, in which case target sizes are much smaller. An ablative material is applied to the uprange side of the target plate, and a high power laser pulse is directed onto the ablator. Laser energy and duration may be changed to control shock strength and duration. In addition, the shape of the loading pulse may be controlled [33]. Finally, facilities such as Sandia National Laboratories' Z- Machine employ electromagnetic compression on samples to reach particle velocities on the order of 50-60 $^{km}/_{s}$ [32].

2.1.3 Impedance Matching Techniques

The use of a previously characterized material as an impactor allows for the estimation of state variables in the target material via direct computation with the conservation equations. Impedance matching is a graphical technique in which the Hugoniot of the known material is plotted against a single Hugoniot point observed in a shock experiment. This idea is illustrated for 6061-T6 aluminum with a Hugoniot given by [13] in meters per second:

$$U_{s,Al} = C_{0,Al} + s u_{p,Al} = 5350 + 1.34 u_{p,Al} \tag{2.27}$$

The aluminum impactors have an initial velocity at zero pressure, since it is assumed that they are not accelerating at the time of impact. This initial condition dictates the starting point of the Hugoniot. As the flyer plate impacts the target, forward and reverse shocks are generated. Continuity requires that the particle velocity on either side of the impact plane interface be identical, along with pressure in the shocked state. The stress (pressure) can be written as:

$$\sigma = \rho_{0,Al} U_{s,Al} \left[u_{p,Al} \right] \tag{2.28}$$

The above equation is a simplified version of Equation 2.22, with the jump in stress replaced by stress in the shock state since the impactor is initially at zero pressure. The known relationship between shock speed (U_s) and particle velocity (u_p) in Equation 2.27 is then substituted in Equation 2.28 for stress:

$$\begin{aligned} \sigma = \rho_{0,Al} u_{p,Al} \left[C_{0,Al} + s u_{p,Al} \right] = \rho_{0,Al} s u_{p,Al}^2 + \rho_{0,Al} C_{0,Al} u_{p,Al} \\ \sigma = 3618 u_{p,Al}^2 + 14.445 x 10^6 u_{p,Al} \end{aligned} \tag{2.29}$$

Density has been substituted with $\rho_{0,Al} = 2700 \ {}^{kg}/_{m^2}$, and the units of stress are Pascals since all velocities are given in meters per second. To take into account that the projectile is not initially at rest, the Hugoniot curve may be reflected about the vertical axis and shifted right by the impact

velocity:

$$\sigma = 3618\,(u_i - u_p)^2 + 14.445x10^6\,(u_i - u_p) \tag{2.30}$$

It is noted that the particle velocity in the target, u_p, is one half of the free surface particle velocity measured from the rear of the target sample by the continuity and compatibility conditions described above. The quantity of stress has been substituted with hydrostatic pressure, where compressive pressure is positive. An impact velocity of $u_i = 1017\ {}^{m}/_{s}$ is used for illustrative purposes. The pressure - particle velocity Hugoniot of the aluminum flyer is shown in Figure 2.6. The average

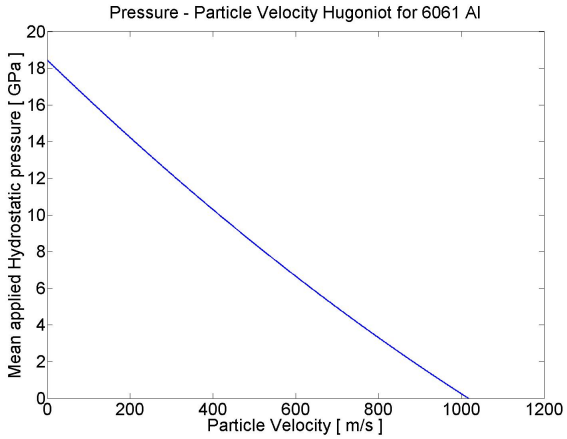

Figure 2.6: Pressure - particle velocity Hugoniot for 6061-T6 aluminum.

Hugoniot state of the target is given by the intersection of the locus of the shock states and the aluminum Hugoniot, which is given by the measured particle velocity. The interface (and aluminum) particle velocity was observed to be 704.2 ${}^{m}/_{s}$, and falls on the aluminum Hugoniot at 4.8 GPa as shown in Figure 2.7. Each additional experiment with a different impact velocity will produce one additional point in the pressure - particle velocity space. When a sufficient number of points have been accumulated, a curve may be fit to derive an empirical relationship between two state variables of interest.

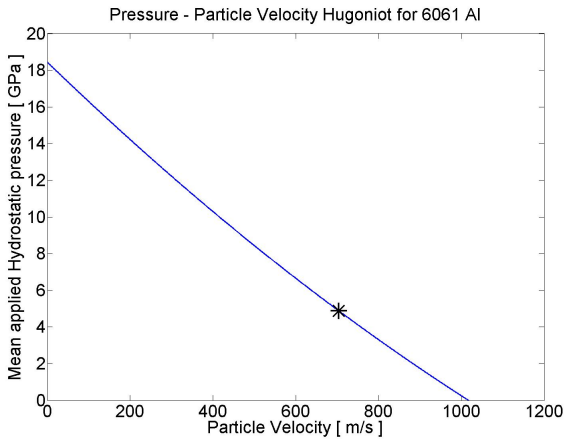

Figure 2.7: Pressure - particle velocity Hugoniot with superimposed computed target pressure.

2.2 Wave Scattering and Dispersion

Scattering and wave reflections are among the dominant mechanisms of shock front disruption in heterogeneous materials such as composites. The magnitude of shock disruption is highly dependent on the length scale of the material heterogeneity, as well as the shock strength. Shock disruption in composites is typically characterized by the degree of the departure of the straight shock front from its assumed form as a propagating sharp discontinuity in stress and particle velocity. At moderate and low levels of shock strength, the shock structure observed is mostly dependent on the impact strength, as lower magnitude shocks in composite materials are not typically steady [30] [38] [60].

The simplest form of introducing heterogeneity into a shock experiment is to use alternating layers of homogeneous materials impacted normal to the layer interface planes, and a systematic study on such a system was undertaken by Zhuang [64]. Not only are layered composites of great interest in defense and aerospace applications, but this geometry also ensures 1D wave propagation, and may be tuned to isolate the dependency of mechanical response on specific microstructure and material properties. Whenever a stress wave interacts with an interface, some of the energy is reflected, transmitted, or dissipated by interface damage or friction. In this study, only the reflection and transmission of waves will be considered. The final steady steady shock profile that results is dependent on the number of interfaces, as well as the mechanical property mismatch (e.g., shock impedance) at the interface.

In layered composites, the amount of energy reflected at each interface is a function of the shock impedance mismatch. The shock impedance mismatch is defined as the ratio of the shock impedance of the "harder" material and the "softer" material:

$$R = \frac{(\rho c)_{hard}}{(\rho c)_{soft}} \tag{2.31}$$

Shock impedance is the product of the material reference density, ρ, and its bulk longitudinal wave speed, c. The higher the impedance mismatch ratio, the larger the magnitude of the reflection. At its lower limit of R=1, the interface is perfectly matched, and the interface reflects no energy. More

energy is reflected as the impedance ratio increases, with complete reflection as R approaches ∞. For a linear elastic material, the fraction of the energy reflected back at each interface is given by the impedance mismatch factor, I [26]:

$$I = \left(\frac{R-1}{R+1}\right)^2 \tag{2.32}$$

When a layered composite is subjected to shock loading, both the backward (primary) and forward (secondary) reflections contribute to the final steady shock wave profile (assuming that the impact velocity is sufficiently high to attain a steady wave). Consider the following X-t diagram for a uniformly layered composite subjected to 1D strain loading:

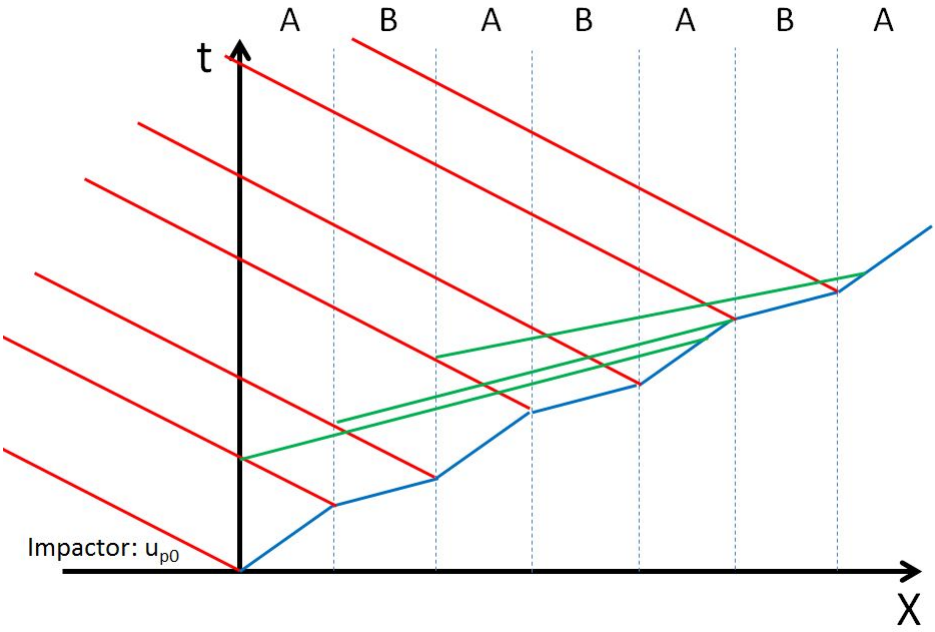

Figure 2.8: Model X-t diagram for a 1D wave propagation in a layered composite.

The impact problem described in Figure 2.8 uses a homogeneous impactor on the left hand side (X < 0) with an initial velocity of u_{p0} striking the first layer of the composite (X > 0). The layered material consists of two alternating materials of equal thickness, A and B, where B has a higher shock impedance than A. At (X,t) = (0,0), impact occurs, and a backward propagating shock is introduced into the impactor (red line denotes the shock front) and a forward propagating shock

enters material A (blue line denotes lead shock front in A and subsequently B and etc.). Each of the dotted vertical lines represents an interface between material A and B, and originates a reflected shock. These subsequent backward propagating shocks (red lines denote shock fronts) are due to the primary reflections of the lead shock wave at each interface. These primary reflected waves then interact with interfaces located upstream of the shock and can produce secondary reflections resulting in additional forward propagating shock waves (green lines denote these shock fronts). In the materials used in this study and in [64], higher pressure waves travel faster than the leading shock wave, allowing them to catch up and interfere with it.

The interference of the secondary waves with the shock front as well as the primary reflections directing energy away from the shock front results in a structured shock wave, with a finite rise time, typically one or two orders of magnitude longer than the rise time of a steady shock in either of the constituents of the composite by themselves. Figure 2.9 clearly shows the constructive/destructive

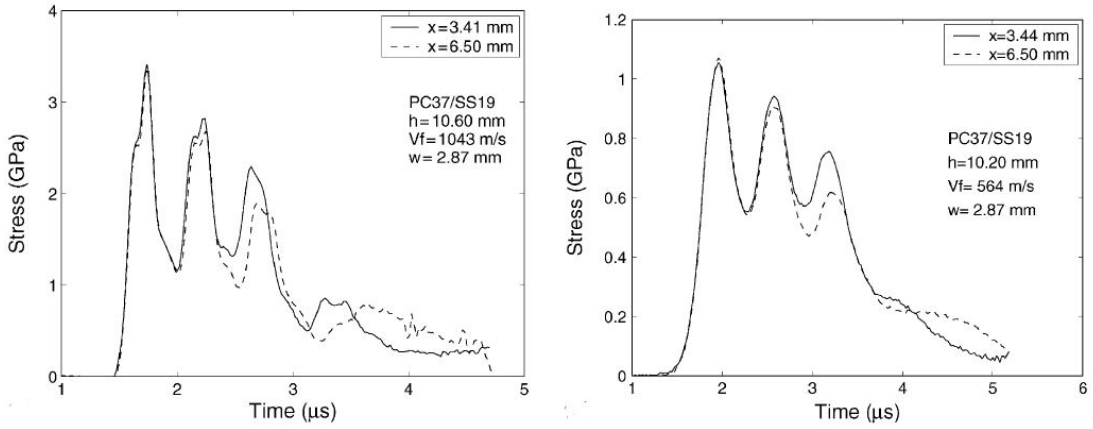

Figure 2.9: Shock response of polycarbonate/stainless steel layered composites showing steady waves. Adapted from [64].

wave interference effects on the structure of shock waves [64]. A polycarbonate/stainless steel layered composite consisting of 16 units of 0.37 mm thick polycarbonate and 0.19 mm thick stainless steel are impacted with polycarbonate (left) and aluminum (right) flyer plates. A 200 - 400 ns shock wave rise time is observed due to scattering of energy from the shock front, in addition to stress oscillations from the interference of the primary and secondary reflections. It was also found that an increase

in impedance mismatch resulted in increased scattering and longer rise times. Increasing interface density (thinning out the layers) reduces the observed rise time, as well as increases oscillation amplitude and frequency. Mean heterogeneity size is a dominant length scale in the scattering of shock waves.

The waves observed in the study by Zhuang [64] were all steady waves. Consequently, the experiments revealed a power law relationship between the strain rate and shock stress. In layered composites, the strain rate is proportional to the square of the shock stress.

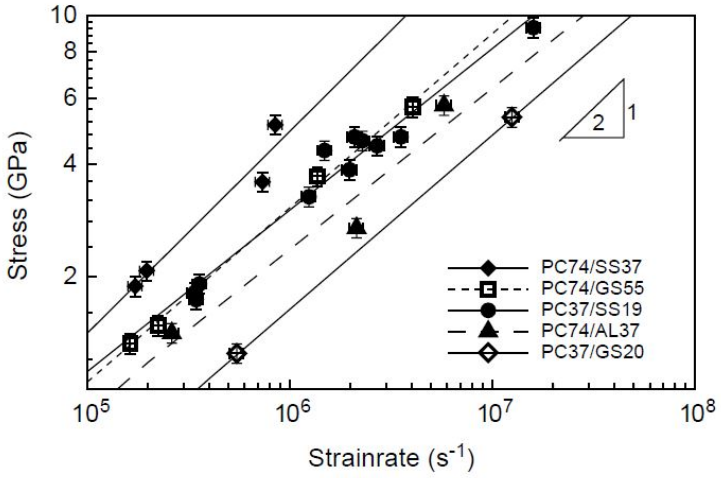

Figure 2.10: Shock stress vs. strain rate for steady waves in layered composites. Adapted from [64].

Grady [38] summarizes the dependence of stress on the strain rate in a variety of different metals and heterogeneous materials. Strain rate of steady waves in homogeneous materials such as metals tends to scale with the fourth power of the shock stress, indicating a much greater shock "viscosity" [64] in composite materials. The introduction of interfaces reduces the material acceleration at the shock front by redirection of energy. In steady waves, the shock profile becomes steady as a balance is reached between primary reflections sending energy away from the shock front and secondary reflections catching back up through precompressed media. The additional constraint of periodicity of the composites in [64] contributes to the large rise times.

2.3 Random Particulate Composites

The elimination of periodicity from composite materials removes global constructive and destructive interference as a mechanism for modifying shock wave structure. Local shock response and particulate distribution become far more important factors in the overall shock response of a composite. Due to the massive interest in composite materials for impact and blast protection, many studies of composite materials have been undertaken to understand their Hugoniot response, as well as their capability for shock wave structure control. Shock wave studies of particulate composites may be divided mainly into two categories: those driven to high enough pressures to propagate structured, steady waves, and those at lower pressures that develop structured waves, but are dominated by matrix response. Composite materials may also be separated by particulate size when scattering effectiveness is considered.

Although scattering is a dominant mechanism of shock structure development in particulate composites, the bulk of the work in the field is focused on Hugoniot response as a function of impedance mismatch and particulate size. Notable composites include concretes, polymer bonded explosives, epoxy-ceramics, epoxy-metal, and polymer-ceramics. These materials cover a large range of impedance mismatch ratios and particulate sizes. Except for the smallest particulate sizes studied in existing literature, the particle size distributions have been largely polydisperse. Volume fraction of second phase particulates is typically around 40% - 55%. Higher particulate volume fraction composites require highly polydisperse particulate size distributions or special fabrication methods to prevent de-bonding of the matrix from the particulates or agglomeration of particulates.

Due to their use as structural materials, concretes have been subjected to shock and blast for as long as mankind has had the means of launching projectiles and high explosives. Recent scientific studies of construction grade and high strength concretes have been undertaken by Tsembilis [58] [59] and by the Air Force Research Laboratories [46]. The studies undertaken on structural grades of concrete focus on specimens with large particulate size spreads in addition to large particulates on the order of 10's of mm in mean particle size [39] [44] [58] [59]. In the preceding cases, the Hugoniot response of the concretes (SAC-5 and CPSC: 10mm gravel particles at 40% - 45% by

volume) showed a weak dependence on particle size [59], and very closely matched the Hugoniot response of the mortar paste serving as the binder. Hall and Chhabildas [39] observed that for ASTM aggregate sizes of 57 and 7, Hugoniot response as well as shock structure was nearly identical and minimal dependence on particle size was observed. The descriptors "LC" and "SC" in Figure

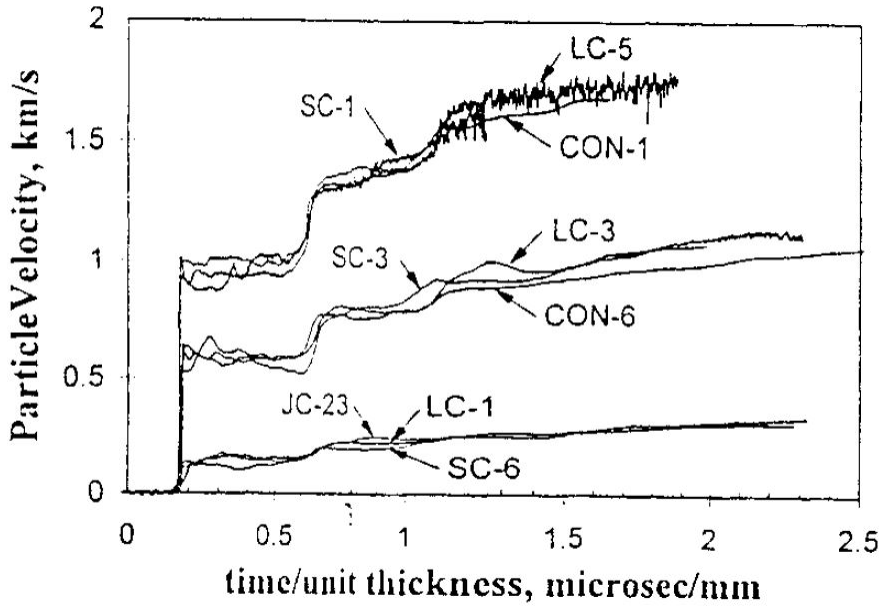

Figure 2.11: Shock wave structure for concretes with large particulates. Adapted from [39].

2.11 relate to aggregate size in the concrete, large and small, respectively. Traces with CON are for experiments with SAC-5 composition concrete, similar to SC concrete. At the scale of 10 mm - 25 mm particulates, very little difference in structure is noted. Discrepancies arise from location of measurement on the witness plate, due to the heterogeneity of the concrete sample.

The inclusion sizes of the concretes in Hall and Kipp's studies were much greater than the shock thickness of a steady wave in the pure matrix material (approximately 800 μm) [58]. The large difference in scales between the scatterer size and shock thickness in the pure constituent materials results in minimal scattering effectiveness, and the composite response is largely dependent on the matrix initial porosity and processing. Hall and Kipp propose that particle size does not meaningfully correlate with the shock response of concrete in the stress range that was explored [39] [44]. For scattering to be effective and a dominant contributor to shock structure, the wavelength of the

incident plane wave must be much greater than the size of the particle [38]:

$$\frac{A_s(r,\theta)}{A_I} = \frac{\pi a^3}{r\lambda^2}\left(\frac{\Delta E}{E} + \cos\theta\frac{\Delta\rho}{\rho}\right) \tag{2.33}$$

Equation 2.33 was derived by Lord Rayleigh for the relative magnitude of scattered energy at a point by elastic scattering of a plane wave by a spherical inclusion in elastic media, in the limit of small particles. The wavelength of the incoming wave is given by λ, E, is the modulus, and ρ is the density of the medium. The ratio of amplitudes on the left hand side, $\frac{A_s}{A_I}$, gives the relative amplitude at some point (r,θ) from the center of the sphere. While the waves under investigation in this study are far from the elastic regime, the dominant wave scattering factors still hold true at larger amplitudes. It is likely that the shock structure dependence on particulate size and mechanical mismatch will still dominate in the shock regime, but at smaller particle sizes.

Along these lines, high strength concretes intended for use in high rate deformation environments have transitioned away from the use of gravel as particulate and towards graded, engineered silica sand. These concretes are categorized as ultra-high-performance composite (UHPC) concretes, one example of which is Cor-Tuf [63]. The silica sand particulates in Cor-Tuf are mostly spherical crystalline grains ranging in size from 160 μm to 600 μm, and are embedded in a mixture of Portland cement and silica flour (with 90% of its particles smaller than 45 μm). UHPC concretes exhibited significant shock wave structure development in initial plate impact experiments [50].

Polymer bonded explosives (PBX) also fall into the range of materials where scattering induced by particulates is a significant mechanism that defines shock wave structure. These composites have low impedance mismatch ratios, and particulate size spreads centered on 250 μm and about 250 μm wide [18] [61]. These composites may also be considered to be nearly 50% particulate by volume when the fabrication conditions are considered. Many PBX compositions are hot pressed, melting the smaller crystals into the polymer binder, creating a mixture called dirty binder [61]. Larger high explosive crystals are then interspersed in this matrix mixture, contributing to the relatively low impedance mismatch ratio.

Simulations and experiments undertaken with the PBX samples noted above showed strong strain rate dependence on shock structure. Weak shocks were attenuated rapidly and steady waves were not observed below 0.5 GPa [30]. As expected, shock rise times decreased with increasing impact velocity, but they were also strongly dependent on wave propagation distance at lower pressures. Figure 2.12 clearly demonstrates the non-steady wave behavior of particulate composites at low

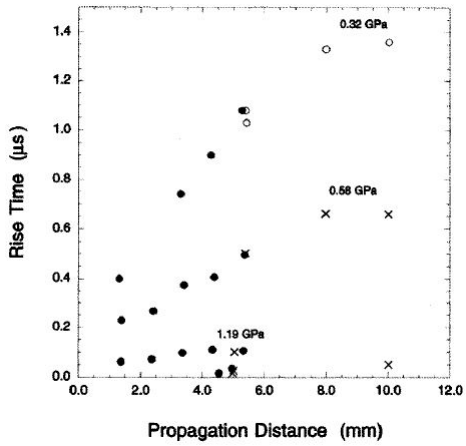

Figure 2.12: Compressive wave rise time vs. propagation distance for various impact stress levels in PBX9501. Adapted from [30].

stress loads. As pressure is increased moving from top left to bottom right, the rise times rapidly stabilize. This transition to steady waves is not well understood, but is likely an artifact of the low impedance mismatch ratio between the HMX and dirty binder material causing the response to appear closer to that of a homogeneous material. It is also likely possible that porosity and interface defects common in PBX materials [29] are significant factors in the impact response.

A final assortment of particulate composites are the epoxy matrix based potting compounds typically found in shock protection applications for electronics in munitions. Under the stresses induced when munitions strike the ground, a shock wave propagates from the nose cone towards the rear of the munition, subjecting the warhead and sensor package to high stresses. If the sensor package is not reinforced, the inertia of the individual components will pull them off of the circuit board and render it ineffective. Surrounding the surface mounted components with a composite shock attenuating material allows the assembly to survive until the most opportune time for munition detonation. The potting composites in common use are composed of fine ground alumina, tungsten

carbide, and aluminum. Typical particle sizes are on the order of 100 μm or less, down to about 1 μm. Impedance mismatch ratios in these composites are much greater than concretes and high explosives, typically in the range of R = 30 - 50 [60] [55].

Volume fractions of particulates are typically 45% - 50%, in line with high strength concretes and the high explosive materials mentioned above. At the highest end of the impedance mismatch scale are the tungsten carbide epoxy composites. Fine tungsen carbide granules were sieved to obtain particles between 20 μm and 32 μm [60]. Steady wave behavior was observed, and the strain rate was observed to be proportional to the average Hugoniot stress to the fourth power, similar to homogeneous materials and metals. The strain rate stress relationship in granular tungsten carbide scales linearly, indicating that the addition of a matrix material, even a significantly more compliant and less dense one, changes the deformation mechanisms from crushing and particle friction to scattering and wave reflection.

Significant pressure dependence on shock wave structure is noted at levels of 1.5 GPa and below. Rise times increase with propagation distance, while stress attenuates. Similar behavior below this stress level is observed in other ceramic - epoxy based composites, such as aluminum oxide epoxy composites of similar volume fraction and slightly smaller particle size (2 - 30 μm) studied by Setchell [54] [55]. Rise times of 60 ns at 2 GPa decreased to 10 ns at loading pressures of 4.43 GPa [54]. Wave propagation was observed to be nearly steady at the higher end of the pressure range; however, lower stress levels resulted in non-steady waves. Figure 2.13 demonstrates how the wave profile changes with increasing propagation distance in a 1.5 GPa average pressure experiment. The wave slowly steepens as it propagates, indicating that a balance between the dissipation and plasticity of the material, the wave scattering, and the increasing steepness of the Hugoniot curve is occurring near and above these pressures. For sufficiently strong shocks, the distance required to reach a steady wave propagation state, δ, is given by [21]:

$$\delta = \frac{3}{8}\frac{C_0}{s}\frac{1}{\dot{\epsilon}} \tag{2.34}$$

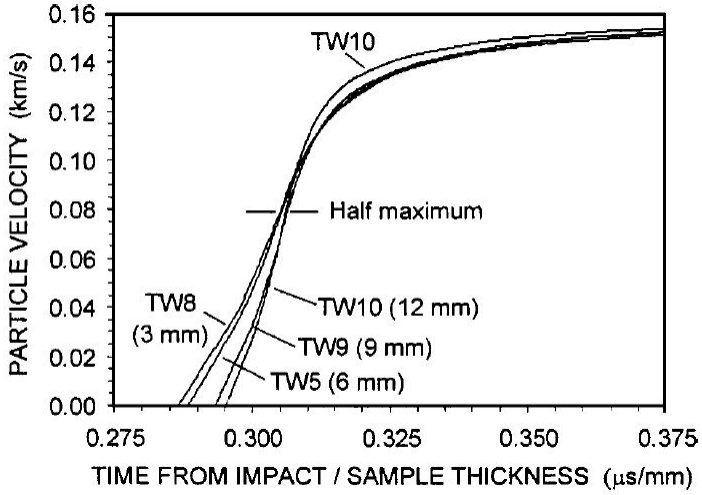

Figure 2.13: Stress wave profile as a function of propagation distance in alumina-epoxy composites. Adapted from [54].

C_0 and s are the linear Hugoniot parameters, and $\dot{\epsilon}$ is the strain rate.

At the lower pressures, the balance of the strength of the dissipation mechanisms such as viscoplasticity can override the shock steepening tendency induced by positive curvature of the Hugoniot curve of the constituent materials. A later study examined the effects of changing particle size on Hugoniot response, using smaller, spherical, sieved particles [55]. As the particle sizes are reduced, shock rise times are reduced (and assuming steady waves, the shock thickness as well). Furthermore, it was found that rise times increase slightly with volume fraction of particulate. Setchell [55] attributes this behavior to increased viscous dissipation. The present study intends to demonstrate that the shock structure evolution is scattering dependent, more so as the particle sizes become 2 - 50 times larger than the thickness of a shock wave in a homogeneous pure binder material.

A study of alumina particle based composites with a lower impedance mismatch ratio was undertaken by Neel [52] to determine the particle size effects on shock response. The alumina particles in the THV based composite were separated to 1, 10, and 100 μm nominal diameters. Again, Hugoniot state response appeared to be independent of particle size (within the resolution allowable by the varying levels of porosity in the composites), but stress time profiles showed a dependence on particle size. While the smaller particle sizes can be considered monodisperse, the 100 μm particulate composites had a ± 60 μm spread about the mean. Structure was also noted in the shock profiles,

even at a volume fraction of 25% particulates.

A summary of the notable shock wave studies on composite materials is presented in Figure 2.14. The axes are mean particle size in mm on the abscissa, with the impedance mismatch between the hard inclusions and relatively soft matrix or binder material on the ordinate. Error bars show approximate bounds of particle size spread, limited by sieving or reported probabilistic particle size distributions, where 90% of the particles in the composite may be found in the reported size range.

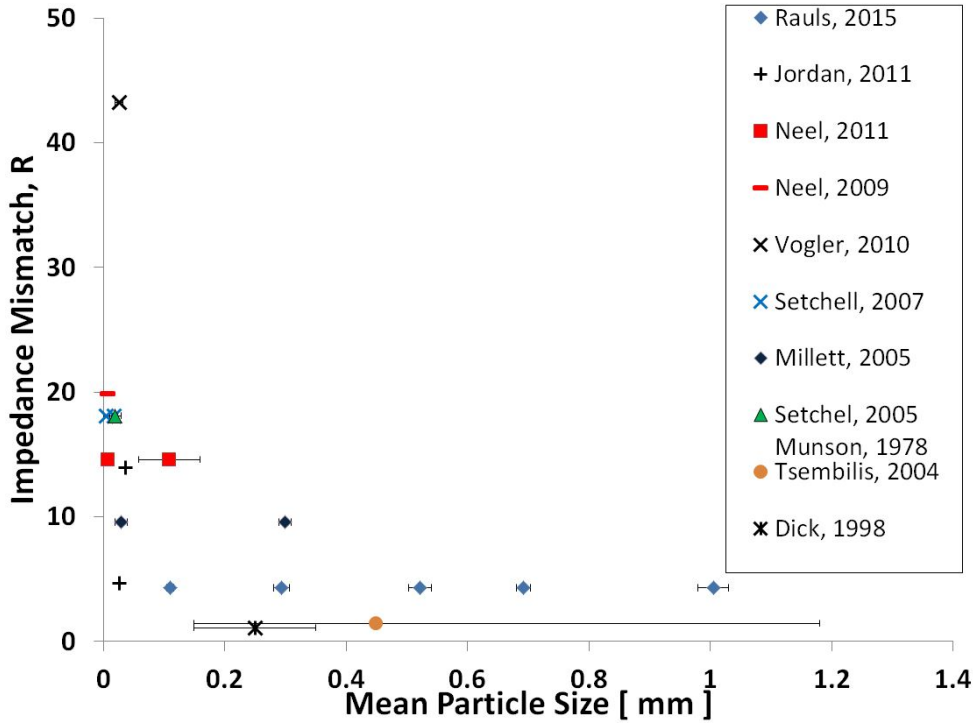

Figure 2.14: Summary of particle size vs. impedance mismatch ratio for various particulate composites. Adapted from [42] [52] [51] [60] [55] [54] [48] [59] [30].

The bulk of the experimental shock wave studies involving composites are characterized by small particles that are far more dense and possess a much higher wave speed than their encapsulating matrix material. These are the electronics potting materials as well as several model composites. Information and observations in this range of materials center on shock Hugoniot information, and tend to follow the fourth power strain-rate law [38] commonly observed in homogeneous materials such as metals. While the high impedance mismatch would indicate a high degree of scattering effectiveness, the inclusion sizes are far too small relative to the width of a shock in the pure material to be effective scatterers. The rise times then remain on the order of the pure matrix rise

time, with some shock structure development.

Structural materials such as concretes and PBX's occupy the lower portion of the chart. These materials have larger inclusions, and finite but smaller impedance mismatch ratios. While the larger particles enhance scattering and increase the spatial heterogeneity in the particle velocity, the concrete and PBX experiments focus largely on Hugoniot response and response at low pressures where shock waves may not be steady. Furthermore, the uncertainty in particulate size and shape increasingly contributes to the bulk material response. Therefore, a model particulate composite was developed to have a similar impedance mismatch to the structural and energetic materials of interest, while also spanning the particulate sizes that are effective scatterers with monodisperse size distributions.

In this manner, the dependence of shock rise time and stress profile on microstructure may be determined with a degree of certainty. Hugoniot response was measured and an examination of shock wave structure and its scaling on the dominant microstructural length scale are presented later in this study.

Chapter 3

Experimental Methods

3.1 Sample Preparation

3.1.1 Materials

The model material must meet several requirements in order for us to use it as a stand-in for concrete and energetic materials. As described in 2.2, the amount of energy redirected at each interface is a function of the shock impedance of the materials on either side of the interface given a strong bond. Given that the range of impedance mismatch in the materials of interest is between 2 - 10, the chosen model material must fall within that range and also be simple to acquire and fabricate. Two options that were considered to make particulate composites with rigid inclusions are casting and molding. Consequently, the likely matrix materials are polymers. A common industrial plastic with a reasonable wavespeed and density is Polymethyl Methacrylate (PMMA), more commonly known as Plexiglas. PMMA is available in monomer (MMA) form for casting as well as powders for compression molding. Choosing PMMA as the matrix then gives limits on the properties required from the inclusions. Simplifying the inclusion shape to a sphere increases options for inclusion materials to a multitude of glasses and ceramics.

Glass beads are common in microbiology microscope experiments [53] and are available in various graded sizes. The above manufacturing advantages, combined with the impedance mismatch falling into the middle of the range set by high strength concrete and PBX, make PMMA and glass the ideal candidates for a model composite. PMMA may also be heat treated to relieve or take advantage

of residual stress introduced in the molding process to control interface properties. Composites can be made with strong, perfect transparent interfaces or thermally shocked to produce weaker interfaces. This study will focus on relatively strong interfaces, which are more straightforward to simulate. After trial and error, it was found that mixing PMMA powder and glass beads produces even and random distributions of beads in composites with no evidence of settling or clumping. An even, random distribution mimics the common composites of interest to this study, and is also readily comparable to simulations on geometries with randomly generated particulate location distributions.

Molding grade PMMA is slightly different than the PMMA used for windows in typical shock propagation experiments [19] [25]. Windows are typically cut from Plexiglas (Atuglas International) or Perspex (Lucite International) sheet for optimal clarity and flatness. PMMA sourced in sheet form is typically cast from high molecular weight monomer. While commercially available sheets can be heated and formed or "welded", the viscosity of the material is bounded by its underlying chemical structure. At such high molecular weights (1,000,000 MW+) the molding temperature is higher than the autoignition temperature; the material will more readily burn than melt. The extremely long average chain length makes it difficult for the polymer chains to slide past one another to the degree required for compression molding, and thus the cast sheet materials do not depart the rubbery stage, even past 160°C [14]. As such, lower molecular weight compositions are chosen. A polymer powder of 75,000 MW (Polysciences, Warrington PA, P/N 04553) with a glass transition temperature, T_g, of 105°C is used as the matrix for the particulate composites in this study. Due to the discrepancy in molecular weight this material must be characterized in order to verify that existing PMMA simulation parameters can be used. Measured density of the as-molded and heat-treated polymer is 1.1804 ± 0.0003 $^{g}/_{cm^3}$ [1] which is identical to values found in the literature for molding grade PMMA, and 0.01 $^{g}/_{cm^3}$, or less than 1% less than the density of cast acrylic sheet.

Bulk elastic wavespeeds were measured from as molded samples using piezo actuator driven wave reflection experiments. An Olympus (Waltham, MA) 5000 series pulser-receiver and accompanying transducers were used to measure the time of flight of waves passing through PMMA discs of known

[1] Measured from the average of three individual targets, ID 140407_1-3.

thickness. Results are presented in Tables 3.1 and 3.2 below.

Sample	Thickness [mm]	Time [μs]	Round Trips	Wave Speed [$^{km}/_{s}$]
1	9.499	14.19	2	2.678
2	7.112	15.91	3	2.682

Table 3.1: Longitudinal bulk wave speed for as molded PMMA.

Sample	Thickness [mm]	Time [μs]	Round Trips	Wave Speed [$^{km}/_{s}$]
1	9.499	14.08	1	1.349
2	7.112	10.54	1	1.350
2	7.112	21.04	2	1.350

Table 3.2: Transverse bulk wave speed for as molded PMMA.

Shock impedance of PMMA can then be computed as:

$$Z_{PMMA} = \rho_{PMMA} \times C_{0,PMMA} = 3.163 \frac{GPa}{^{km}/_{s}} \tag{3.1}$$

With the matrix well characterized, the inclusion material may be chosen. Spherical particles are most readily sourced from glass microsphere suppliers. Standard values for silica glass are ρ_{glass} = 2.203 $^{g}/_{cm^3}$, with a bulk wave speed of 5.93 $^{km}/_{s}$ [19]. The shock impedance is then:

$$Z_{glass} = \rho_{glass} \times C_{0,glass} = 13.064 \frac{GPa}{^{km}/_{s}} \tag{3.2}$$

$$R = \frac{Z_{glass}}{Z_{PMMA}} = 4.13 \tag{3.3}$$

The above two materials satisfy the impedance mismatch requirement of our ideal model material to control the amount of energy reflected at each interface. Next, the quality of the interface between the phases must be able to be controlled. For simplicity in initial tests and simulations, a perfectly bonded interface between the composite phases is assumed. The perfectly bonded assumption negates the need for estimates on the friction coefficient at the interface, as well as the fraction of the interface area that is not well bonded. It is readily apparent, however, that inter-phase bond-

ing in some composite materials of interest that we are trying to approximate (PBX, for example) is less than perfect. The motion of grains within the composite and the collapsing of pores create hot spots that drive explosive detonation [29]. It is likely that future work with this material may take advantage of the thermal expansion coefficient differences on PMMA and glass to produce weaker interfaces and voids around the particulates. Heat treating is discussed later in 3.1.4, but the choice of materials for the model composite ensures that both strong and weak interface conditions may be explored.

Finally, the PMMA and glass bead model composite must satisfy geometrical constraints on the locations of the particulates within the composite itself. Typically, when one looks at concrete or PBX, an even distribution of particulate is noted. Settling of aggregate in concretes is generally considered to be detrimental to its compressive strength and longevity in the field. As such, there exist many standards in the construction industry for measuring the amount of settling that happens for various concrete mixes, as well as setting a limit on the degree of settling (ASTM C1610 and ASTM C 1712). As such, the model composite should not exhibit significant settling of the particulates during fabrication. Initial attempts at making samples employed the use of casting a slurry of MMA and glass beads with a catalyst. The goal was to partially polymerize the MMA to the point that its viscosity would suspend the beads, but the MMA never catalyzed quickly enough. Slow polymerization also allowed the remaining MMA to vaporize, leading to shrinking problems. Cast samples are shown in Figure 3.1.

Shrinkage is clearly visible in all composite samples as evidenced by the raised edges, as much as .1 in (2.5 mm) along the outside diameter. The three samples with beads show considerable settling and/or porosity, both undesirable results. Fortunately, the thermoplastic properties of PMMA allow for the use of compression molding as an alternate fabrication method. The average size of the Polysciences PMMA granules used in this study were about 200 μm in diameter, comparable to the size of the glass spheres used in the creation of the composites. As such, when the PMMA granules and glass spheres were mixed and poured into the mold, they remained well mixed. Confinement in the mold and high viscosity of PMMA even at 180°C ensured that the heavier beads did not

Figure 3.1: Samples made by casting, and failure modes.

settle during the molding process. A cross section is presented in Figure 3.2. The micrograph of

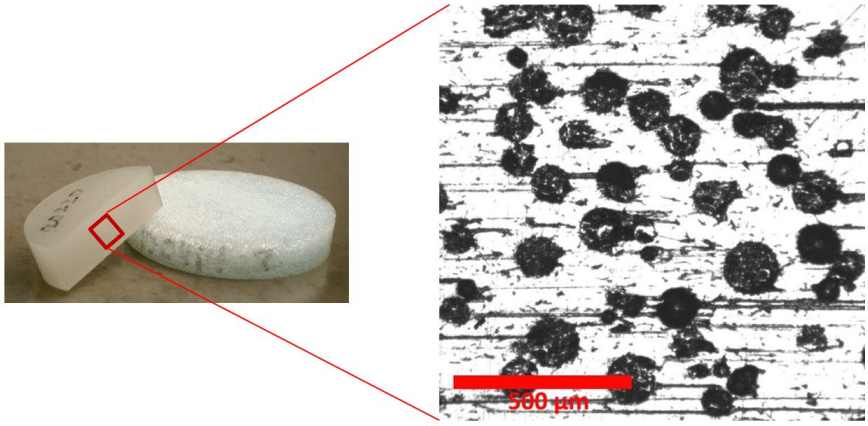

Figure 3.2: Micrograph of model particulate composite cross section.

sample 120220 at 22% glass by volume confirms that there is even distribution of particles though the thickness and that no settling has occurred during the molding process. Identical behavior is noted for the entire range of bead sizes used in the study, from 100μm to 1000μm. The molding process is described in detail in 3.1.3.

3.1.2 Sieving and Glass Beads

Particulate composites such as PBX and concrete have highly complex microstructures, with a random distribution of particulates, and a wide distribution of particulate sizes and shapes. In order to determine the effects of particulate size on shock structure, the size must be isolated, and the geometry simplified. Using solid spherically shaped particulates eliminates the need for quantifying the jaggedness, sphericity, or void fraction in analysis. Spheres are characterized solely by their diameter and are invariant to orientation of the incoming shock wave. This consistency allows for the use of sieves to separate the beads by their size with relative ease. Wire mesh sieves are available from industrial supply companies (Grainger, Los Angeles CA), and the wire count and size chosen to filter glass beads of the desired diameter. Thus, the size distribution of beads within a given sample can be controlled, and bounds placed around the "average" bead size.

The beads within the ranges determined by the sieving screens are assumed to be uniformly distributed between the minimum and maximum bead diameters. Beads are sieved from larger populations with a large spread in bead diameters. For example, the 500 μm diameter beads used in the study are sieved from bulk beads advertised as being 400 μm - 600 μm and 500 μm - 750 μm. Other sizes are sieved from bulk beads with similarly large spreads. An approximately Gaussian distribution of beads is assumed for the bulk beads. Since the sieved beads used in the making of the composites are taken from near the center or near the ends of the bulk ranges, the change in the probability distribution function of the bulk beads over the range of interest is assumed to be small.

Glass beads are sourced from Corpuscular Inc. (Cold Spring, NY) in one of six different bulk products, as shown in Table 3.3. Beads sieved from the large end of the advertised range were

Product Number	Advertised Size Range [μm]	Target Use [μm]
149117-50	90-150	100
149123-50	300-400	300
149125-50	250-500	300, 500
149127-100	400-600	500
149129-100	500-750	700
149133-100	1000-1250	1000

Table 3.3: Bulk glass bead products used in experiments.

typically unusable due to deformed or oblong beads, as well as multiple beads stuck together. These bead quality issues were more prevalent in the larger bead products. When misshapen beads were observed in sieving, they were manually removed. The above products yielded approximately 7-10% by weight of beads in the desired range. As such, large quantities of beads were ordered, knowing the bulk would be discarded or unfit for use.

The process of sieving is straightforward, but time consuming. Such fine mesh screens as used in the preparation of these samples clog rapidly with oversized beads. Therefore, only small quantities of beads may be processed at one time. In addition, this clogging prevents undersized beads from passing through. While this may make it seem like the yields achieved are favorable, not removing the smaller beads has the unintended effect on the observed shock rise times of reducing the average bead size of the sample. As such, each sieving step is performed twice to ensure that as many of the undersized particles that can get through do get through. The sieves must also be spaced far enough apart to ensure adequate yield, while still constraining the size range enough for reasonable analysis. Pass bands of approximately 20 μm - 40 μm were chosen where possible with commercially available mesh screens. The mesh screens were obtained from Grainger (Los Angeles, CA) and are listed in Table 3.4.

Product Number	Mesh Number	Wire Size [in]	Opening Size [μm]
3DLP5	#150	.0026	104
3DLP4	#120	.0037	116
3AMA2	#64	.0045	281
3AMA1	#62	.0040	307
3ALY7	#38	.0065	503
3DNF5	#30	.0120	541
3ALY3	#30	.0065	681
3GPJ7	#24	.0140	704
3DLL1	#18	.0170	980
3AKC7	#18	.0150	1031

Table 3.4: Sieve sizes for glass bead segregation.

The sieving process is easily the most time consuming (but necessary) part of the composite fabrication process. Bulk beads are filtered through the largest sieve within the advertised range to remove the largest (typically also misshapen) particles. Removing the largest beads also reduces

clogging of the screens in subsequent sieving. Once the largest beads are removed, the actual yield may begin to be separated from the bulk. The following process flow is for 300 μm beads taken from P/N 149125-50, but is similar for all average bead sizes. A photograph of the sieving arrangement is presented in Figure 3.3.

1. Obtain and set up a sieve (503 μm) and primary catch bin as shown in Figure 3.3.
2. Pour approximately 10-20 g of bulk beads on to the sieve, evenly distributed over the area above the primary catch bin.
3. Process all of the bulk beads to remove grossly oversize and misshapen beads.
4. Separate the oversize beads on top of the screen into a secondary catch bin.
5. The beads in the primary catch bin contain the future yield. Pour them into a clean bag and clean the primary catch bin. Discard the beads in the secondary catch bin.
6. Obtain the large screen of the size range of interest (307 μm), and set up on primary catch bin.
   (a) Process small amounts of beads (10-20 g) to minimize clogging of the screen and ensure that as many beads under 307 μm pass through.
   (b) Separate oversize beads to secondary catch bin, clean, and unclog sieve. Reset.
   (c) Take the beads in the secondary catch bin, and sieve them with the 307 μm sieve a second time.
   (d) Separate oversize beads to secondary catch bin, clean, and unclog sieve. Discard oversize beads. Reset. Repeat previous three steps until all beads are processed.
7. The beads in the primary catch bin contain the future yield. Pour them into a clean bag and clean the primary catch bin.
8. Obtain the small screen of the size range of interest (281 μm), and set up on the primary catch bin. The yield is now going to be the beads that do not pass the 281 μm sieve.

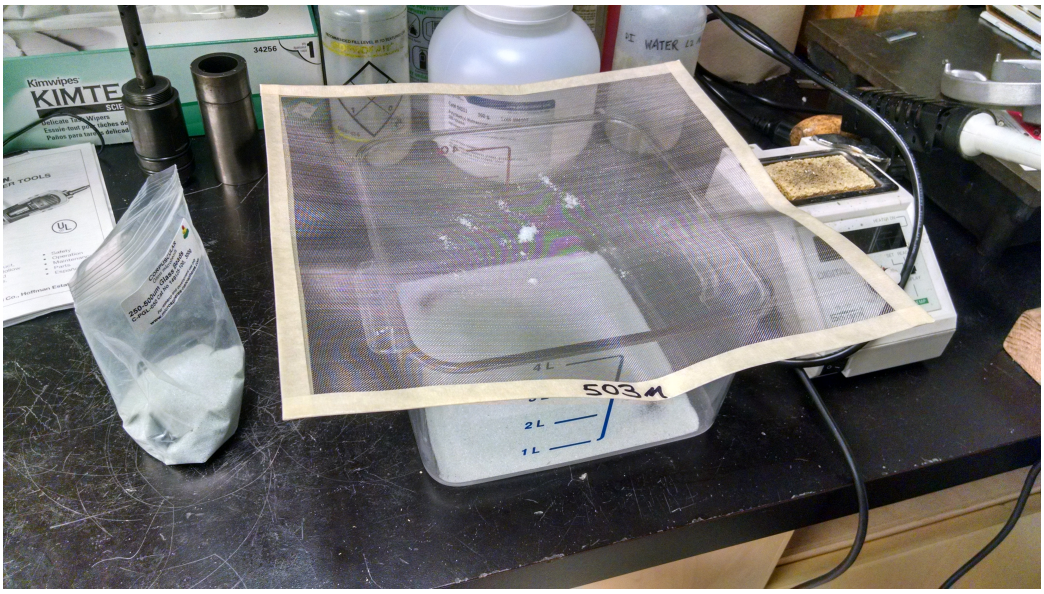

Figure 3.3: Photograph of sieving arrangement for separating particulates from bulk beads.

9. As done above for the 307 μm sieving step, repeat for the 281 μm screen. Instead of discarding beads in the secondary bin, store them in a clean, marked bag.

10. Continue sieving until all beads are sieved. Clean sieves and work bench.

The repetition involved in each sieve step is necessary to ensure that as many of the beads that can pass through the screen do pass through the screen, and are not simply being held up by clogging. A large number of retained undersize beads can skew observed rise times and render the computation of interface area and density inaccurate. Consequently, re-sieving is required as an error reduction process.

3.1.3 Molding Process

Compression molding of polymers is a well understood process, and is used in the fabrication of many household and industrial products with a variety of polymers. Polymers used in compression molding can be thermosets or thermoplastics. Typical compression molds involve two mold halves, which enclose a cavity in the shape of the part to be molded [9] [12]. Mold parameters for the 75000 MW PMMA used in this study are available in [14]. The matrix material must be placed in a mold capable of sustaining temperatures of 105°C for extended periods of time. A design for

a PMMA compression mold is presented below. Specific weighing and transfer practices must also be employed to reduce loss of raw components and ensure accuracy of computed volume fraction values.

The matrix and particulate components of the composites begin as separated powders and particles. The components must be weighed out and identified for future steps. A Sartorius (Bohemia, NY) GD-503-NTEP scale (S/N: 24250264) was used for the following sample weighing process.

1. Power on the scale and allow 20 minutes for warm up.
2. Place a weighing boat (Sigma-Aldrich P/N:Z154881, St. Louis, MO USA) on the scale, let it settle, and zero the scale.
3. Consult notebook for appropriate weights of components, determined by sample thickness and glass volume fraction.
4. Add appropriate weight of PMMA powder to weighing boat. Note actual weight. Zero the scale.
5. Add appropriate weight of glass beads to weighing boat. Note actual weight.
6. Label weighing boat with sample serial number for later identification.
7. Transfer sample in weighing boat to an oven at 50°C for drying overnight.

At this point, the powders are unmixed and spread out in the bottom of the weighing boat for drying. PMMA granules can pick up moisture from the air [14], so leaving the powders spread out in the weighing boat enhances drying.

Once the drying process is complete, the powder and beads must be mixed to produce the uniform bead distribution desired. The use of a glass or plastic tube allows the buildup of static charges, which can cause the PMMA powder and some small glass beads to stick. A conductive aluminum tube is therefore a better choice to use to reduce the amount of PMMA that remains stuck to the tube after the mixture is poured into the mold. An Analog Vortex Mixer from VWR (Radnor, PA) provides the vigorous vortexing of the powders within the tube. Samples are mixed for one minute

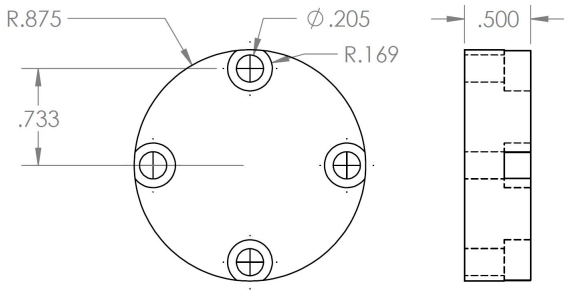

Figure 3.4: Base platen dimensions in inches.

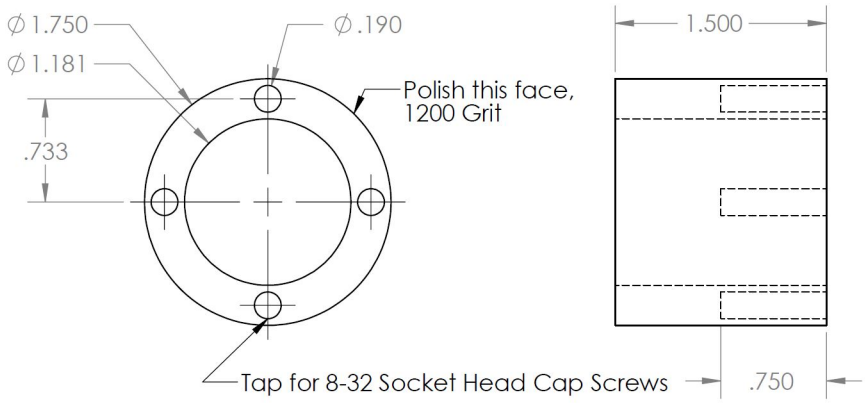

Figure 3.5: Mold cavity dimensions in inches.

continuously, allowed to rest for one minute, and mixed continuously for one more minute. They are then immediately poured into a mold preheated to 50°C.

The compression mold used for this study was custom-made to optimize sample quality. The base material is 304 stainless steel, chosen for its strength and temperature-stable mechanical properties. It is assembled from three individual pieces: a base platen, a mold cavity, and a punch platen. The base and punch platens were lapped and polished to 1200 grit to reduce the amount of final polishing work to be done on the molded sample composites. The clearance between the diameters of the mold cavity and punch platen were designed to minimize PMMA flash while still permitting air to escape from in-between the granules. The difference on the diameters is 0.006 in (0.152 mm). These clearances were determined from the examination of past work in [62], where compression molds were used to flatten acrylic sheets. The individual parts are shown with their dimensions in Figures 3.4, 3.5, and 3.6. The assembled mold is shown in a photograph in Figure 3.7.

Once the mold is loaded with the well mixed powder and glass beads, the punch is forced down

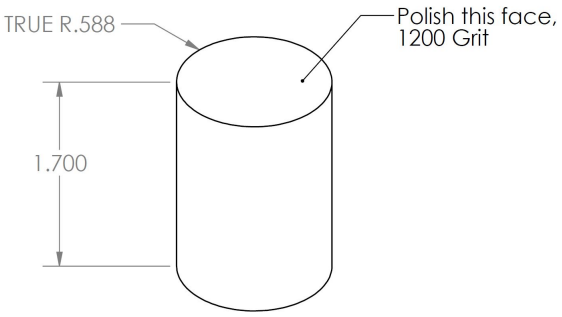

Figure 3.6: Punch platen dimensions in inches.

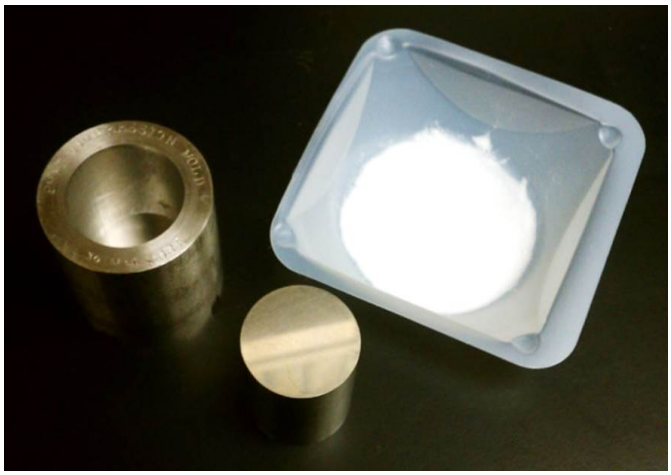

Figure 3.7: Assembled compression mold with PMMA powder.

Figure 3.8: Assembled PMMA compression mold in vacuum bag for molding.

as far as it will go to lock the powder down and keep it from shifting during the remainder of the preparation process. It is critical to avoid sharp impacts and shaking once the powder is poured to avoid settling. Having the punch pressed down should mitigate the effects of impact, but it's best to avoid it altogether if possible. The assembled mold is then transferred to a vacuum bag. Vacuum bagging accelerates the removal of excess air from between the powder granules in the mold, and prevents oxygen from reaching the molten plastic while the mold is subject to elevated temperature. The vacuum bag film is Wrightlon 7400, from Airtech (Huntington Beach, CA). Wrightlon 7400 is a nylon polymer able to withstand temperatures up to 204°C, which is necessary during the compression molding process. A vacuum bagged sample is shown in Figure 3.8.

After reaching a vacuum level of at least -25 in. Hg (-635 torr) for 5 minutes, the mold is placed between the compression mold platens and 600 lbf (2670 N) is applied with a pneumatic ram under the bottom movable platen. The force applied to the mold is held constant during the duration of the molding process. The compression molding machine is a custom unit from OEM Press Systems (Fullerton, CA), which has been modified with new platen temperature controllers from Newport (Irvine, CA) to reduce the possibility of unintentional temperature drops during molding. Once the pressure is applied, the heaters in the platens are turned on and allowed to heat up to 180°C (indicated on the front panel). Temperature level of 180°C is maintained within ±2°C for at least 18 hours. The temperature and pressure have been chosen to permit plastic flow around the glass

Figure 3.9: Mold under vacuum in press with insulation.

spheres, without the plastic becoming so fluid that the glass beads can settle. The mold and vacuum bag are surrounded with aluminum foil insulation around the edges of the platens, as shown in Figure 3.9.

The insulation blocks air conditioning currents and helps keep the temperature stable during molding. A vacuum gauge is also visible in order to monitor for adequate vacuum during molding. After 18 hours of heat and pressure, the vacuum line is removed, pressure released from the platens, and the bagged sample placed immediately into a pre-heated heat treating oven.

3.1.4 Heat Treating

The interface quality required in this study requires the use of a heat treating process to relieve internal stresses and maintain a strong bond between the phases. The mold must not experience rapid thermal shock upon removal from the compression molding machine or sample damage will occur. The large difference in thermal expansion coefficient between PMMA and glass causes a strain mismatch, which can be large enough to pull the plastic away from the glass spheres and damage interfaces. Fortunately, this symptom of improper heat treating is readily visible to the

naked eye. Samples with strong bonding are nearly transparent, and the interfaces difficult to see. As the plastic begins to debond, the samples become opaque, as in Figure 3.10.

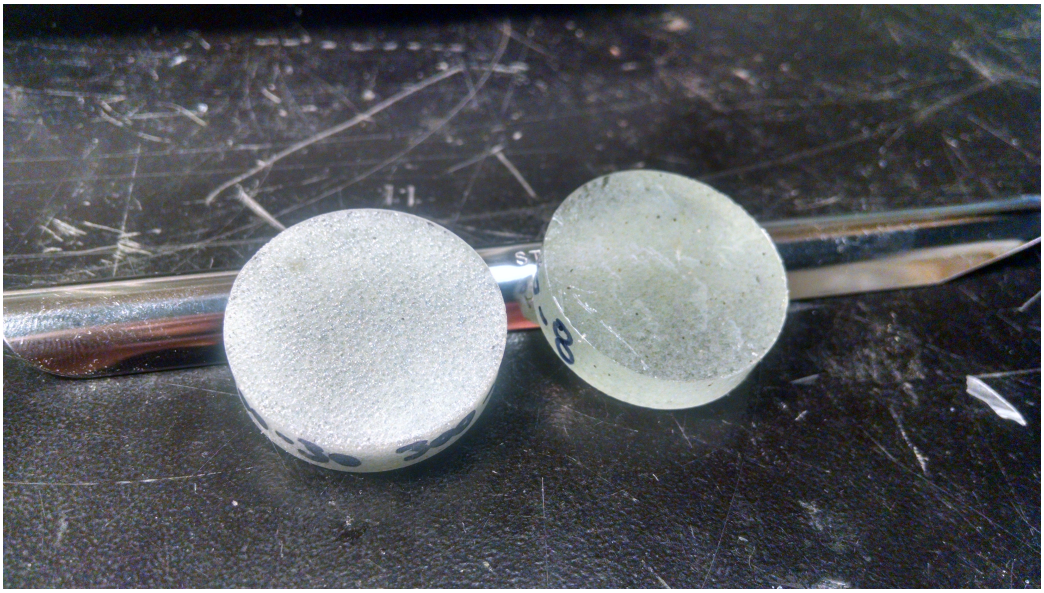

Figure 3.10: Sample debonding failure due to inadequate heat treatment (Left) and sample with proper heat treatment (Right).

The heat treating process designed in this study allows the plastic to relax to a stress-free state, while maintaining interface integrity. Strong bonding requires the following process, especially at high volume fractions of glass (40% VF glass +):

1. Preheat oven to 150°C.
2. Upon completion of 18 hour molding cycle, deactivate air ram and remove vacuum line with mold assembly still between heated platens and behind aluminum insulation.
3. Quickly remove mold assembly in vacuum bag and transfer into preheated oven.
4. Maintain sample in closed mold at 150°C for at least 12 hours.
5. Slowly cool sample while still in oven (reduce target temperature in oven by 15°C per hour).
6. When the sample has cooled to 50°C, remove from oven.
7. Remove mold from vacuum bag, open mold, and press out sample.

8. Wrap sample in aluminum foil to reduce air exposure during second heat treating step.

9. Return sample to 50°C oven, and set target temperature in oven to 150°C.

10. Maintain free sample at 150°C for at least 12 hours.

11. Slowly cool sample while still in oven (reduce target temperature in oven by 15°C per hour).

The first heat treatment step relieves stresses through the sample thickness, while the second step is necessary to relieve stresses due the removal of the sample from the mold, when the radial confinement no longer exists to force the plastic against the beads. Samples that do not receive the second heat treatment step initially appear normal, but over the course of several days separation of the phases occurs at the circumference, and cracks/separation propagates inwards. If weak interfaces are desired, rapid cooling and skipping the second heat treating step will produce rapid separation of the phases. Future studies that focus more on the PBX end of the spectrum may make use of this phenomena to mimic the relatively weak interfaces between the explosive crystals and urethane binders in those materials without having to resort to experimenting on the explosives directly.

3.2 Experimental Design

3.2.1 GALCIT Powder Gun

Impactor plates are accelerated to high velocity using a powder gun at the Solid Mechanics High Strain Rate Laboratory at the Graduate Aerospace Laboratories of the California Institute of Technology (GALCIT). The powder gun is capable of providing shock loading for a variety of target geometries and is readily adaptable to the propulsion of a large variety of sabots and projectiles. The gun is a 36 mm smooth bore breach loading single shot cannon, with a barrel length of approximately 3 m. A schematic of the gun and target assembly is presented in Figure 3.11.

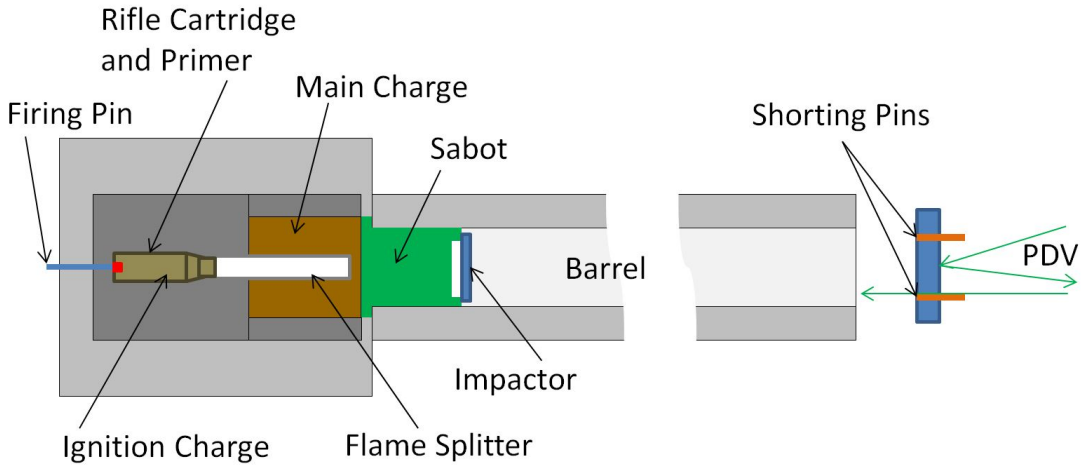

Figure 3.11: GALCIT Powder Gun system configuration.

A coil driven hammer drives a hardened steel firing pin into a bench rest grade rifle primer (CCI, Lewiston, ID) for reliable ignition. Upon hammer impact, the firing pin is propelled down the firing pin channel to strike the primer solely under its own inertia. The pin crushes the primer approximately .020 in (.6 mm), sending a short burst of sparks into the powder contained in the .30-06 Springfield rifle cartridge (Winchester, New haven, CT). The powder inside of the rifle case is intended as an ignition charge, to ensure a complete burn of the much larger main charge. The ignition charge is composed of 3 g of smokeless magnum pistol powder (Hodgdon, Shawnee, KS).

The hot gasses and flame from the ignition charge travel down a flame splitter tube, which serves as a manifold to evenly ignite the main charge in the cavity behind the sabot and impactor assembly.

The charge cavity is capable of holding up to 50 g of smokeless rifle powder. Powder calibration curves are provided in the laboratory for Hodgdon's H4198 Rifle powder. The H4198 powder has been specifically chosen to match its burn rate to the sabot diameter and gun barrel length, ensuring that the projectile is not accelerating just before impact. Use of other powders may adversely affect impact velocity or create a dangerous chamber overpressure condition and should be avoided.

Rapid combustion of the main charge elevates the chamber pressure until it is high enough to break the retaining ring on the sabot, at which time it begins to accelerate down the barrel. The sabot is fabricated from molybdenum disulfide impregnated nylon, also known as Nylatron (Quadrant Plastics, Reading, PA). In addition to the retaining ring, the sabot is machined with an angled cavity on the breech end to enhance sealing via expansion against the bore. Additional circumferential sealing rings are present on the sabot body. Multiple counterbores are present on the impactor end to provide a free surface condition for the impactor plate allowing for the completion of release and spall experiments. An engineering drawing of the sabot is shown in Figure 3.12.

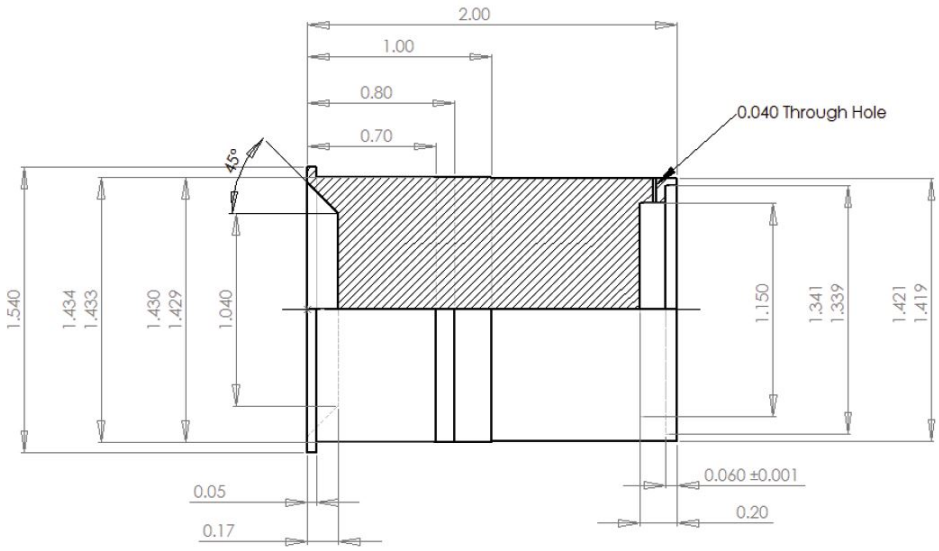

Figure 3.12: Nylatron sabot dimensions in inches. Adapted from [24].

The target chamber and gun barrel are evacuated of air before shooting to eliminate air being pushed down the barrel as a source of impact tilt error. Having a consistently low vacuum also enhances the quality of the impact velocity estimate as a function of charge weight. Impact velocities

attainable with this system range from 450 $^{m}/_{s}$ to 1800 $^{m}/_{s}$. Impact velocity is estimated by the amount of powder used and the projectile mass according to the relationship in Equation 3.4:

$$V = A \times (^{p}/_{m})^{B} \tag{3.4}$$

V represents impact velocity in [$^{km}/_{s}$], p is the total powder charge weight (primer and main charges) in [g], m is the projectile assembly mass in [g], and the constants A and B are empirical constants that are updated after each shot. Values for A and B are available in the laboratory handbook or Shot Data repository. Impact velocity can be estimated within 1% to 5% of the actual measured value.

Projectile velocity is measured during experiments with heterodyne velocimetry, while impact time is recorded with a set of four electric shorting pins flush mounted with the target. The shorting pin outputs are wired directly to an oscilloscope for timing, in addition to an OR circuit for reliable triggering. A pre-trigger record of 30 μs provides enough time for an accurate impact velocity measurement. The tilt of the flyer with respect to the target is computed from the impact times measured by the shorting pins.

3.2.2 Target Configuration and Fixture

The target holder is a 3.25 in. (82 mm) diameter disk, approximately 0.48 in. (12 mm) thick. It has a number of design features that are there to assist the experimenter and reduce wear on the target holder assembly in the blast chamber. Three 10-32 threaded holes on a 2.75 in. (70 mm) diameter are provided for tilt adjustment. Screws may be inserted into the mount from the rear, and when the target holder is floated on springs, adjustment of the tilt is rapid and simple. Tilt alignment is completed with a 1/10th wave mirror affixed to a vacuum chuck, which is then stuck to the impact face of the target. The mirror allows for accurate, repeatable alignment of non-reflective targets. A laser is aligned to be collinear with the barrel axis, and shined upon the mirror attached to the target face. The laser beam is made to reflect back on itself, indicating that the mirror (and thus

the target) is perpendicular to the barrel axis. Collinearity of the incident beam with the barrel axis is ensured through the use of two pinholes that are inserted in the breech and muzzle ends of the barrel. Tilt magnitudes of approximately 5 mrad were commonly observed.

There is also a breakaway groove, 1/4 in. (6.35 mm) thick that goes approximately 2/3 of the way through the plate. This allows the target holder to break apart after the experiment without bending the alignment and centering bolts on the mounting fixture.

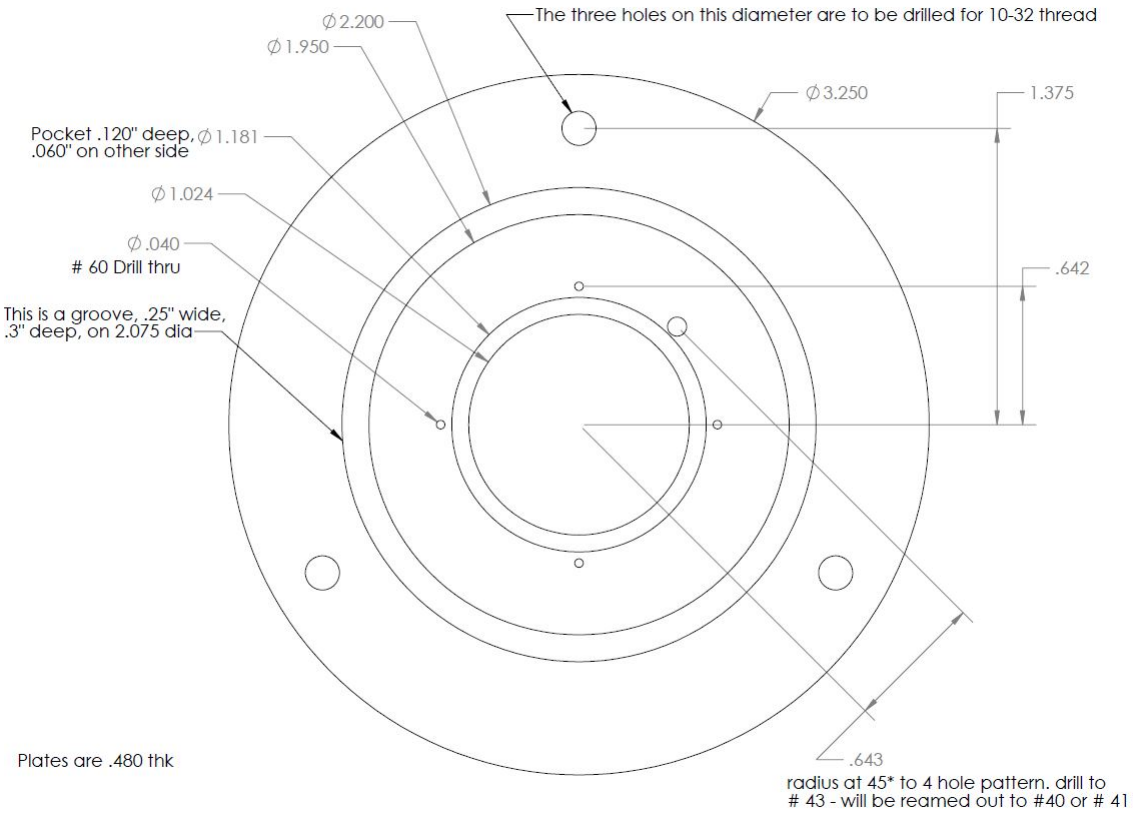

Figure 3.13: Target holder plate, demonstrating breakaway groove and tilt adjustment enhancement. All dimensions in inches.

An additional feature built in to the target holder is the PDV probe pass through at the 1:30 clock position on the target holder. The hole allows a PDV probe to look past the target and down the barrel of the cannon in 3.2.1, as it lies on a diameter smaller than 34 mm. The PDV probe provides a robust return with a minimum of alignment for metallic flyer plates. Existing preparation practices for flyer plates (lapping and polishing to 1200 grit) may be used. The projectile impact face is traceable for approximately 50 μs before impact. The velocities observed are nearly constant,

the powder charge is completely burned, and the projectile sails down the barrel. Averaging the 10 μs of velocity record preceding impact results in measured velocity accuracy of $\pm$ 1 $^{m}/_{s}$. Previous attempts at measuring impact velocity with staggered shorting pins and calibrated beam breaking systems were only capable of velocity uncertainties on the order of 10 - 50 $^{m}/_{s}$ with the current fixturing and target holders. Difficulties included measuring the pin spacing, and electrical noise in the observed beam breaking data.

A new fixture for target holders has been developed to replace the V-groove steel assembly used earlier. Independent adjustments in X (barrel axis), Y (horizontal), and Z (height) have been implemented, along with target face tilt adjustment from the downrange side of the target holder fixture. X and Y axis slides enable rapid alignment and repeatable placement during set up. The target holder may be removed from the fixture without any fixture disassembly after each alignment step to prevent damage, saving time. A schematic of the fixture is shown in Figure 3.14.

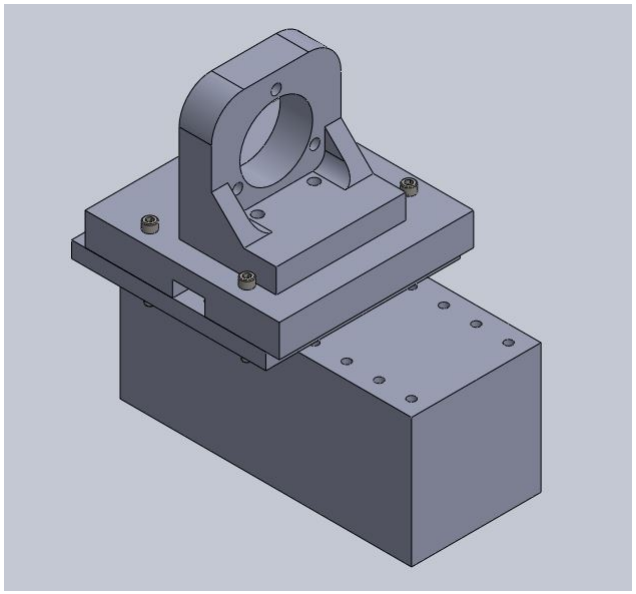

Figure 3.14: Target fixture - uprange is toward upper left corner.

3.2.3 Target Preparation Considerations

The key to obtaining high quality PDV data is to start with a properly prepared specimen. Fortunately, most metallic surfaces are great reflectors of infrared radiation. Very little additional

preparation for PDV use is required for these targets. So long as the surface is not specular (if it is, lightly scuff it with 1200 grit sand paper), the response level of returned light should remain roughly constant through the duration of the experiment. Using a specular surface presents possible light return issues following shock breakout. Unless the surface is perfectly orthogonal to the axis of the focusing of collimating probe, it will be difficult to realize a reasonable return. If a strong return is observed from a specular surface and the oscilloscope voltage range and PDV attenuators set for that return, any tilt introduced during shock breakout will result in greatly reduced returns and a decrease in signal to noise. Low signal to noise reduces absolute velocity measurement confidence as explained later in Equation 3.31.

Light entering the collimating lens must get focused down into a 9 μm diameter glass fiber core. Any tilt of the rear surface changes the angle of incidence of the reflected light on the probe lens and reduces the light that is coupled into the fiber. Assume that the focal distance of the probe lens is approximately f = 6 mm. Ideally, the light entering the probe will come in parallel to its optical axis. If the rear surface tilts and is specular, most of the light originally entering the probe will then be entering the probe at an angle α to its optical axis (some light remains parallel to the optical axis due to diffuse scattering, but it will be neglected for this exercise).

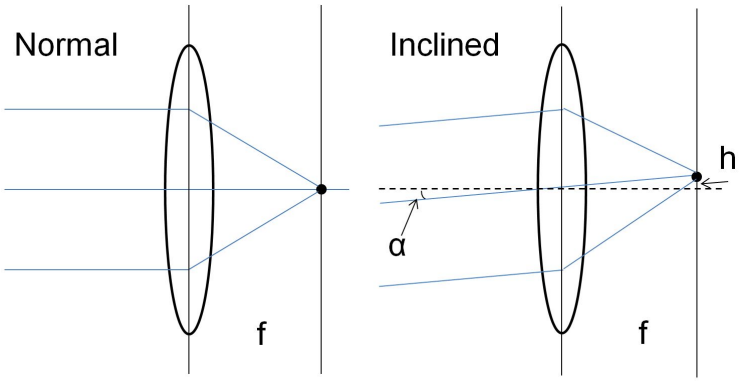

Figure 3.15: Ray traces for thin lenses: normal incidence (Left) and tilted reflector (Right).

A properly focused beam with normal incidence will direct the center of the focused beam onto the center of the cleaved fiber inside of the probe housing. The focused beam doesn't focus exactly to a point — the spot of light had a finite diameter, defined by the diffraction limit of light. The

angular width subtended by the tails of the spot (also known as the central or brightest peak, or Airy disk) is given by [15]:

$$\theta = \frac{1.22\lambda}{D} \tag{3.5}$$

The quantity D is the first location of zero intensity of the interference pattern. The central peak and its motion is illustrated in Figure 3.16. When the light coming into the lens is tilted, only light in

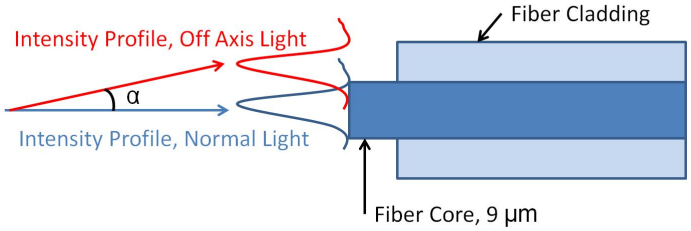

Figure 3.16: Central fringe light intensity profiles for normal and off axis light entering PDV probes.

the tail of the intensity distribution is coupled into the fiber. The width of the intensity distribution through the collimator at a 6 mm focal length is approximately 12.6 μm. If a Gaussian approximation for the intensity profile is used, the Gaussian width, or standard deviation, is given by $\sigma = .42\lambda/D$ in radians, which subtends 2.17 μm at a 6 mm focal length. The 9 μm fiber is illuminated with 95.4% of the intensity in the central fringe. If the center of the intensity distribution moves by 4.41 σ [10], then there will only be 1% of the original light intensity remaining. A 99% loss is the same as seeing a 20 dB drop in target light signal to the PDV photosensors. Back solving for α in Figure 3.15, the maximum rear surface angular deviation may be computed (assuming small angles):

$$\alpha = \frac{h}{f} = \frac{4.41 \times 2.17\ \mu m}{6000\ \mu m} = 1.6\ mrad \tag{3.6}$$

Therefore, it is imperative that diffuse surfaces be used to prevent complete signal loss under slightly less than ideal conditions. Since the rear surface of the model particulate composite is expected to ripple and deform upon shock breakout, the targets are scuffed before coating with a thin layer of higher impedance aluminum. Experience in this laboratory has shown that evaporative aluminum

coatings approximately 500 nm thick provide an excellent IR reflective surface without influencing the shock response of the material of interest. These coatings function well when applied to a flat surface lapped to 1200 grit. The surface is flat and smooth but the swirl marks from the sandpaper give the diffusively reflecting surface that is required.

3.2.4 Target Assembly Preparation

The target holder plate is machined in such a way as to require a certain order of assembly for the remaining target components in order to reduce impact tilt during the experiment. If tilt between the shorting pins, target, or probe is built in, no amount of pre-shot adjustment on the target fixture will correct it. Since all sensors and components must be indexed to the target plate, it should be the first component added to the target holder plate. Once the target plate has been lapped, polished, and treated with a reflective coating, the target holder pocket can be deburred. The target is then epoxied into the target holder. Orientation is as one would expect: reflective side in, towards the

Figure 3.17: Target plate and target holder.

probes that will be added later. Only a small amount of epoxy is required as shown in Figure 3.17. Too much will squeeze out onto the rear surface, or make a mess of the front of the target plate. Alcohol attacks the particulate composites, so removal of inadvertently applied epoxy to the target face will be difficult or impossible. Dried epoxy on the target face will damage the polished finish and introduce built in tilt issues since the target face may not lay perfectly flat on the set up jig. In order to fully seat the target plate and ensure it stays flat in the holder, weight is applied during curing, as shown in Figure 3.18. The same process applies to the assembly of the probe holder in

Figure 3.18: Weights applied during glue curing process.

the opposite side pocket. Probe holder plates are simply delrin inserts drilled and reamed to tightly hold probes during alignment. The same deburring process and weighting is used to ensure that the bore axis of the probe holder holes remain perpendicular to the rear surface of the target plate. Probes are then set once the probe holder plate is glued up, as described later in 3.2.5.1 and 3.2.5.2.

3.2.5 Probe Alignment

3.2.5.1 Active Probes

Active probes project and receive the interrogation and Doppler shifted light with the same fiber. The use of bi-directional traffic on a single fiber simplifies the design of the PDV probes. The device that makes the use of bi-directional traffic possible is the fiber optic circulator. The fiber coupled circulator is a recent development in the telecommunications industry used for separating inbound and outbound communications from the same run of fiber optic cable, reducing infrastructure costs and increasing bandwidth [45]. The PDV, as designed, is intended to be used with a single port for sending and receiving light. There is usually no power cut-off inside the PDV box — if the boosted laser is active, there will be emission from the front panel outputs. Each channel on the front panel, 1-4, has an FC-APC patch cable with a bulkhead fitting near the blast chamber of the Powder Gun for connecting the probes. Probes should always be connected to the patch cable, and never directly to the PDV box. The circulators are connected directly to the front panel of the PDV box. Repeated connecting and disconnecting may damage the circulator fiber connection, so a sacrificial patch cable

has been affixed for the express purpose of connecting probes. When the patch cable is damaged, it is far easier to replace than sourcing new (and expensive) circulators (Agiltron, Woburn, MA).

Alignment of active PDV probes is a very simple process, since it can be done without powering on the boosted laser. Optical return loss meters have been developed for use in the telecommunications industry to check fiber optic cable installs and broken cable runs. In order to test cables, the destination end is left unconnected and the optical return loss meter is connected to the source end. Optimal performance of the line requires that light sent into the source end does not get reflected back at imperfection in the fiber, or damage to the fiber face at the destination end. A calibrated source launches light into the fiber run, and reflected light is measured through a built-in circulator. The sent and received power levels are compared, and a relative loss value is displayed. ITU standards require losses of greater than -27dB [34], equivalent to measuring $^{1}/_{500}\ ^{th}$ of the output signal being returned to the source. Return loss meters are capable of measuring losses up to approximately -60 dB.

Unlike the telecommunications industry, experiments require that as much light intensity is returned as possible. To this end, an ORL-55 (JDSU, Milpitas, CA) "Optical Return Loss" meter is used to measure the percentage of light returned from the target in real time during probe alignment. Once the losses are made as low as possible, the approximate amount of drive power needed for adequate signal power to the PDV sensors may be computed. Drive power can be slightly higher than computed, with the extra light tuned down with the front panel attenuators.

With this method, the probe may be aligned and assembled outside of the chamber, and one single connection made to the PDV after it is aligned. The holes in the probe holder plate are reamed to be about .001 -.002 larger than the probe barrel so that they are held closely normal to the target surface. The tight fit will also give enough friction to hold the probes in place once a point of good return has been found. It is generally customary to monitor the loss during the application and curing of the epoxy bond to ensure that the probes have not moved within their bores. An example is presented in Figure 3.19. Figure 3.19 shows a four probe arrangement: three active probes on the rear surface of a target plate, and a single active probe immediately next to

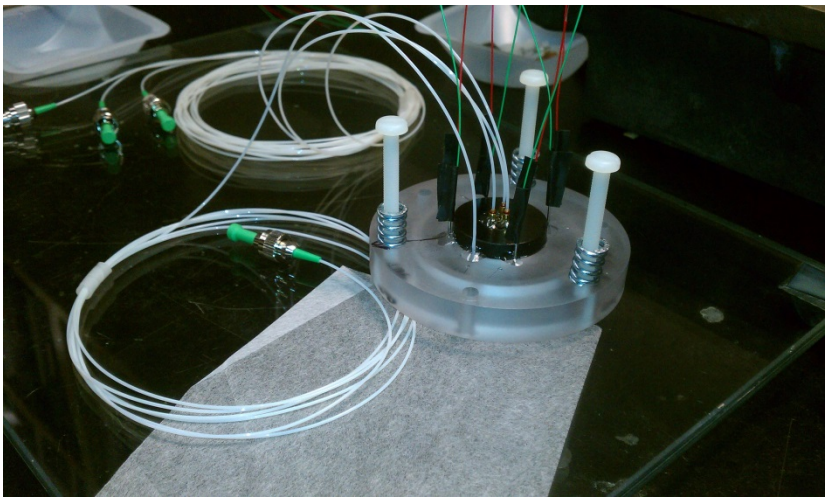

Figure 3.19: Probes glued into target holder assembly

the probe holder plate protruding completely through the target holder observe projectile velocity before impact. The probe looking down the barrel is capable of measuring impact velocity to $\pm$ 1 $^{m}/_{s}$. The velocity trace is apparent even up to 30 μs before impact. The probe can be set straight into the reamed hole immediately outboard of the target plate. It is typically set at the same time as the shorting pins.

A glass plate is cleaned and any protective coverings are removed from the impact face of the target. Four prepared tilt pins are placed in the 0.040 in. diameter holes such that they rest squarely on the glass plate, where they are epoxied in place. A collimating PDV probe is placed in the remaining reamed hole after the tilt pin epoxy is cured, to reduce the chance pf inadvertent tilt pin motion. Additional alignment of the down-barrel PDV probe is unnecessary before gluing.

3.2.5.2 Passive Probes

The use of passive probes with the existing PDV architecture requires special care both to align and take a measurement. As designed, the attenuators are placed after the doppler shifted light returns to the PDV box. Consequently, all channels get the same laser drive power, regardless of whether they are used or not, so long as the booster is on. Therefore, the laser drive on the passive channel must be eliminated outside of the PDV box without affecting the light collected by the probe. A device called an isolator is used for this purpose. The magneto-optical effect is used to modify the

polarization of the input light. Each light path is polarized differently, and then passed through birefringent crystals. Forward traveling light is refocused into a collimator, and reverse traveling light is diverged away and the power is dissipated as heat.

Alignment of these probes should also be done independently of the PDV box. In addition to the ORL-55 being used in a different mode, a power meter will be required. An active probe is placed and optimized as directed above and as shown in Figure 3.20. A laser source is affixed to the active

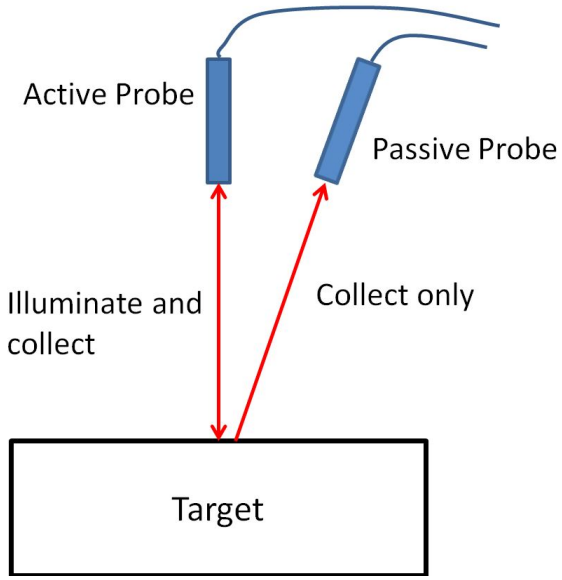

Figure 3.20: Comparison of active and passive probe operation

probe, at which point a power meter (JDSU OPM-34) can be used to measure the amount of the light exiting the active probe and being collected by the passive probe. The passive probe must be located in such a way that the power meter shows the maximum amount of optical power collected. Losses will be very high. In extraordinary cases, the PDV boosted laser may be required to provide enough light to align the passive probe.

3.3 Heterodyne Velocimetry

3.3.1 Interferometry Theory

Heterodyne Velocimetry, also commonly known as Photonic Doppler Velocimetry (PDV), is a time resolved velocity measurement technique, based upon the Michelson [47] displacement interferometer. The extreme sensitivity of the apparatus in two respects is of critical necessity to the investigation of structured shock waves. First, the fundamental displacement sensitivity of one half wavelength per fringe is responsible for the large amount of fringes seen in signal analysis. Secondly, the phase extraction methods are not as dependent on absolute magnitude of the interference record as other velocity interferometer architectures such as VISAR (Velocity Interferometer System for Any Reflector) [20]. The development and commercialization of high bandwidth oscilloscopes (4 GHz analog Bandwidth and above) and fiber coupled telecommunications equipment have made measurements of this type possible in university level research. Strand et. al [56] at Lawrence Livermore National Laboroatory were the first to construct a compact velocimeter using commercial off the shelf fiber coupled equipment and 1550 nm fiber coupled lasers. When constructed in this fashion, the PDV interferometer is entirely fiber coupled up to the probe, making it unnecessary to align or tune the interferometer itself before each use. There are still places where VISAR is superior, but the availability and simplicity of PDV probes makes it usable for a large variety of experiments.

The device in [56] is described as a heterodyne velocimeter. While this is acceptable terminology, this device uses a single laser source for both target interrogation and as a reference as shown in Figure 3.21. It is more correctly a homodyne velocimeter. Heterodyning is a signal processing technique where a reference signal is mixed to create a carrier on which the signal itself is superimposed [36]. The shift of the signal of interest into a different frequency range offers many advantages for the PDV. In Strand's device, probes are specified to give a certain amount of back reflection to provide the reference signal or a fiber splitter can be used. A true heterodyne velocimeter uses light of different wavelengths to interrogate the target and to function as a reference in order to create a

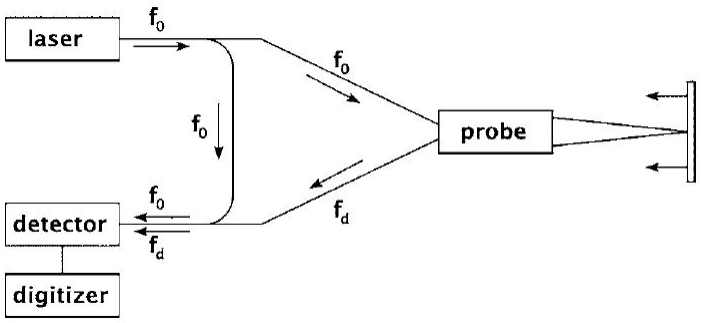

Figure 3.21: Homodyne PDV. Adapted from [56].

carrier. The difference in laser wavelength can serve any number of purposes — from multiplexing, to doubling the maximum measurable velocity of a system, or to shifting the measured frequency associated with zero target velocity.

Both arrangements use the fact that light, in a manner similar to sound waves, can have phase information encoded as it is reflected from a moving surface. While the absolute frequency of sound can be measured directly, no sensor exists to do the same for a light wave since

$$f_{light} = \frac{c}{\lambda} \approx O\left(10^{14}\right) \ Hz. \tag{3.7}$$

The electric field magnitude of light oscillates at frequencies on the order of terahertz, far above the analog bandwidth of any currently available sensors. Therefore, heterodynes generated by mixing light of two different wavelengths are required. More simply, the beat frequency of time averaged light intensity can be observed. Beat frequencies in PDV are related to the surface velocity of the reflector and the wavelength of the incident light by the following relation in the homodyne case [56]:

$$f_{beat} = \frac{2v}{\lambda} \tag{3.8}$$

At the simplest level, we can do some dimensional analysis to start our understanding of heterodyne velocimetry. Take the Michelson Interferometer sensitivity constant: for a given laser wavelength λ,

a motion of the reflector by a multiple of $^{\lambda}/_{2}$ gives one complete fringe:

$$2\Delta u = n\lambda \tag{3.9}$$

The fundamental sensitivity of the interferometer can be realized by rearranging:

$$Sensitivity\left[\frac{\Delta u}{fringe}\right] = \frac{\lambda}{2}\left[\frac{nm}{fringe}\right] \tag{3.10}$$

At this point, an assumption must be made about the velocity and its variations over time. In order to make conclusions about the instantaneous frequency of the signal, the method used to determine that frequency must be considered. In the interest of simplicity, the instantaneous frequency will be determined through the use of the Short Time Fourier Transform (STFFT). The STFFT window length will be on the order of nanoseconds with sampling rates of approximately 20 GSa/s. Over time windows of this sufficiently short length, the observed velocity should not be changing, and the frequency extracted can be directly related to the actual target surface velocity. Given an observed number of fringes over a short period of time in $^{fringes}/_{sec}$, the frequency can be related to the free surface velocity:

$$Sensitivity\left[\frac{\Delta u}{sec}\right] = v = \frac{\lambda f}{2} \Rightarrow f = \frac{2v}{\lambda} \tag{3.11}$$

The above approximate dimensional analysis gives the needed background for a definitive proof of the PDV principle. We would like to consider a window so small that the velocity within that window is approximately constant, such that the extraction of the spectral information contained by the fringes can be tied directly back to the velocity of the reflector. An appropriate starting point for this is with a discussion of optical path length, the quantity from which a change will produce fringes in a displacement interferometer.

Optical path length is the equivalent distance traveled in a vacuum by a ray of light as it passes through other mediums of varying optical index. In the case of the PDV, the only path length change happens outside of the fiber coupled components (ideally, that is; stretching of the fiber due

to vibration during the experiment is neglected). The light accumulates phase, Φ, over time as it covers distance, say from A to B, through a medium of given refractive index, n:

$$\Phi = \frac{2\pi}{\lambda} \int_A^B \mathrm{n(s)}\, \mathrm{d}s \tag{3.12}$$

In this case, the light is only outside of fiber in a vacuum during the experiment, so n=1 over the distance of interest. Therefore, a change in optical path length of Δd results in a phase change of:

$$\Delta\Phi = \frac{2\pi\Delta d}{\lambda} \tag{3.13}$$

Since we are interested in the phase change imparted on a beam illuminating a moving target, the target beam must be mixed with a reference beam in order to be able to sense the change with low bandwidth (relative to the frequency of light) sensors. It is advantageous to use light of a different wavelength as a reference beam to add a carrier signal to the final output. After some manipulation, the carrier frequency will appear explicitly in the final result. The reference beam is denoted by subscript R in the following analysis, while the subscript T signifies target light with encoded phase information related to its position. Consider the interference of two beams represented by their electric fields, $\mathbf{E}_R$ and $\mathbf{E}_T$:

$$\begin{aligned} \mathbf{E}_R &= E_{R0} e^{i(\mathbf{k}_R \cdot \mathbf{r} - \omega_R t + \phi_R)} \\ \mathbf{E}_T &= E_{T0} e^{i(\mathbf{k}_T \cdot \mathbf{r} - \omega_T t + \phi_T(t))} \end{aligned} \tag{3.14}$$

Each plane wave has a scalar magnitude "E_{i0}", a wave vector "$\mathbf{k}$", angular frequency "ω", and phase term "ϕ". The plane wave equations for the electric field give a convenient representation for combining the two waves in the 2x2 fiber combiner. The mixed electric field is simply the sum of the two individual fields:

$$\mathbf{E} = \mathbf{E}_R + \mathbf{E}_T \tag{3.15}$$

This mixed signal is recorded by the photo sensors at the end of the interferometer. The sensors have analog bandwidths of the order of GHz, five orders of magnitude less than the frequency of

the electromagnetic wave falling upon it. The recorded quantity is required to be the time averaged intensity of the electric field signal,

$$I = s\left|\mathbf{E}\right|^2 = s\mathbf{E}\cdot\mathbf{E}^* \tag{3.16}$$

The constant "s" is simply a proportionality constant and is unimportant, and the intensity can be computed by the product of the time varying electric field vector with its complex conjugate.

$$\begin{aligned} I &= s((E_R + E_T)(E_R + E_T)^*) \\ I &= s(E_R E_R^* + E_T E_T^* + E_R E_T^* + E_T E_R^*) \end{aligned} \tag{3.17}$$

The quantities $sE_iE_i^*$ are the DC intensities of the reference and target beams and may be simplified to I_R and I_T.

$$\begin{aligned} I &= I_R + I_T + sE_{R0}E_{T0}(e^{i(\Phi_R - \Phi_T(t))} + e^{i(\Phi_T(t) - \Phi_R)}) \\ I &= I_R + I_T + sE_{R0}E_{T0}(e^{i(\Phi_R - \Phi_T(t))} + e^{-i(\Phi_R - \Phi_T(t))}) \end{aligned} \tag{3.18}$$

A cosine identity is then applied to give:

$$\begin{aligned} I &= I_R + I_T + sE_{R0}E_{T0} \times 2\cos(\Phi_R - \Phi_T) \\ I &= I_R + I_T + 2\sqrt{I_R I_T}\cos(\Phi_R - \Phi_T) \end{aligned} \tag{3.19}$$

The phase information can be examined by considering the oscillatory part of the time averaged intensity,

$$\begin{aligned} I_o &= 2\sqrt{I_R I_T}\cos(\mathbf{k}_R\cdot\mathbf{r} - \omega_R t + \phi_R - \mathbf{k}_T\cdot\mathbf{r} + \omega_T t - \phi_T(t)) \\ I_o &= 2\sqrt{I_R I_T}\cos((\omega_T - \omega_R)t + (\phi_R - \phi_T(t)) + (\mathbf{k}_R - \mathbf{k}_T)\cdot\mathbf{r}) \end{aligned} \tag{3.20}$$

The second part of Equation 3.20 represents a simplified form of all of the information contained in the oscillatory component of the PDV signal measured using an oscilloscope. The term $\phi_T(t)$ contains the encoded phase difference from the motion of the reflector. In the case of shock experiments, the reflector will be accelerating toward the probe. Due to the fact that the light travels to the reflector and back, a change in displacement of Δd is equal to twice the displacement of the reflector, or $2u$.

Since we may choose our origin for measurement in any way that pleases us, we will call displacement of the reflector towards the probe negative, while motion away from the probe will be positive, as shown in Figure 3.22.

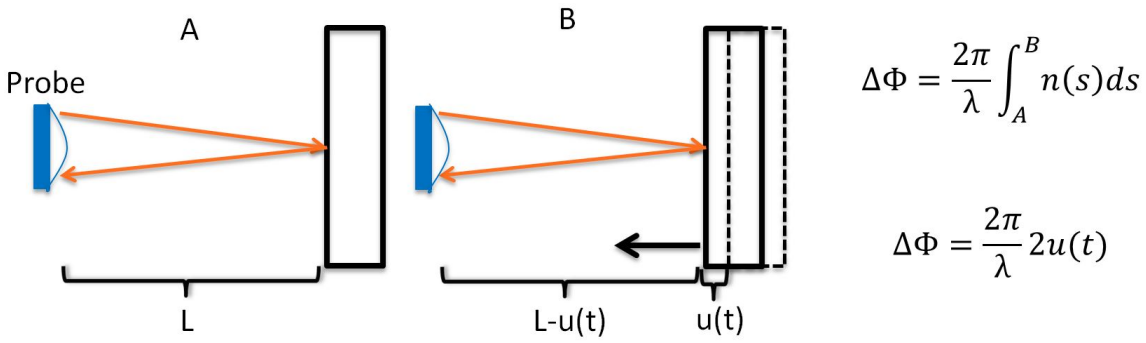

Figure 3.22: Optical phase dependence on path length change.

The intensity can then be expressed as,

$$I_o = 2\sqrt{I_R I_T}\cos\left((\omega_T - \omega_R)t + \left(\phi_r - \left(\frac{2\pi 2u(t)}{\lambda_T} + \phi_{T0}\right)\right) + (\mathbf{k}_R - \mathbf{k}_T)\cdot\mathbf{r}\right) \tag{3.21}$$

Equation 3.21 now accounts for all signal components present in the upshifted PDV signal; there are static fringes at zero reflector velocity, and an additional phase shift due to reflector motion. Unfortunately, the information encoded in the continuous phase is the displacement u(t), not the velocity. Numerical differentiation and the noise involved with the process can be avoided with velocity analysis.

In order to justify the dimensional analysis in Equation 3.11, we must look closer at the phase information in the cosine term and create our own short time analysis window, from which the velocity of the target surface can be deduced.

$$\Phi(t) = \left((\omega_T - \omega_R)t + \left(\phi_r - \left(\frac{2\pi 2u(t)}{\lambda_T} + \phi_{T0}\right)\right) + (\mathbf{k}_R - \mathbf{k}_T)\cdot\mathbf{r}\right) \tag{3.22}$$

By multiplying the phase term by $1 = {}^{\Delta t}/_{\Delta t}$, where Δt is the time over which the surface displace-

ment is acquired, the phase can be written as,

$$\Phi(t) = \left((\omega_T - \omega_R)t + \left(\phi_r - \left(\frac{2\pi 2u(t)\Delta t}{\lambda_T \Delta t} + \phi_{T0}\right)\right) + (\mathbf{k}_R - \mathbf{k}_T)\cdot\mathbf{r}\right) \tag{3.23}$$

The accumulated phase of reflector motion between time t and t+Δt is computed,

$$\Delta\Phi = \Phi(t+\Delta t) - \Phi(t) = \left((\omega_T - \omega_R) - \frac{2\pi 2}{\lambda_T}\left(\frac{u(t+\Delta t) - u(t)}{\Delta t}\right)\right)\Delta t \tag{3.24}$$

The instantaneous angular frequency of the signal can then be determined by sending the size of the "window" to zero:

$$\begin{aligned} \omega_s = \lim_{\Delta t\to 0}\frac{\Delta\Phi}{\Delta t} = \lim_{\Delta t\to 0}\left((\omega_T - \omega_R) - \frac{2\pi 2}{\lambda_T}\left(\frac{u(t+\Delta t) - u(t)}{\Delta t}\right)\right) \\ \omega_s = (\omega_T - \omega_R) - \frac{2\pi}{\lambda_T}2\dot{u}(t) \end{aligned} \tag{3.25}$$

Several quantities are renamed to make them more clear in the context of plate impact experiments. The quantity observed on the oscilloscope is frequency (from the voltage time record), which may be converted according to $\omega = 2\pi f$. As noted above, the shock particle velocity can be written as the opposite of the displacement of the reflector $\dot{u} = -v$:

$$f_s = (f_T - f_R) + \frac{2v(t)}{\lambda_T} \tag{3.26}$$

The leftover frequency from the difference in the wavelength of the target and reference beams is the "upshift" or "carrier" frequency. Now everything observed in the time history traces from the interferometer can be explained. There is a beat at zero target velocity, and instantaneous frequency increases with movement of the rear surface of the target towards the probe. The fundamental relationship of f=$^{2v}/_{\lambda}$ for the velocity is also recovered:

$$f_s = f_c + \frac{2v(t)}{\lambda_T} \tag{3.27}$$

Drive Laser Wavelength:	1550.012nm	
Reference Laser Wavelength [nm]	Beat Frequency [GHz]	Velocity Upper Limit [m/s]
1550.017	0.62	2616
1550.022	1.25	2133
1550.027	1.87	1649
1550.032	2.50	1166
1550.037	3.12	682

Table 3.5: Approximate PDV upshifts.

Typical settings for the carrier frequency are tabulated in Table 3.5 and are dependent on the maximum particle velocity that is expected over the course of the experiment.

3.3.2 Optical Power Requirements

The approach to sensor power will be the same as that employed at Sandia National Labs, as described by Dr. Dan Dolan. The bulk of the power to the sensor will be reference light to ensure a strong carrier signal. The oscillations due to the imposed phase change from target motion will then be superimposed on that baseline. 0 dBm (1 mW) is to be taken as the maximum detector power in order to prevent damage. The Miteq (Hauppauge, NY) sensors used in the PDV device exhibit non-linear response above that power level, and the voltage output can jump. The sensors saturate at +10 dBm (10 mW), and it is critical to keep power below this level at all times, or damage will result.

In terms of light return, it is usually adequate to get -20 dBm to -15 dBm of target light power from the probe. This level is generally very easy with purpose-made PDV probes and a prepared target surface. With a patch cable end used as a probe, efficiencies of -30 dB to -40 dB are likely, so more booster laser power may be needed to get to -25 dBm to -15 dBm at the sensor. Probe efficiency of -40 dB or worse (as measured on the ORL-55 during alignment, described in 3.2.5.1) can be used to achieve a successful experiment, but it is not ideal. Below the -40 dBm return power level, the light reflected at each of the fiber junctions or leakage through the circulator starts to become a significant power component of the observed signal. Good results have been observed with diffuse aluminum coated surfaces and probes set to 30 dB loss, as measured by the ORL-55.

Assuming a satisfactory return on the probe, a 100mW input to the probe gives -20 dBm (.01 mW) of target light to the sensor. -3 dBm of reference light is also an easily achievable quantity. The modulated intensity as a function of time is the quantity of interest:

$$I(t) = I_R + I_T + 2\sqrt{I_R I_T}\cos(\Phi(t)) \tag{3.28}$$

Base power is then .51 mW, and interfering power is .14 mW which determines the oscillation magnitude. Miteq sensors have a sensitivity of approximately 1000 V/W, giving and oscillation amplitude of about 100 mW. These numbers should provide a good starting point for making measurements with the PDV.

3.4 Data Acquisition

3.4.1 Timing Considerations

In the interest of compatibility with existing laboratory systems and instruments, the PDV and its supporting equipment were carefully chosen to ensure that if necessary it could run simultaneously with the existing interferometers and gauges. When multiple instruments are tied together and involved with capturing a single, rapid event, timing, skew, and delays become a significant issue. This is especially critical in shock physics experiments when wave transit times and stress gauge records must be synced to measure shock speed. The multiple instruments used to measure shock speed are completely independent, and in some cases may not be connected to the same digitizer and time base due to the limitations on bandwidth and number of digitizer channels available.

Typically, when more channels are needed, oscilloscopes can be daisy-chained together, with a single lead scope acting as a triggering device; sending out a pulse to the remaining oscilloscopes when it is triggered by a combination of specific inputs defined by the experimenter. This approach is not particularly robust, and is susceptible to errors introduced by skew and the splitting process. Different lengths of coaxial cables and the use of a trigger port that is not intended for such fast measurements (most sample on the order of 10's of MHz) can introduce difficulty in aligning the order of events observed on different digitizers. For such short time scales, events may possibly be missed completely if the delay is significant. In addition, some instruments require rapid sampling, while others can function with lower analog bandwidths and sample rates. The difference in sample rates can result in a timing skew between duplicated signals on the two oscilloscopes.

Therefore it is advisable to duplicate timing channels across all digitizers in order to remove the uncertainty introduced by uncharacterized timing circuits. A recent development in high rate digitizers is that of the mixed signal oscilloscope (MSO). A MSO carries an additional 16 bit bus that runs in parallel to the 4 analog inputs and on the same time base. The 16 bit bus can be separated into 16 individual high speed 1 bit analog to digital converters, with user defined thresholds. These "digital" channels, so named for the the fact that their output is binary, may also be used as triggers.

The digital channels on the Agilent MSO oscilloscopes operate at a "medium" impedance ($100k\Omega$), between the 50 Ω and 1 $M\Omega$ impedance of the analog inputs [1]. The outputs of the tilt pin mixer are high impedance and thus require high impedance observation circuits to keep the voltage signals in an observable range. The attenuation of the high impedance digital channels is minimal, and allows for the tilt pin outputs to be observed with multiple oscilloscopes without large voltage drops. In this way, when synchronization is needed between multiple instruments over different oscilloscopes, the timing signals from the pin mixer will be duplicated and on the same time base as the pressure gauge and velocity interferometer signals. Having 16 independent 1 bit ADC's allows for complete usage of the pin mixer if desired, as previous data acquisition systems were limited in the number of available analog channels available for pins.

Leaving analog channels for instruments enhances laboratory capability. 5 point surface velocity records are possible with simultaneous VISAR and PDV. The new triggering and timing architecture enables rapid expansion in instrument use without sacrificing the use of existing instruments by simply duplicating the pin timing channels for triggering, and ensuring that the observed time base on each oscilloscope can be correlated to the others with the duplicate signals. This capability is particularly useful in experiments involving heterogeneous materials, where spatial information about shock front disruption may be used to gain insight into scattering phenomena.

3.4.2 Shorting Pins

The use of shorting circuits to observe arrival of flyer plates and wave motion at interfaces has been in use for many years, starting with early shock physics experiments and the Manhattan Project [49]. As technology has progressed, timing systems have developed from simple wire circuits to purpose-built integrated devices that emit an electric pulse when a short circuit is detected. A Dynasen (Goleta, CA USA) CS2-50-300 mixer is used to detect impact induced shorting of Dynasen CA-1038 pins. The CA-1038 pin is comprised of a conductive center pin insulated from a conductive outer casing, and separated by a gap to a conductive brass cap. Upon impact or shock arrival, the cap yields to close a gap of approximately $.0025 \pm .0005$ in. (63.5 ± 12.7 μm) [5]. The mixer

supplies an excitation voltage to the center pin, which is detected upon shorting. Sensing of the short activates a fast RC circuit discharge into a summing circuit and the mixer output. The mixer's summing output is normally attenuated by 20 dB (1/100th of the input)[6]. It is desirable to use the summing output as the trigger signal such that recording will be activated if any one of the pins in use during the experiment is shorted, reducing the likelihood of a single defective pin destroying the measurement.

Due to the fact that the output is at 50 Ω and attenuated, the summing signal magnitude is too low in absolute voltage for reliable triggering, and ground spikes and other electromagnetic disturbances (EMI) can cause the oscilloscopes to trigger before the gun is fired. To eliminate this problem, the summing circuit was modified to increase the voltage output to a level that the trigger would not be tripped by EMI, as shown in Figure 3.23 below:

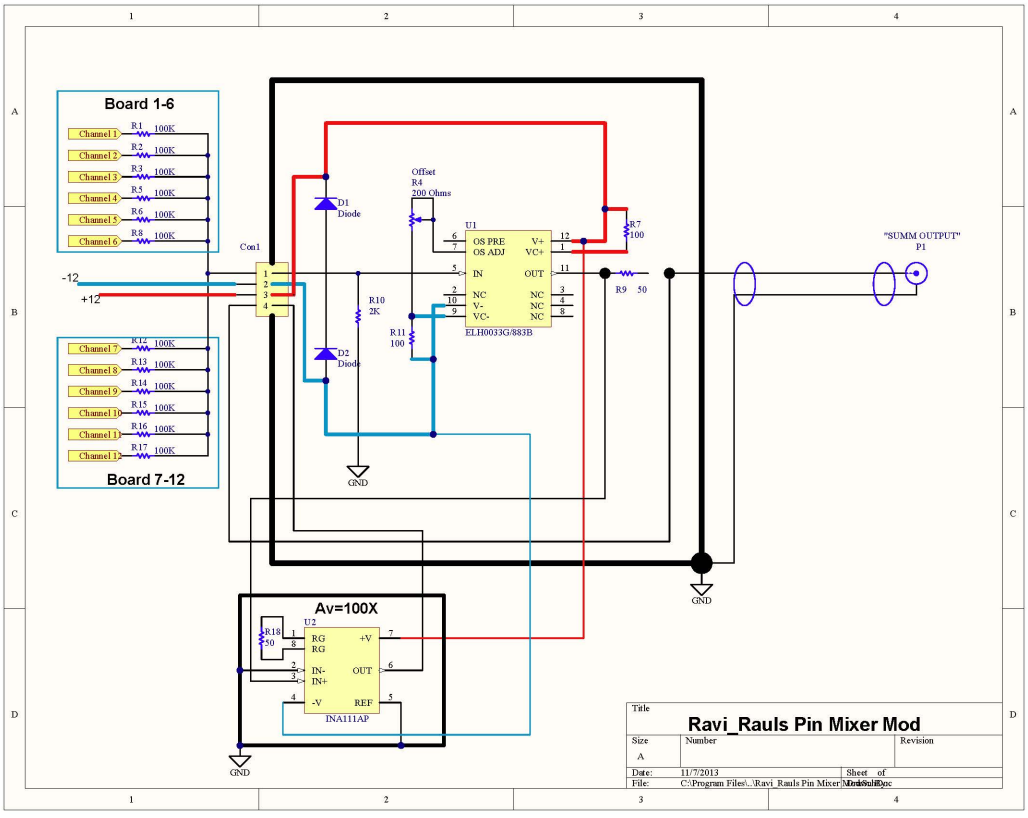

Figure 3.23: Circuit diagram for summation circuit modification.

The output of the original sum circuit is passed through a INA111AP 100x gain amplifier. The

bandwidth of the amplifier is rather low, so it does not readily duplicate the signal being put into it, but it spreads the pulse in time: The channels in Figure 3.24 are numerically labeled from top to

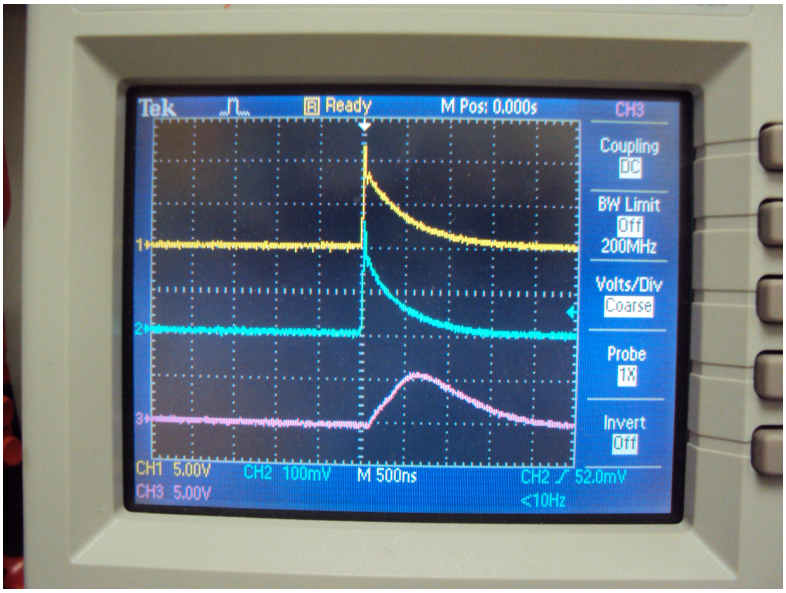

Figure 3.24: Analog waveforms from pin mixer.

bottom. Channels 1 and 3 have the same voltage scale of 5 V/div, while Channel 2 is the original summation circuit, with a scale of 50 mV/div. While the slew rate of the amplifier is too slow to pass the signal, the amplitude of the pulse is high enough for the trigger threshold to be at a reasonable EMI resistant level, and the rising edge will activate the trigger algorithm on the oscilloscope. Faster amplifiers exist for a higher price, but are not necessary at this time.

The shorting pins are used solely as time of arrival designators and for measuring the planarity of impact. PDV provides impact velocity. The shorting pins are glued up such that the faces of their caps are coplanar with the front surface of the target plate. This is accomplished by placing the target assembly face down on a flat glass plate and epoxying the pins in as they sit on the plate. Impact angle is measured as the difference between the target normal and the line orthogonal to one calculated from the shorting time of any two of the pins. This gives six possible unique planes, and the maximum is taken as the tilt assigned to the shot.

$$\alpha = 1000 \times \left| \arctan \left[\frac{V_I(t_i - t_j)}{R_{ij}} \right] \right| \tag{3.29}$$

Equation 3.29 gives the impact tilt in units of milliradians, where t_i and t_j are times of observed pin impact in μs, V_I is the projectile velocity in $mm/\mu s$, and R_{IJ} is the distance between the pins in mm. Experiments in this study only require an average time of arrival, and that α remains below a threshold value of 7.5 mrad, so no further analysis of the tilt direction is necessary. As explained in Section 3.2.2, the alignment procedure established with the vacuum chuck assembly is proven to meet the desired tilt. Tilt effects on the order of the threshold are generally negligible [13].

3.5 Data Analysis

The analysis of PDV signals in Section 3.3.1 yielded an analytic expression for the voltage time history observed on the oscilloscope record. The key components of the observed signal are the carrier and the phase shift due to reflector motion, that appears as a frequency change. The frequency change associated with a change in surface velocity of 77.5 $^{m}/_{s}$ is approximately 100 MHz at 1550 nm. The scattering phenomena present in heterogeneous materials under shock loading results in shock front spreading, on time scales of tens of nanoseconds. For reasonable analysis of a shock front 10%-90% rise time from 0-1400 $^{m}/_{s}$, changes in observed frequency on the order of tens of MHz must be precisely resolved over short time scales. The time resolution of frequency extraction is therefore dependent on getting enough information into a short time window to have confidence that the measured instantaneous frequency is the actual instantaneous frequency present in the signal. For the purposes of this experiment, the sampling rate, f_s, is held constant and is equal to 20 GSa/s. Best practices dictate that there should be at least one full period of the signal of interest within the short time FFT window.

Consequently, low velocities without a carrier will have periods of hundreds of nanoseconds. For composite targets with bead diameters of 300 μm and smaller, the velocity is changing rapidly over time periods of hundreds of nanoseconds. In the case of shock waves, the time resolution required at shock breakout is not adequate for un-shifted PDV. Adding a carrier to the observed signal reduces the signal period at zero target velocity. Therefore, a shorter window can be used allowing for much finer time resolution and better estimation of spectral make up. Table 3.5 shows the range of available upshift states for the PDV used in this study. In the case of a 1.25 GHz upshift, there will be approximately 4 or more cycles per 3 ns sliding analysis window (τ). Time resolution should be adequate to measure rise times on the order of 20 ns, while including enough information in the record to accurately gauge the spectral content within it. The velocity resolution is inversely related to the record length that is available in the window, excluding zero padding. Therefore, time resolution is a trade-off with velocity resolution.

The uncertainty principle, otherwise known as the Gabor Limit, specifies the relationship between

the frequency resolution and the window size and is given by Equation 3.30 [41].

$$(\delta v)(\tau) \geq \frac{\lambda}{8\pi} \tag{3.30}$$

The uncertainty product is greater than or equal to the quotient of the wavelength of the light used to illuminate the target and 8π. Consequently a window of length 1 ns will give an uncertainty of approximately 62 $^{m}/_{s}$. Steps to minimize this uncertainty with peak fitting and making the assumption that a single dominant frequency is present in the signal reduce the uncertainty to more reasonable levels, as is shown by Dolan in [31]. The parameters used to analyze velocity history data are as follows in Table 3.6:

Sample Rate	20	GSa / s
Window Length	64	Samples
Window Overlap	50	%
Window Function	Hamming	
Window Length Padded with Zeros	32768	Samples

Table 3.6: PDV record analysis parameters.

The estimated uncertainty can then be written [31]:

$$\delta v = \frac{\lambda}{2}\left(\sqrt{\frac{6}{f_s}}\frac{\sigma}{\pi}\right)\tau^{-3/2} \tag{3.31}$$

Assuming that the noise fraction is a worst case 10 % of the PDV record signal, the uncertainty in the velocity becomes a far more reasonable 2.36 $^{m}/_{s}$. In addition, the further away from DC the carrier is, the better the estimate of the velocity. This is due to the decrease in signal to noise ratio for larger wavelengths, where only a partial fringe may be present in the window region. Uncertainties in velocity are then on the order of less than 1 % for most experiments.

Data records were chosen with high signal to noise and processed with the above parameters in PlotData, a PDV and VISAR analysis tool from Sandia National Laboratory, written by Dave Wackerbarth. A simple peak finding algorithm is used to determine shifted instantaneous velocity, and the pre-shot measured upshift velocity is then subtracted from the record to give the final time

resolved velocity profile. Statistics such as shock width, 10% - 90% rise time, and shock speed are then computed and averaged from the multiple points measured for each target. Standard deviations are presented with each measured quantity to offer insight into the precision confidence of the value.

Chapter 4

Numerical Simulation Methods

4.1 CTH Shock Hydrocode

Sandia National Laboratories "CTH" Shock Hydrocode simulation software was used for experiment planning and computer aided analysis of the PMMA and glass bead composites in this study. CTH is a combined Eulerian-Lagrangian solver sequence used to simulate propagation of stress waves in solids and fluids. A one-dimensional version was developed at Sandia in 1969 called Radiation-Diffusion Hydrodynamic Code (1D) (CHART D). A 2D version of CHART D was developed in 1975, CHART D^2 (CSQ). CSQ was re-written in 1987 to include additional material models and 3D support as $CSQ^{3/2}$ (CTH). A grid spacing is defined, and the grid is populated with the materials of interest in the proper locations in order to create a composite geometry. Cells that contain a material boundary are defined with a volume average of the two constituents.

Time steps are chosen such that a propagating disturbance does not move by more than 0.6 of the width of a computational cell. This criteria is known as the Courant stability condition and ensures code and mesh stability. With this in mind, at each time step, the Lagrangian equations of motions are solved, yielding a distorted version of the original mesh. The material motion is then remapped back onto the original Eulerian mesh and the material properties in each cell are updated with the current volume fractions, velocities, and pressures. The length of the next time step is checked to make sure that the Courant stability condition is not violated. The code then moves forward one time step, solving the Lagrangian equations of motion and repeating the update process.

A two-dimensional simplification of the three-dimensional plate impact problem was implemented in CTH. A center "section" view was selected to give a rectangular domain with a vertical dimension given by the plate diameter, and the horizontal dimension given by the plate thickness. Discussion of particle size and placement choice is presented below. Once the bead sizes and locations are determined, they are inserted into the geometry with an "insert circle" command in the CTH input deck. Materials that are added earlier in the input deck have precedence over overlapping materials added later, which simplifies the geometry generation. The PMMA matrix of the particulate composite under investigation is defined with an "insert box" command that covers the entire rectangular domain of the target plate, filling in the gaps between the particulates. An aluminum flyer plate is then defined in the up range direction, and given an initial down range velocity, i.e., impact velocity.

The computational domain extends up range and down range of the flyer/target assembly in order to ensure the free surface condition. The mesh is updated and extended automatically as the simulation progresses and the target plate begins to move down range. The top and bottom of the geometry (the radial free surfaces of the target plate) have a defined boundary condition to minimize wave reflections and best mimic experimental conditions. The parameter used to define them is boundary condition 2: Outflow Boundary Condition - mass may leave the mesh, and this may be used to simulate a free surface. The outflow condition is not subject to a constant pressure, since the confinement from the target holder is not strong. The mesh used in the experiment has a pitch of 20 μm, giving at least five cell widths across each bead. The nodal pitch is maintained constant through all simulations. A convergence study was undertaken, and it was determined that the increased computational time of smaller nodal pitches did not offer any additional resolution increases over 20 μm.

Information is extracted from the simulation results in the form of tracer particles. These are Lagrangian tracers in that they follow the material as it flows during the experiment and current pressure, particle velocity, and position can be obtained. Bulk information dumps of the composition, particle velocity, and pressure of each computational cell are also reported. The reported rise times are computed from tracer data, while the pressure and geometry maps presented in Section 5.1.1

were generated with the CTH package SPYMaster from the SPCTH information dumps.

4.2 Geometry Generation

Simulation geometries were chosen to match the experimental cases as closely as possible and match the dominant length scale and volume fraction. Creating a two-dimensional analog of a three-dimensional composite requires some assumptions about the conversion between volume fraction and area fraction. It has been shown that the area fraction of inclusions $< A_A >= {}^{A_{inclusions}}/_{A_{Plane}}$ on a plane through a sufficiently random material of interest is equivalent to the volume fraction of particulates in the whole sample $< V_V >= {}^{V_{inclusions}}/_{V_{sample}}$ [8] [16]. The area fraction alone is not enough to determine the number of beads to be inserted in each simulation geometry. Since the objective of the study was to determine the scaling of rise time with respect to some fundamental length scale, the diameter of the beads inserted in the two-dimensional geometry was chosen to match the diameter of the beads present in the experimental samples. Doing so simplified geometry generation and directly correlated the simulation cases to experiments.

Once the volume fractions were determined and bead diameters chosen, the number of beads to be inserted was computed to be:

$$n_{beads} = Floor\left[\frac{V_A h_{target} t_{target}}{\frac{\pi d_{mean}^2}{4}}\right] \tag{4.1}$$

A floor function is applied to the ratio of area fraction of glass beads desired and the area occupied by a representative bead, represented by its diameter d_{mean}. Area fraction is given by V_A multiplied by the area of the simulation domain computed by multiplying its height h_{target} by its thickness t_{target}. The mean bead diameters were chosen based on the available sieve screens described in Table 3.4. The center of the range was defined as the mean, and the diameter distribution was assumed to be uniform across the range. No bead diameters outside of the sieve range were permitted. A uniform diameter distribution was used since the sieved ranges fell near the center or tails of the assumed distribution of the as received bulk beads. A Gaussian distribution for bulk bead diameter

distribution was assumed. Consequently, the slope of the Probability Distribution Function for bead diameter in the bulk beads should be nearly flat at the center and tails for a wide size range.

A column vector of n_{beads} bead diameters was generated with a uniform random variable implemented in Matlab (Mathworks, Natick, MA). The use of a uniform random variable prevented concentration of bead diameter near one side of the bounds. The number of beads inserted in the simulation geometries ranged from nearly 30,000 for the 100 μm diameter beads to approximately 100 for the 1000 μm diameter beads.

The micrograph presented in Figure 3.2 shows an evenly dispersed random arrangement of beads within the PMMA matrix. This condition is required to replicate the assumed interface conditions in materials of interest such as high strength concrete, as well as simplify modeling efforts. Consequently, friction at interfaces may be neglected. Frictional forces play a significant role in response of granular media [23], so simplifying and removing their effects from the modeling allows for the study of effects due only to particle size.

Bead center locations were also generated with two independent uniform random variables. A non-overlap condition was enforced by a brute force check method. After each bead location was determined, a script looped through all previously placed beads to ensure that the new point was no closer to any previous point than one mean diameter. While inefficient, this process was only run once per geometry.

A series of analyses using bi-modal bead distributions was also completed using similar geometry generation. The larger beads in the distribution were placed first, according to the preceding algorithm. Then, a interstitial bead center location was generated (the smaller of the two bead sizes present in the composite). A series of checks was then completed to ensure that the non overlap condition was satisfied. Each new interstitial center point is checked against the larger beads, after which it is checked against the newly added interstitial bead centers. Consequently, the interstitials become the filler in the gaps between the larger beads, as one would expect to see resulting from a mixing process. A center picking interference check is presented in Figure 4.1.

Once the bead centers and diameters have been determined, a text file must be generated to be

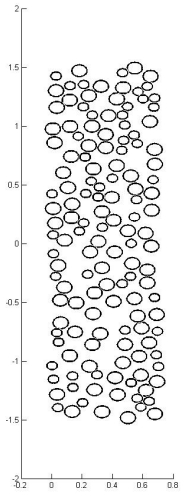

Figure 4.1: Bead center location interference check for for 1000μm glass beads with 700 μm interstitials.

inserted into the CTH input deck. Matlab and its loop and incrementing capabilities are employed to assign every bead in the simulation an integer number between 1 and 4. Each of the four bead groups is assigned as a different material in CTH with identical material properties. Since the bead locations have been randomly generated and are not ordered by position in the column vectors, breaking the beads up into subsets reliably ensures that most beads do not have neighbors that are members of the same subset.

The volume fraction based mechanical property computation used by CTH will "weld" cells of the same material together when contact is made and eliminate the interface when they begin to occupy the same computational cell. As silica glass is not known to weld together at these pressures and temperatures, eliminating this modeling artifact is an important part of the geometry generation process. Inputting beads in as multiple groups with identical mechanical properties tends to preserve interfaces with higher fidelity (or at least as well as is possible with CTH).

Sample geometries for a single mode simulation and a bi-mode simulation are presented in Figure 4.2. The empty rectangle to the left of the composite samples shown is occupied by aluminum, and is given an initial velocity corresponding to the experiment that is being simulated. The aluminum flyer plate in the simulations was 7 mm thick, and extends past the left hand field of view in Figures

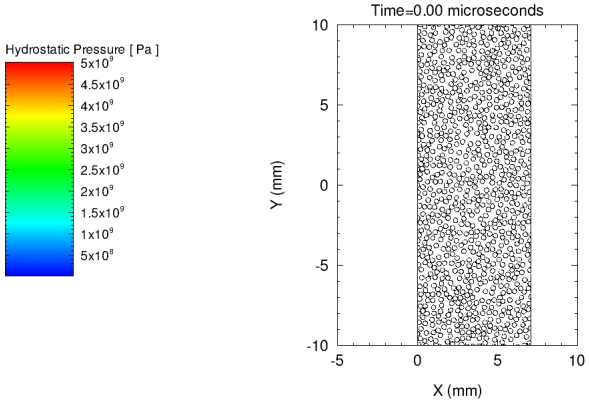

(a) Sample geometry for 300 μm beads.

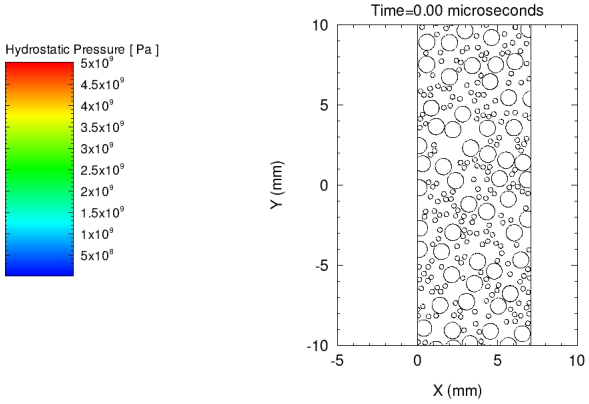

(b) Sample Geometry for 1000 μm beads with 300 μm interstitials.

Figure 4.2: Sample simulation geometries for CTH.

4.2a and 4.2b to ensure that the composite target remains in compression through the duration of the experiment. In the single mode and bi-mode bead experiments, the flyer velocity is 1000 $^{m}/_{s}$.

The field of view in Figure 4.2 and all following simulation pressure maps has been zoomed in to show detail. The full geometry mimics the experimental target diameter to preclude release waves from the edges reaching the tracer locations during shock break out and for sufficient time afterwards to measure the Hugoniot state.

4.3 Material Models

The material models used in the simulations in this study are all considered primary models in CTH. CTH primary model interface guidelines are models that are self contained, and do not call information from other Equations of State (EoS) models that may be present in CTH or other shock hydrocodes. The two EoS models used in this study are the SESAME and MGRUN models. The SESAME model is employed to describe the mechanical behavior of the glass bead particulates and MGRUN is used for the aluminum impactor as well as the PMMA matrix of the composites.

Silica glass is a well studied material, and a significant body of experimental data exists on its response at high pressure. The pressures of interest in the present study tend to be at the lower range of those studied. The use of a SESAME tabular EoS allows for the most general representation of the material. It is best with materials that are too complex to be described by a simple model, or are being investigated in loading regimes away from those in typical experiments. A built in table of temperature, density, and pressure is available, and called by setting the material to FUSED_QUARTZ in the CTH input file. Initial temperature and density are taken from the input file. No modifications to the built in material properties are made. State variables are interpolated between given values in the pre-programmed SESAME tables.

Both the PMMA and the aluminum use a separate primary EoS: MGRUN. The MGRUN model in CTH provides a means of fitting Hugoniot data to an analytic expression. The Hugoniot data has been fit to the Mie-Grüneisen equation [2]. The Grüneisen function, Γ, is defined as the dependence

of pressure on internal energy at constant density:

$$\Gamma = \rho^{-1} \left(\frac{\partial P}{\partial E} \right)_{\rho} \tag{4.2}$$

The Grüneisen approximation is that Γ is only a function of density. Solving for pressure gives:

$$P(\rho, E) \approx P_H(\rho) + \Gamma(\rho)\rho \left[E - E_H(\rho) \right] \tag{4.3}$$

The CTH implementation of the Grüneisen formulas further assumes that Γ and the specific heat, C_V (used for temperature calculations), are constant. The values P_H and E_H fall on the measured material Hugoniot. So long as the study remains within the pressure ranges explored by previous experiments that were used to fit the Hugoniot, the MGRUN model offers rapid, accurate computation of state variables. The parameters used to seed the models are given in Table 4.1.

Material	Density $[\ {}^{g}/_{cm^3}\ ]$	Hugoniot Intercept $[\ {}^{km}/_{s}\ ]$	Hugoniot Slope	Grüneisen Parameter
6061_ AL	2.703	5.240	1.400	1.97
PLEXIGLAS	1.186	2.598	1.516	0.97

Table 4.1: Mie-Grüneisen model parameters for PMMA used in CTH simulations.

Material strength models were also implemented for all materials in the simulation. A visco-elastic plastic (VEP) model was used for PMMA, a Steinberg-Guinan (SG) model used for aluminum, and a user defined model for the glass particlates. The VEP model in CTH is a parallel Maxwell model [4]. VEP is capable of resolving both quasistatic material behavior as well as rate dependent viscoplasticity via parallel Maxwell elements. A shear "spring" with an initial modulus is employed to capture the low strain rate response. Up to five parallel Maxwell elements (consisting of a series "spring" and dashpot) are available in the model. A schematic of the model is presented in Figure 4.1.

The quasistatic shear modulus is represented by the quantity G_0. Subsequent G_n and μ_n in the Maxwell elements are calibrated to experimental data at various strain rates so that the model is

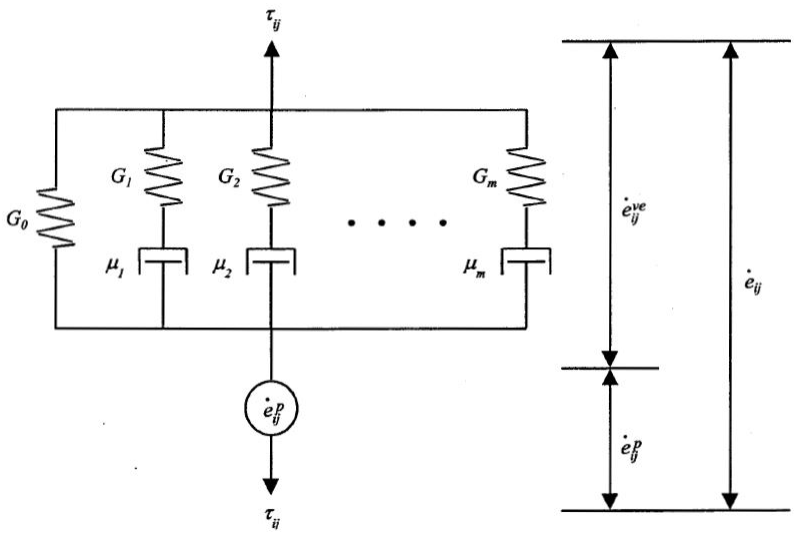

Figure 4.3: VEP Parallel Maxwell model with quasistatic shear spring. Adapted from [4].

applicable to as many loading cases as possible. A separate set of VEP coefficients is available for each of the five components of deviatoric stress. The VEP model is also capable of accumulating damage and updating the material properties and maximum available shear resistance. Deviatoric strain rates are allowed to approach zero as the material becomes fully damaged, but it can still support some shear stresses when loaded in hydrostatic compression after damage. The constitutive relation for shear stress rate is then:

$$\tau'_{\mathbf{0}} = 2G_0\dot{\mathbf{e}}^{ve} \tag{4.4}$$

$$\tau'_{\mathbf{m}} = 2G_m\left(\dot{\mathbf{e}}^{ve} - \frac{\tau_{\mathbf{m}}}{\mu_m}\right) \tag{4.5}$$

The stress rates are integrated with an Euler method to determine stress as a function of time. The material model inputs for PMMA are presented in Table 4.2.

Quantity	Value	Units
Density	1.186	$^{g}/_{cm^3}$
Poisson Ratio	0.4	-
Quasistatic Shear Modulus	$1x10^{10}$	$^{dyne}/_{cm^2}$
Maxwell Shear Modulus 1	$3x10^{9}$	$^{dyne}/_{cm^2}$
Maxwell Shear Modulus 2	$2.5x10^{9}$	$^{dyne}/_{cm^2}$
Maxwell Damping Coefficient 1	$3x10^{3}$	$^{dyne\cdot s}/_{cm^2}$
Maxwell Damping Coefficient 2	$4x10^{2}$	$^{dyne\cdot s}/_{cm^2}$

Table 4.2: VEP model parameters used in CTH simulations [4].

A validation that the model parameters built into CTH were adequate in describing the shock response of the molding grade PMMA was performed. Three experiments on pure molded PMMA without particulates were performed at 800, 1000, and 1200 $^{m}/_{s}$ impact speeds with an aluminum flyer. The free surface velocity profiles obtained using PDV are shown below in Figure 4.4. Bolded

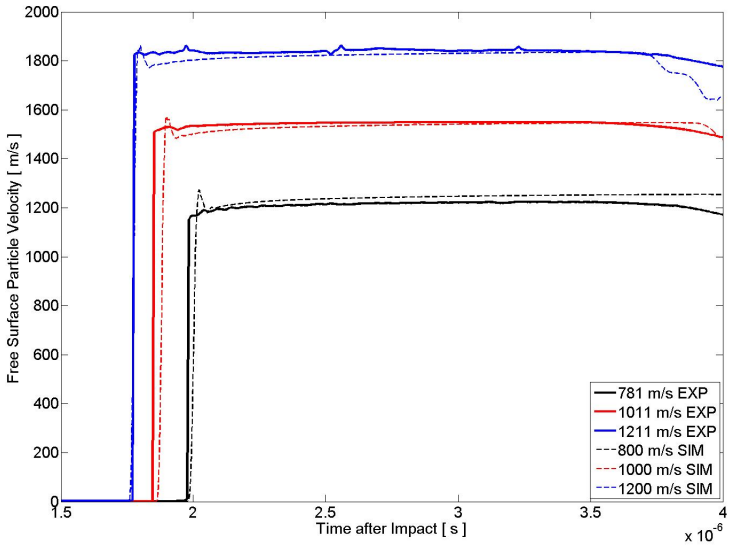

Figure 4.4: PMMA simulation parameter validation. Solid traces are from plate impact experiments and dashed traces are from CTH simulations.

wave traces are the measured shock response, while the thinner traces are simulation tracer data. Other than a tracer location artifact on the leading edge of the simulation data, the time of arrival, steady state particle velocity, and shock wave structure are very similar. The measured Hugoniot of

$$U_s = 2.786 + 1.329u_p \tag{4.6}$$

with velocities in $^{km}/_{s}$ compares favorably with the Mie-Grüneisen model parameters in Table 4.1.

The aluminum flyer plate uses a Steinberg-Guinan-Lund viscoplastic model. This model takes into account strain hardening, strain rate dependency, and pressure dependent shear strength [3]. A general failure surface was used for the glass particulates, as no significant plasticity is to be expected in brittle materials. A high melt temperature was input to prevent melting, and a Poisson's ratio of 0.17 was used for glass.

Chapter 5

Results

A series of simulation based experiments were undertaken for single mode bead diameter distribution composites comprised of 30% - 40% glass by volume. The initial simulation results were used to determine the appropriate bead diameter range for experimental observation, as well as to assist in the classification of shock front disruption regimes. Shock front disruption is quantified from transmitted wave profiles observed with heterodyne velocimetry, and scales linearly with increasing monodisperse bead diameter. Bi-modal bead diameter distribution composites were also examined. An analysis of the the limitations of the use of simple shock hydrocodes for composite analysis is presented.

5.1 Single Mode Bead Size Distributions

An initial parametric study was undertaken to determine the scaling of the shock front disruption, as measured by the observed shock wave rise time on the rear free surface of a particulate composite subjected to planar plate impact. Composite mixtures of 30% and 40% glass particles by volume were impacted at a velocity of approximately 1000 $^{m}/_{s} \pm 1\%$ by a 7 mm thick 6061 aluminum alloy flyer plate. Nominal stresses of approximately 4 GPa were imposed over a long (6 μs) pulse width. Monodisperse beads were obtained at 5 discrete average bead diameters, for a total of ten individual shock wave experiments. As described in Section 3.2.5.1, three separate wave profiles were obtained per experiment using PDV to determine the level of spatial heterogeneity and provide error bounds on the measured shock rise times. Initial CTH calculations were performed to plan the ideal bead

diameters to explore.

5.1.1 Simulation Results

Model and geometry parameters are discussed in Section 4, where a sample with randomly placed particulate composite geometry is presented. The randomly generated microstructures are subjected to a 1 $^{km}/_{s}$ impact by a 6061 Aluminum alloy at time $t = 0$. Bead diameters were chosen to cover the particle size range prescribed by composites of interest in the appropriate impedance mismatch region of Figure 2.14. Five test cases were chosen to determine if there was a strong dependence of rise time on average bead diameter for monodisperse bead distributions. Based on manufacturing constraints observed in preliminary studies, two volume fractions were chosen. PMMA and glass composites of 30% glass by volume and 40% glass by volume were simulated. As mentioned in Section 4, equal area fractions of glass were used as a stand-in for volume fraction in order to simplify the simulation to a more time-efficient two-dimensional geometry. This allowed for the dominant length scale (the mean bead diameter) to be present in the simulation.

The choice of 30% and 40% glass by volume composites was also motivated by the body of previous work where volume fractions of particulates in experiments rarely exceeded 50% (see references in Figure 2.14). Particle size bounds were chosen based on mesh screens available at popular US tool supply companies, and size spreads range from 10 μm to 50 μm. Bead diameters were chosen with a uniform distribution between the given bounds and their centers were chosen with a uniform random distribution across the cross sectional area. The geometries used in the simulations are presented below for each case before impact occurs for the 40% glass by volume cases in Figures 5.1, 5.2, 5.3, 5.4, and 5.5. 30% by volume geometries are visually similar enough and hence omitted in the interest of space. As one would expect, so long as volume fraction is held constant, there are fewer beads and interfaces with increasing mean particle diameter.

The sample geometries were meshed in such a way that there were five cells across the diameter of the 100 μm beads. Meshes were kept constant with increasing bead size. Due to the fineness of the mesh, it is omitted from the following visualizations. The geometries below show only a small

portion of the 30 mm tall sample, centered around its centerline at y = 0 mm.

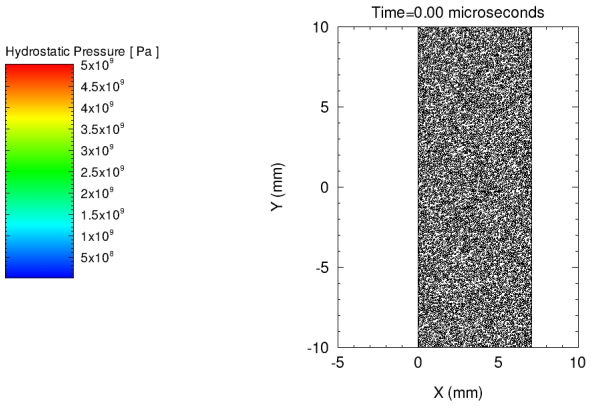

Figure 5.1: Initial 2D simulation geometry for 40% volume fraction 100 μm glass beads in a PMMA matrix.

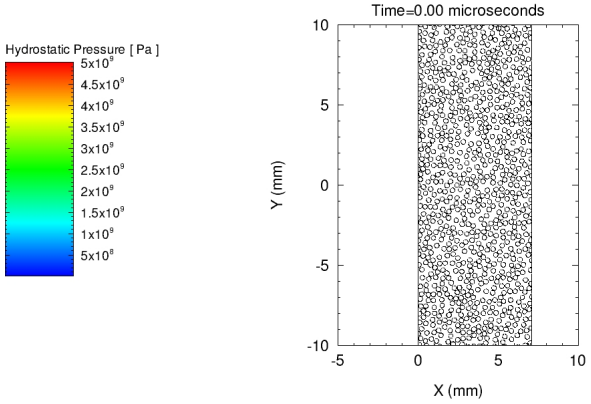

Figure 5.2: Initial 2D simulation geometry for 40% volume fraction 300 μm glass beads in a PMMA matrix.

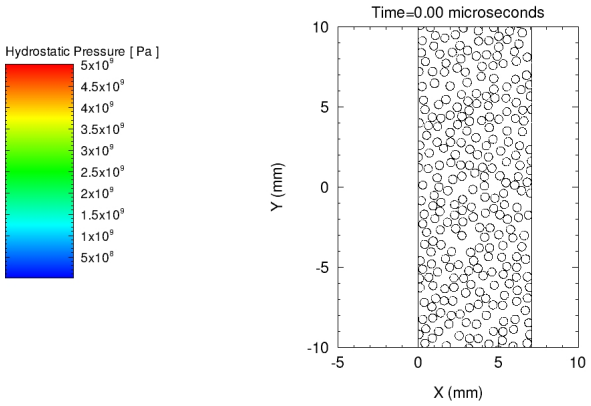

Figure 5.3: Initial 2D simulation geometry for 40% volume fraction 500 μm glass beads in a PMMA matrix.

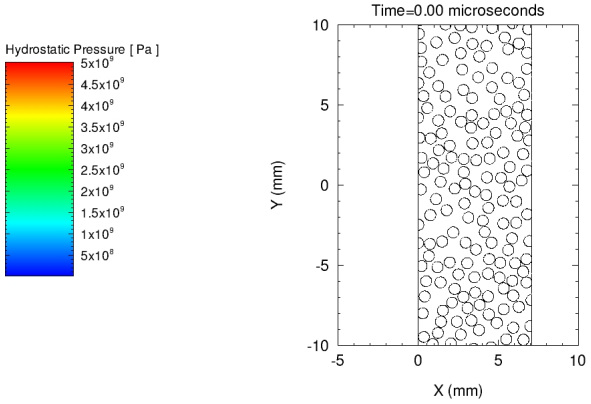

Figure 5.4: Initial 2D simulation geometry for 40% volume fraction 700 μm glass beads in a PMMA matrix.

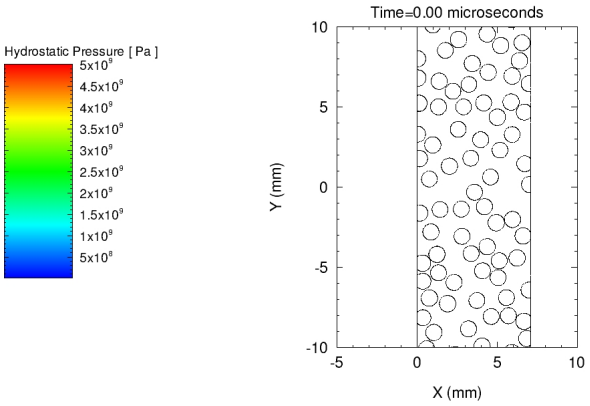

Figure 5.5: Initial 2D simulation geometry for 40% volume fraction 1000 μm glass beads in a PMMA matrix.

Spatial heterogeneity can be considered to increase, as the mean bead diameter increases away from the characteristic length scale given by the shock width in pure PMMA. In the case of a 1000 $^{m}/_{s}$ impact with a 6061 aluminum flyer plate, the shock width in pure PMMA was measured to be 22.96 ± 0.77 μm in Shot 25. This value assumes a steady shock speed of $3.826 \pm .128$ $^{mm}/_{\mu s}$ and an observed rise time of 6 ns. The average bead diameters chosen span a range of two orders of magnitude from the unaltered shock width, offering adequate room for experimentation.

Hydrostatic pressure contour plots were generated with CTH at 1 μs after flyer plate impact. The results for 100 μm, 500 μm, and 1000 μm diameter mean bead size at 40% glass by volume are shown below in Figures 5.6, 5.7, and 5.8.

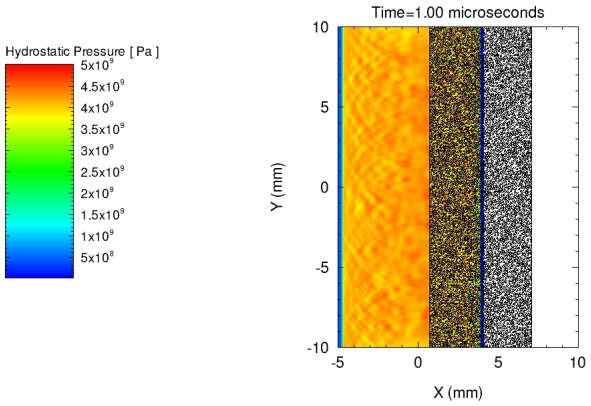

Figure 5.6: Hydrostatic pressure contours at 1 μs after impact for 40% volume fraction 100 μm glass beads in a PMMA matrix. Impactor is 6061-T6 aluminum with impact velocity of 1 $^{km}/_{s}$.

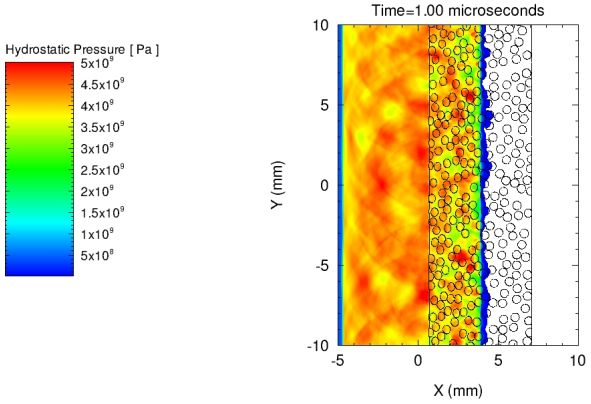

Figure 5.7: Hydrostatic pressure contours at 1 μs after impact for 40% volume fraction 500 μm glass beads in a PMMA matrix. Impactor is 6061-T6 aluminum with impact velocity of 1 $^{km}/_{s}$.

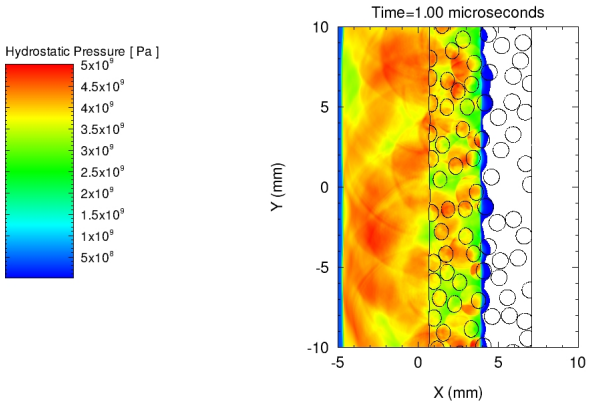

Figure 5.8: Hydrostatic pressure contours at 1 μs after impact for 40% volume fraction 1000 μm glass beads in a PMMA matrix. Impactor is 6061-T6 aluminum with impact velocity of 1 $^{km}/_{s}$.

It is clear in the above figures that the imposed shock wave has traversed approximately the same distance into each composite sample, with the primary difference then being the thickness and morphology of the shock front. At the smallest average bead diameter of 100 μm, the bead size is not significantly different from the shock thickness in pure PMMA. A roughly planar thin shock front is observed, even with a large number of interfaces present. Many reflections are noted in the shock loaded region of the PMMA and glass composite. At this scale, it is difficult to observe secondary reflections that redirect scattered energy back toward the shock front. After a short (less than 0.5 mm transit in the composite), the shock width stabilizes to be roughly equal to the average bead size.

As the mean bead size is increased to 500 μm in Figure 5.7, rippling and broadening of the shock front is noted. The shock front is rippled approximately evenly across its length, and the steady state shock width again approaches the mean bead diameter of the composite. There are sufficiently many beads and interfaces present to ensure that the shock does not encounter uninterrupted regions of PMMA. Pressure concentrations are observed due to constructive interference of stress waves in the PMMA binder. These large differences in stresses likely lead to large shear stress levels, especially near the interfaces. No immediate opening of voids is observed, but the simulations are not specifically intended to visualize or predict damage in these composites.

The 1000 μm glass bead composite simulation in Figure 5.8 again follows the same trend of widening the shock front to near the mean bead diameter. A shock front this wide greatly reduces particle accelerations and thus the forces seen by the material at the shock front. The limit to this behavior at a fixed glass volume fraction is that there are relatively fewer beads and interfaces present to serve as scattering sites. This manifests itself in non-optimal scattering, where significant areas of the disrupted shock front can straighten out. In Figure 5.8, consider the horizontal paths at y = 0.5 mm and y = 4 mm. At y = 0.5 mm, a very narrow shock front is approaching a glass bead at x = 4 mm. The wave has already passed through a bead at x = 1.5 mm, but the wave front through pure PMMA after the first bead allows for the front to straighten out. The multi-point velocity measurement capability discussed in Section 3.3.1 is ideal for quantifying the level of spatial heterogeneity upon shock breakout on the rear surface. It is expected that a large uncertainty in measured shock particle velocity rise times will be observed.

Rear surface morphology of the 2D simulations was also examined. The location of the rear surface was tracked at discrete times after shock break-out in order to quantify rippling and spatial disruption. Based on the above discussion, there should be a difference in ripple magnitude and period on the rear surface. The ripple period will not be constant due to the randomness inherent in the composite geometry. Figures 5.9, 5.10, and 5.11 illustrate the surface deformation over a 5 mm line centered on y = 0 mm.

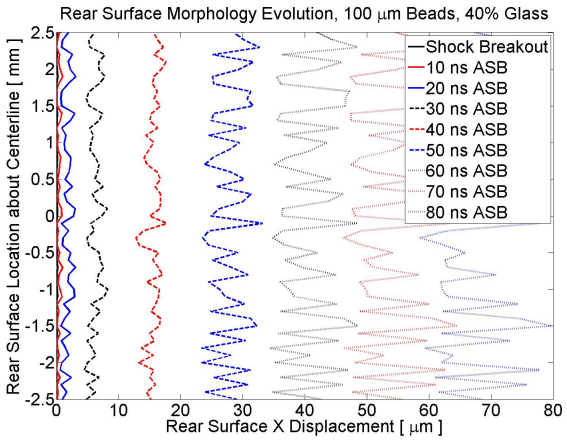

Figure 5.9: Rear surface morphology after shock breakout for 40% volume fraction 100 μm glass beads in a PMMA matrix.

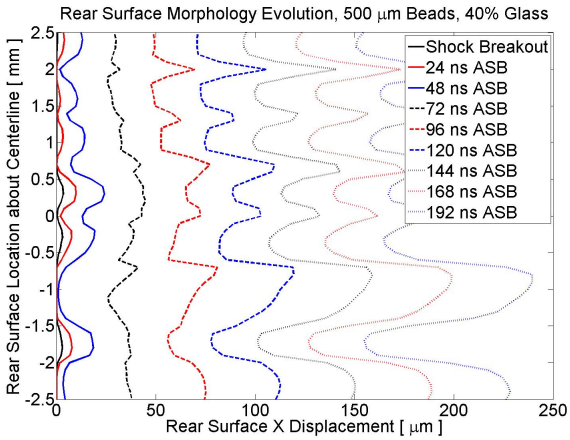

Figure 5.10: Rear surface morphology after shock breakout for 40% volume fraction 500 μm glass beads in a PMMA matrix.

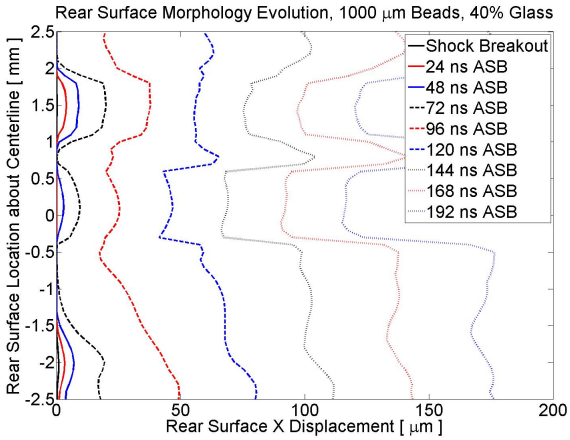

Figure 5.11: Rear surface morphology after shock breakout for 40% volume fraction 1000 μm glass beads in a PMMA matrix.

When the composites are made of of small beads, the magnitude of the surface ripples are small, and the pitch, or peak to peak distance, is small, as seen in Figure 5.9. This rippling is approximately 10 μm in amplitude with a pitch of approximately 200 μm. The fact that neither of these scales appears related to the mean bead diameter indicates that optimal scattering has not been achieved, and that the beads of diameter similar to the shock width in pure PMMA do not have a dramatic effect on shock thickness. The surface disruption reaches a steady state near the black dashed line, 30 ns after shock breakout (ASB). A definite change in rear surface morphology is observed with larger beads.

In the 500 μm bead diameter case shown in Figure 5.10, a steady rear surface profile develops

at approximately the black dotted line, 144 ASB. The ripple at this time is approximately 50-75 μm in amplitude. Pitch of the ripples is near the mean bead diameter at 500 μm. This shape is most likely due to the placement of the beads near the rear surface in the area of interest. Studies performed on different geometries of beads placed in regular grid arrangements (Face Centered and Hexagonal Close Packed grids) returned ripple pitches related to the vertical spacing of the rows of the beads, a quantity determined by the volume fraction of glass present, not the bead size. While surface morphology is a reasonable measure of spatial disruption, using it as a scale factor for shock modification is not advisable. At best, it gives a hint to the size of the uncertainty bounds that must be placed on the metric used to quantify shock front modification.

A dominant scale for disruption is not observed for 1000 μm bead size in Figure 5.11. Even at 40% glass by volume, the large bead diameter results in relatively large distances between neighboring beads. Since the shock may reduce its thickness through regions of pure PMMA, areas of rapid particle acceleration are interspersed throughout the rear surface. Shock waves in nonlinear solids such as PMMA become steeper as the wave propagates farther in the material. The bead dispersion can counteract the shock steepening, provided that there are enough scatterers present [37]. Shock disruption, as evidenced by the dips in rear surface displacement at y = 0 mm and y = 1.5 mm are due to scatterers located immediately near to the rear surface. It is possible that jetting of the more ductile PMMA could occur as well. The surface near the beads begins to accelerate sooner than the PMMA nearby due to the higher local shock speed in the glass, but then their higher density retards their forward motion. The lighter PMMA then accelerates past the regions with beads, forming the high ridges on the rear surface. The regular spacing of the jets encountered in simulations with smaller average bead diameters is likely due to the closer, more consistent spacing in-between the beads than it is due to their size.

The preliminary CTH study was successful in determining that there are multiple scattering effectiveness regimes across the range of available bead sizes. The bead sizes span one order of magnitude and the corresponding shock thickness can be 10 to 100 times the thickness of a shock in pure PMMA. These composites can also be realized through processing methods described in

Section 3.1.3.

5.1.2 Experimental Results

Planar plate impact experiments with monodisperse bead diameter distributions centered about the mean used in the simulated experiments were completed with beads sorted as described in 3.1. Rear surface wave profiles for 7.1 mm composite plates impacted at 1000 $^{m}/_{s}$ by aluminum flyer plates were measured using multi-channel PDV. In order to eliminate target plate thickness as a variable and ensure the validity of the shock jump analysis in 2.1.1, a series of shots was completed with composite target plates of varying thickness before proceeding with varying the particle size.

5.1.2.1 Structured Steady Waves

Three experiments were undertaken to confirm that the shock waves observed after passing through 7.1 mm of composite target plates were fully developed and steady when observed. 100 μm and 500 μm beads at 40% by volume were used in the fabrication of these target plates. Shots 9, 33, and 35 used 100 μm beads, and shots 11, 34, and 36 used 500 μm beads. All shots were completed with impact velocities of 1010 ± 5 $^{m}/_{s}$ except for shot 9 at 1078.4 ± 1.1 $^{m}/_{s}$. Glass beads on the smaller side of the spectrum were also chosen to minimize the risk of measuring geometry specific effects, such as the case of measuring rear surface particle velocity in a bead free region. Experimental steady wave profiles are shown in Figures 5.12 and 5.13. The plate thicknesses examined are 5 mm, 7.1 mm, and 10 mm. The choice of 100 μm and 500 μm beads enables the use of peculiar shock structures to verify the level of wave development. In Figure 5.12, there is a significant short duration particle velocity overshoot present above the late time response. The 7.1 mm target (Shot 9) shows a higher steady state particle velocity due to its higher impact velocity. The initial transient will be explored later with the reverse ballistic experiments in 5.1.2.3. The initial transient width and relative height in Figure 5.12 are similar. Transit time (impact time occurs at approximately -0.2 μs) is commensurate with target plate thickness.

The development of shock widths much greater than the shock width in pure PMMA warrants

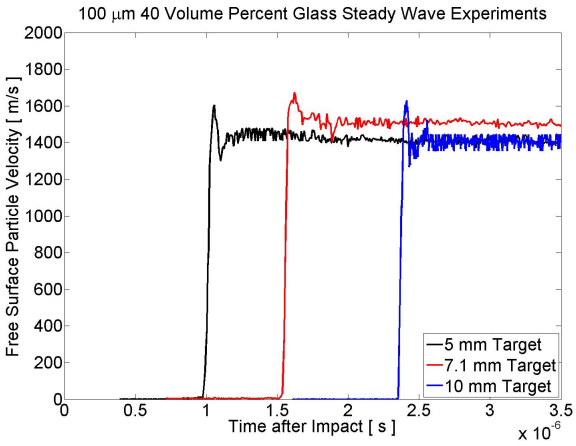

Figure 5.12: Steady wave profiles observed for 40% volume fraction 100 μm glass beads in a PMMA matrix.

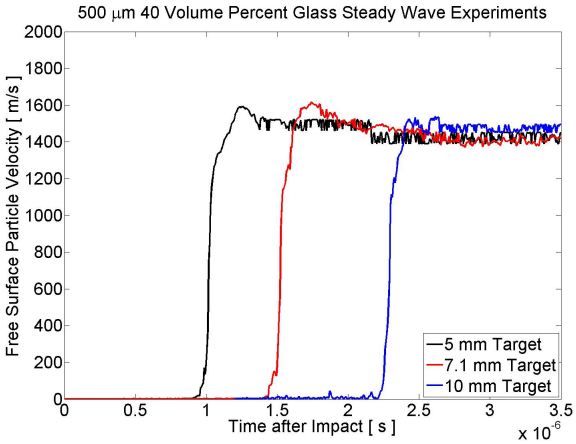

Figure 5.13: Steady wave profiles observed for 40% volume fraction 500 μm glass beads in a PMMA matrix.

the examination of development time to steady state at larger bead diameters as well. 500 μm diameter bead composites show similar shock profile development characteristics. The wave profile is nearly identical for each thickness case, and the wave speeds in each case match closely. Wave speeds are presented in Table 5.1. Shock speed for 100 μm, 7.1 mm thick, is omitted due to the higher impact velocity.

Target Thickness [mm]	Shock Speed 100 μm Beads [$^{mm}/_{\mu s}$]	Shock Speed 500 μm Beads [$^{mm}/_{\mu s}$]
5.0	4.089 ± 0.140	4.106 ± 0.119
7.1	–	$4.154 \pm .110$
10.0	$3.957 \pm .186$	$3.958 \pm .081$

Table 5.1: Shock speed as a function of thickness for 40% volume fraction 100 and 500 μm glass bead composite impacted at nominally 1 $^{km}/_{s}$.

In order to evaluate wave profile development distance, knowledge of the Hugoniot properties of the PMMA and composite material are required. 7.1 mm thick targets were fabricated, and impacted by aluminum flyer plates at velocities between 600 and 1400 $^{m}/_{s}$. Shock speeds were computed based on the difference of the average time of arrival as measured by tilt pin shorting times and the 10% particle velocity level that is also used to determine shock wave rise time. Table 5.2 and Table 5.3 summarize the experimentally observed state variables for as molded PMMA as well as a representative composite formulation.

Shot	Impact Velocity [$^{km}/_{s}$]	Particle Velocity [$^{km}/_{s}$]	Shock Velocity [$^{km}/_{s}$]
24	0.781	0.609 ± 0.004	3.591 ± 0.021
25	1.011	0.773 ± 0.003	3.826 ± 0.129
26	1.211	0.920 ± 0.006	4.003 ± 0.084

Table 5.2: Experimental conditions for PMMA Hugoniot parameter extraction

Shot	Impact Velocity [$^{km}/_{s}$]	Particle Velocity [$^{km}/_{s}$]	Shock Velocity [$^{km}/_{s}$]
51	0.580	0.431 ± 0.013	3.796 ± 0.151
54	0.787	0.555 ± 0.006	3.986 ± 0.167
11	1.078	0.702 ± 0.006	4.139 ± 0.110
52	1.379	1.047 ± 0.008	4.255 ± 0.068

Table 5.3: Experimental conditions for Composite Hugoniot parameter extraction

It also critical to ensure that the shock structure has fully developed by the time it reaches the rear surface so that the scaling determined by the rise times is meaningful. Bland [21] determined

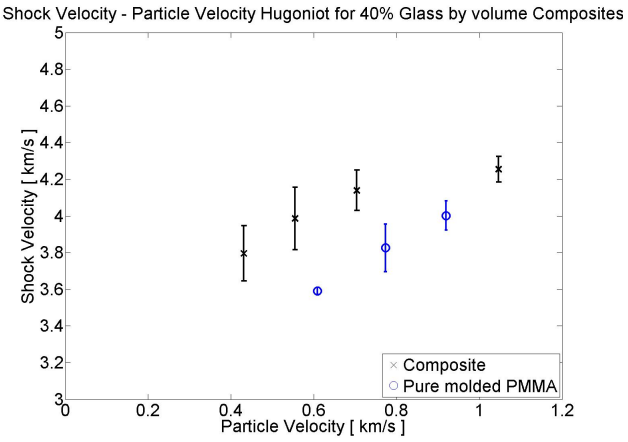

Figure 5.14: Shock speed vs. particle velocity Hugoniot curves for 40% volume fraction 500 μm glass beads in a PMMA matrix (Black X) and pure PMMA (Blue O).

that an approximate required propagation distance for attaining steady state, δ, can be written as:

$$\delta = \frac{3}{8}\frac{C_0}{s}\frac{1}{\dot{\epsilon}} \tag{5.1}$$

C_0 and s are the parameters of the linear Hugoniot shock speed vs. particle velocity relationship. Strain rate, $\dot{\epsilon}$, is approximately equal to the jump in strain divided by the wave rise time, τ, both of which are readily available. Substituting

$$\dot{\epsilon} = \frac{u_p}{U_s \tau} \tag{5.2}$$

in to the relationship for δ:

$$\delta = \frac{3}{8}\frac{C_0}{s}\frac{U_s \tau}{u_p} \tag{5.3}$$

Referencing Figure 5.14, the linear approximation to the 500 μm bead Hugoniot at 40% glass by volume is given as:

$$U_s = 3.566 + 0.698 u_p \tag{5.4}$$

The characteristic distance, δ, is then:

$$\delta = \frac{3}{8}\frac{3.566\ {}^{mm}/_{\mu s}}{0.698}\frac{4.1\ {}^{mm}/_{\mu s} 0.146\ \mu s}{0.7\ {}^{mm}/_{\mu s}} = 1.64\ mm \tag{5.5}$$

Assuming that Hugoniot response is independent of particle size [59] [64], and varying the rise times shows that the distance for developing steady shocks in all composites remains under 2.5 mm. Due to scattering being a stronger contributor than the material viscosity used to derive Equation 5.1, development distance is likely even shorter — on the order of one to two bead diameters.

Within experimental error, the shock speeds appear to be steady, and structure fully developed. Constant shock speed, combined with a qualitative structure analysis indicate that the steady wave assumption made in the theoretical analysis holds in the case of these particulate composites. The determination of the effects of particle size on shock structure may now proceed.

5.1.2.2 Shock Structure as a Function of Particle Size

Five average bead diameters have been chosen, each with tight bounds on the distribution of bead diameters present around the average. The bead diameters were chosen to be identical to those used in the initial simulation study, and enforced with the use of stainless steel screens. The average diameters and their bounds are given in Table 5.4. A uniform distribution about the mean is assumed. Due to the tightness of the bounds, the beads used in each composite can be considered to be monodisperse. A series of ten experiments was proposed consisting of five mean bead sizes and two bead volume fractions. Due to the spatial heterogeneity, three points on the rear free surface of each target were illuminated with collimating PDV probes. A particle velocity time history for each rear surface point was recorded. These time history records for 40% glass beads by volume are presented below, with the remaining five 30% glass bead by volume time histories being presented in Appendix B.

Figures 5.15, 5.16, 5.17, 5.18, and 5.19 show rear surface particle velocity, with time t = -0.2 μs corresponding to time of initial impact on the composite target by the aluminum flyer. The probes are located on the circumference of a 5 mm diameter circle, coincident with center of the target disk.

Label	Mean Bead Size [μm]	Spread [μm]
100	110	$\pm$ 6
300	294	$\pm$ 13
500	522	$\pm$ 19
700	693	$\pm$ 12
1000	1006	$\pm$ 25

Table 5.4: Glass sphere sizing used in composite fabrication.

Probes are located at 12:00, 4:00, and 8:00 positions on the circle. This placement ensures that the observation is not influenced by edge unloading waves until after the initial wave pulse reaches the rear surface. A 3 μs record window is adequate for the purposes of this experiment.

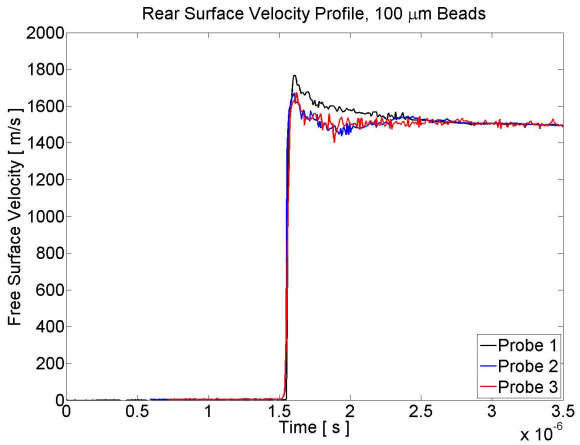

Figure 5.15: Particle velocity vs. time history for 40% volume fraction 100 μm glass beads in a PMMA matrix. Impactor is 6061-T6 aluminum with impact velocity 1078 $^m/_s$.

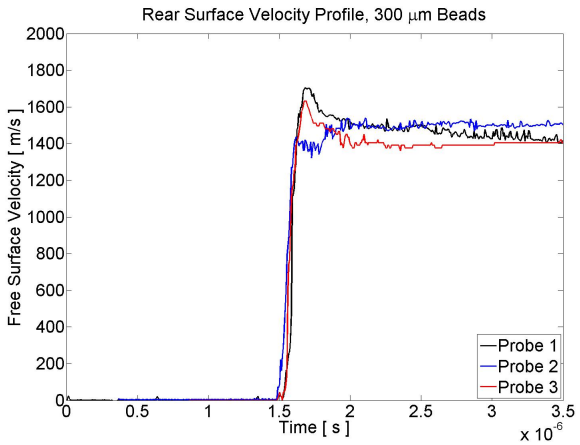

Figure 5.16: Particle velocity vs. time history for 40% volume fraction 300 μm glass beads in a PMMA matrix. Impactor is 6061-T6 aluminum with impact velocity 1025 $^m/_s$.

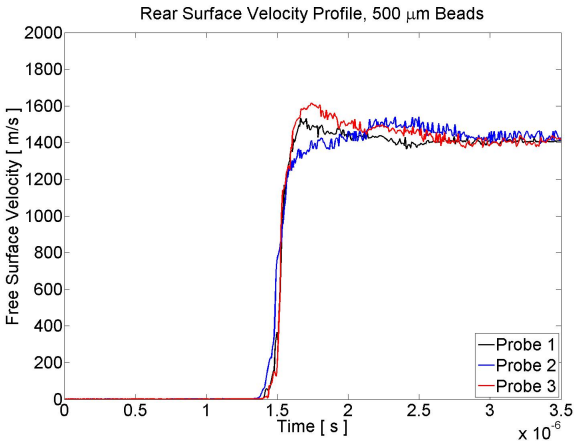

Figure 5.17: Particle velocity vs. time history for 40% volume fraction 500 μm glass beads in a PMMA matrix. Impactor is 6061-T6 aluminum with impact velocity 1017 $^{m}/_{s}$.

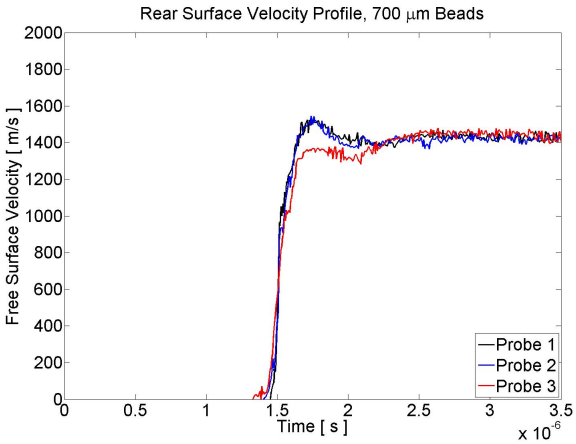

Figure 5.18: Particle velocity vs. time history for 40% volume fraction 700 μm glass beads in a PMMA matrix. Impactor is 6061-T6 aluminum with impact velocity 1010 $^{m}/_{s}$.

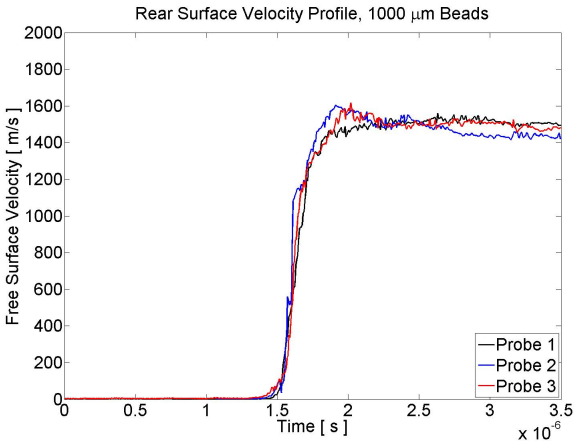

Figure 5.19: Particle velocity vs. time history for 40% volume fraction 1000 μm glass beads in a PMMA matrix. Impactor is 6061-T6 aluminum with impact velocity 1012 $^{m}/_{s}$.

Several qualitative observations may be made from these wave traces. At the smallest bead sizes, the slope of the lead waveform is very large, indicating a very narrow shock thickness and a high strain rate. There is also a significant short duration overshoot above the steady state particle velocity. As the mean bead size increases, the slope of the lead wave pulse is reduced, and structure begins to develop at the leading edge and near the point of maximum particle velocity. This rounding is a significant part of the measured shock width, as the slope, while reduced, remains relatively steep.

In addition to the reduction in slope, the wave profile changes shape from a large short duration overshoot (Figures 5.15 and 5.16), to a lower magnitude longer duration overshoot (Figures 5.17 and 5.18), to a final fully rounded shape (Figure 5.19). In smaller bead diameter composites, the high interface count results in a large amount of primary reflections directing energy in the direction opposite of shock propagation. These primary reflected waves have a high likelihood of encountering another PMMA/glass interface, resulting in a secondary reflection directing energy back toward the shock front. As waves in compressed media travel faster than those propagating into a quiescent material, they may catch up with the lead shock pulse, contributing to the amplitude and short duration of the overshoot. As the bead diameter is increased, the constant volume fraction constraint enforces that there are fewer beads present, and thus fewer interfaces to redirect energy. The beads still serve as effective scatterers, thickening the shock front to near their average diameter, but the

magnitude of the overshoot is lessened, and the duration increased.

In order to verify that the overshoot observed is solely a product of the addition of scatterers into the PMMA matrix material, shots 24 through 26 were completed. Three pure PMMA targets were fabricated from the same powdered PMMA source without the addition of glass beads, and subjected to plate impact by 6061 aluminum flyer plates. Experiments were conducted at 800 $^{m}/_{s}$, 1000 $^{m}/_{s}$, and 1200 $^{m}/_{s}$ on 7 mm thick molded targets. Wave profiles are presented in Figure 5.20.

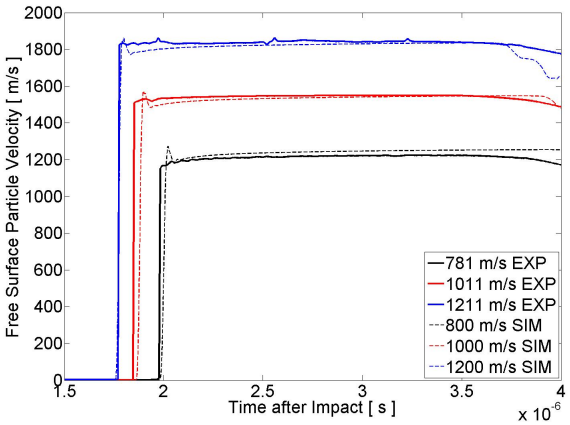

Figure 5.20: Shock wave profile for pure molded PMMA impacted by 6061-T6 aluminum at 781 $^{m}/_{s}$, 1011 $^{m}/_{s}$, and 1211 $^{m}/_{s}$.

Both CTH simulation results and experimental wave profiles are shown in Figure 5.20. Experimental results do not exhibit any overshoot behavior, and the shock thickness remains near 20 μm. The slight bumps in the top part of the shock in the simulation results are an artifact of tracer position in regards to their placement on the rear surface and how CTH handles unloading across material cells. Once the boundary conditions are established, the particle velocity drops immediately back to the steady state velocity that is experimentally observed.

A quantitative metric is needed to evaluate the magnitude of shock disruption as a function of mean bead size in the composites of interest. In the field of control, models and controllers are evaluated in their response to step inputs by defining a rise time. In this study, a rise time is computed by measuring the time that it takes for the rear surface particle velocity to accelerate from 10% of its maximum value to 90% of its maximum value. The shock profile within the 10-90% range contains information from both the change in the slope of the velocity time history, as well as the

overshoot behavior. In order to take into account the spatial heterogeneity, a rise time is computed for each probe pointed at the rear surface. An average is taken of the three spatially separated rise times, and a standard deviation reported to give vertical error bounds. As the bead diameter is assumed to be uniform in-between the bounds defined by the mesh screens, the horizontal error bars are set to these bounds. The experimentally observed rise times for 30% and 40% glass beads by volume are superimposed upon simulation derived rise times in Figures 5.21 and 5.22.

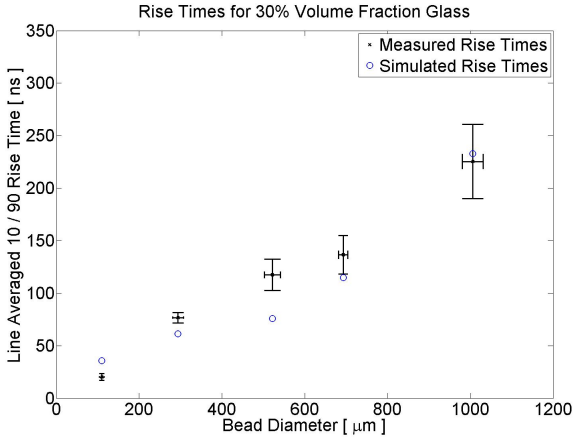

Figure 5.21: 10%-90% shock wave rise time as a function of mean particle diameter for 30% glass by volume composites.

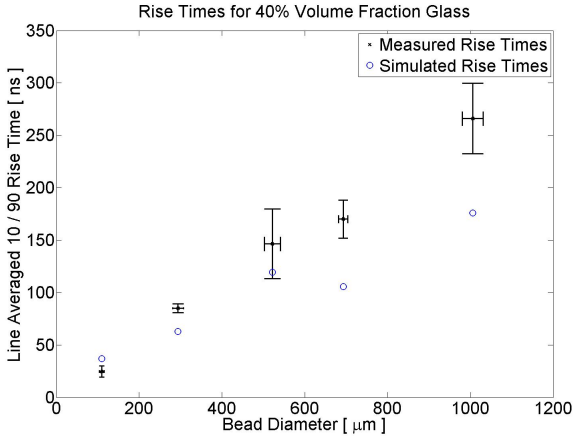

Figure 5.22: 10%-90% shock wave rise time as a function of mean particle diameter for 40% glass by volumes composites.

The observed rise times scale linearly with increasing particle diameter for composites with monodisperse mead size distributions. The shock width is increased by nearly one order of mag-

nitude in both time and space between the smallest and largest particulates. Optimal scattering results in a shock width nearly as thick as the diameter of the beads present. At low levels of heterogeneity (i.e., lower volume fractions and smaller bead diameters), the CTH model parameters can reasonably capture the shock behavior observed in experiments. Interface integrity and local damage is not significant enough for the observed rise times to depart from the simulation results. Each composite sample is subjected to nearly 4 GPa average compressive loading for nearly 6 μs. As the interface count increases with volume fraction and particle size, the number of reflections and stress concentrations result in local damage. Interface separation and local tension resulting in the opening of voids introduces additional heterogeneity, further increasing the experimentally observed rise time.

The CTH simulation parameters are not intended to replicate the effects of interface separation and void growth. As the interfaces are assumed to stay welded, the simulations underestimate the level of heterogeneity and scattering efficiency, and therefore underestimate the observed rise time. The additional damage also inhibits the passage of secondary reflections catching up with the lead shock wave. Overshoot is not observed in the largest bead diameters in the 40% glass by volume composites.

The linear scaling with bead size is consistent across the entire glass volume fraction range under examination. Smaller beads approach the unmodified shock thickness in the matrix material as seen in the previous work on alumina/tungsten carbide epoxy composite systems. The linear regime will also break down at larger bead sizes due to the rapid decrease in number of interfaces per volume as the number of beads becomes fewer. In this regime, there will be regions of significant shock disruption immediately next to regions of strong sharp shock. The increasing magnitude of the error bounds on shock rise time with larger beads begins to indicate the departure from the linear shock rise time scaling regime. The high level of spatial heterogeneity at the largest bead sizes also suggests that the assumption of a steady shock wave is beginning to break down. As the spacing in-between particulates increases, the shock does not remain disrupted and its passage through homogeneous regions of matrix material results in steepening of the shock front, as demonstrated in Figure 5.8.

When the bounds on particle size are limited to the size range containing high strength concretes and polymer bonded high explosives, the linear scaling argument can be considered valid. A two parameter model is proposed after determining the slope defined by the individual data points. The slope from the origin for each experiment is given in Tables 5.5 and 5.6.

Mean Bead Size [μm]	Shock Rise Time [ns]	Slope [$^{mm}/_{\mu s}$]
110	20.19	5.45
294	76.76	3.83
522	117.51	4.44
693	136.60	5.07
1006	225.37	4.46

Table 5.5: Proportionality constant for shock rise times, 30% glass by volume composites.

Mean Bead Size [μm]	Shock Rise Time [ns]	Slope [$^{mm}/_{\mu s}$]
110	24.60	4.47
294	85.03	3.46
522	146.44	3.56
693	170.10	4.07
1006	265.99	3.78

Table 5.6: Proportionality constant for shock rise times, 40% glass by volume composites.

The average slope for 30% glass by volume is 4.65 $^{mm}/_{\mu s}$, while the average slope for 40% glass by volume is 3.87 $^{mm}/_{\mu s}$. These values compare favorably with the measured average shock speed in the composite targets. The measured shock speed is considered to be a constant over bead size. The shock speed contains in it information about the impedance mismatch as well as material properties. When examined with the linear relationship between the shock rise time and mean particle diameter above, it becomes the perfect scale factor. A simple dimensional analysis suggests a scale factor with units of inverse velocity, as shown below for the rise time in terms of the bead diameter (d_{bead}) and shock wave speed in the composite (U_s):

$$\tau_{rise} = \frac{d_{bead}}{U_s} \tag{5.6}$$

The average measured shock speed for each volume fraction of glass are inverted to give a slope, passing through the origin and plotted over the experimentally observed rise times in Figures 5.23

and 5.24.

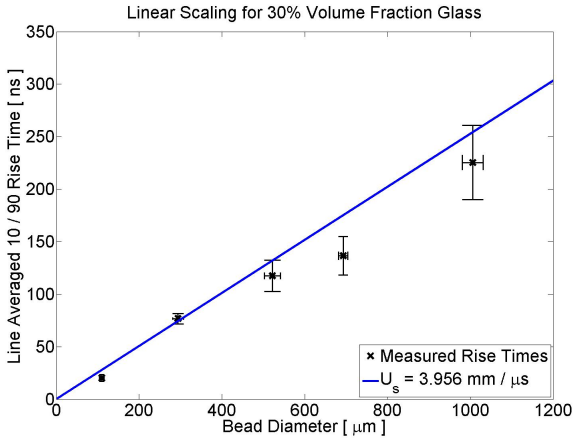

Figure 5.23: Rise time scaling for 30% glass by volume composites. Average Lagrangian shock speed of $U_s = 3.956\ ^{km}/_{s}$ is shown as the slope.

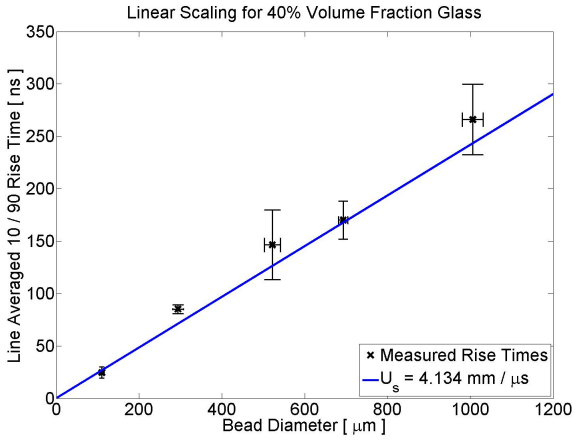

Figure 5.24: Rise time scaling for 40% glass by volume composites. Average Lagrangian shock speed of $U_s = 4.134\ ^{km}/_{s}$ is shown as the slope.

Shock rise time scales linearly with particle size divided by the bulk shock speed in the material. This scaling is even more clear when the physical shock thickness is considered. When the rise time is multiplied by the shock speed (assuming a steady wave), the length scale that is computed is nearly equal to the mean bead diameter present in the composite. Therefore, measuring the bulk shock speed and knowing something about the dominant composite length scale will give an estimate of the level of shock front disruption due to scattering by randomly dispersed composites.

A real test of this proposed scaling is then reevaluating data reported in previous work. The

work chosen to compare must also be in the overdriven shock regime, with a roughly monodisperse bead diameter distribution. The scaling in Equation 5.6 can then be used since the shock speed should contain the Hugoniot state information, shock impedance mismatch, and material properties. Experiments performed in the left hand range of Figure 2.14 are ideal candidates, since the absolute spread in bead diameter is small enough to be considered monodisperse, and there are experiments covering a large range in impedance mismatch. It is imperative that the beads present be large enough to be effective scatterers, or else the rise time of the pure matrix material will be the dominant time scale. In this case, the experiments performed by Vogler in 2010 [60] use particles in a mean diameter range too far away from the diameter range in this study.

Two of the tungsten carbide particle filled epoxy composite experiments that may be used to probe the limits of the scaling argument are those labeled WCE 5 and WCE 13 [60]. In the case of the WCE 5, the experiment with the highest impact speed at 1400 $^{m}/_{s}$, the reported shock speed was $U_s = 3.18\ ^{mm}/_{\mu s}$ for a composite with a mean particle diameter of 26 μm. The estimated rise time is then computed to be:

$$\tau_{rise} = \frac{26\ \mu m}{3.18\ ^{\mu m}/_{ns}} = 8.2\ ns \tag{5.7}$$

The observed rise time is approximately 10^{+5}_{-0} ns. At these extremely small bead sizes, the scaling law begins to break down and underestimate actual rise time. Extrapolation using the linear scaling is not advised. A further departure from the scaling observed in the present study occurs at low impact velocities. A 450 $^{m}/_{s}$ impact was employed in Experiment WCE 13, where the rise time was observed to be 50^{+10}_{-0} ns, much greater than the predicted rise time of 12.8 ns. It was observed that stress waves of lower magnitude were not steady, and attenuated rapidly with propagation into the composite sample, as shown in Figure 5.25. Experiments WCE 18, 19, and 7 were completed with different sample thicknesses at three impact velocities to study the evolution of the shock in the composite material. WCE 7 and WCE 13 were impacted at the same speed. It is possible that this impact speed is very near to the transition to a steady strong shock wave. Lower impact velocities demonstrate exaggerated rise times and do not reach a steady state particle velocity. It was reported that the cause of this attenuation is unknown [60]. No pure matrix material shock

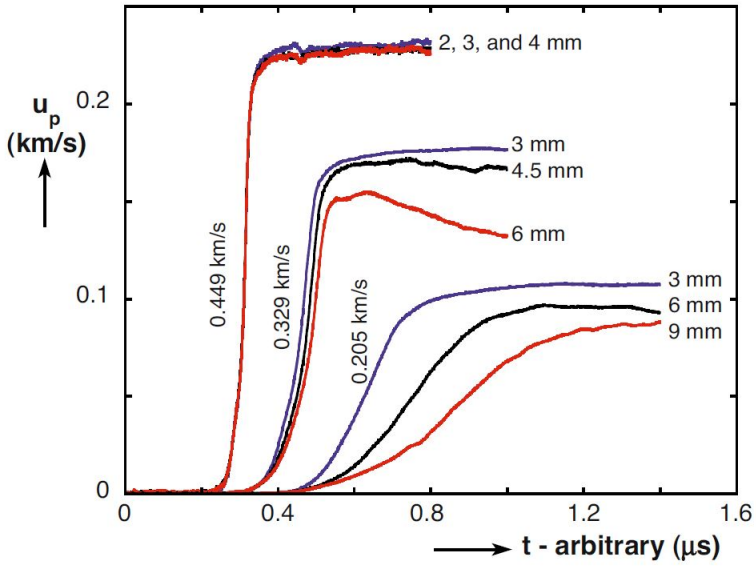

Figure 5.25: Non-steady waves observed in weak shock regime for WCE Composites. Adapted from [60].

studies were reported, but it is likely that the response in this case is strongly matrix material dependent. Therefore, it is important to verify that the propagating disturbance is steady and in the strong shock regime for the linear scaling relationship to be valid.

A data set within the interpolation range for the linear scaling was located in the thesis work of Neel and published in [52]. Three experiments were examined that were determined to be in the strong shock regime, and are presented in Table 5.7 below. The mean particulate size reported was 109 μm, with 90% of the particulates present within 55 μm - 178 μm. Composites were fabricated with alumina particles suspended in THV, a terpolymer of tetraflouroethylene, hexafluoropropylene, and vinyldiene fluoride.

Shot	Impact Velocity [$^{m}/_{s}$]	U_s [$^{mm}/_{\mu s}$]	Measured Rise Time [ns]	Predicted Rise Time [ns]
802	635	3.031	35.0	36.0
759	806	3.393	28.5	32.1
803	1009	3.813	20.0	28.6

Table 5.7: Overview of alumina-THV composite experiments courtesy of Dr. C. Neel

Wave profiles of the shots in Table 5.7 are presented in Figure 5.26.

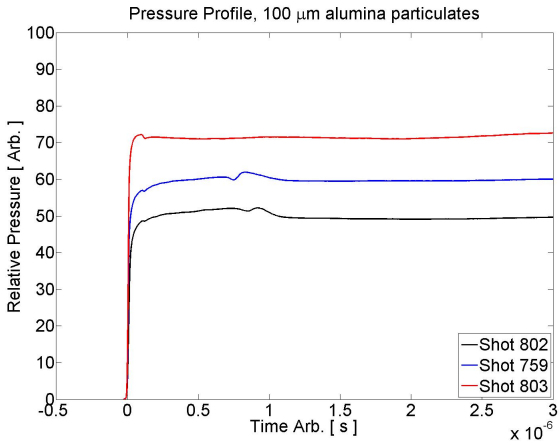

Figure 5.26: Pressure wave profiles in alumina-THV composites courtesy of Dr. Neel.

The wave profiles show the effects of significant scattering and a fully developed rounded structure. The rise times observed in the alumina-THV composite experiments completed by Neel in 2011 are reasonably predicted by the linear scaling observed in the glass bead PMMA composite system. It is interesting to note that the scaling also holds over a range of shock pressure levels. It is possible that the overestimation of the predictions is due to the larger spread in alumina particulate sizes. While the average diameter is the same as reported in the glass-PMMA composites, the particle morphology differs. The sphericity of the particulates in Neel's work is much lower, and the particulates appear to be relatively long, flat platelets with jagged edges. It is possible that this departure from perfectly spherical particulates is the cause of the discrepancy between the predicted and observed rise times. If the reported size is defined by the major axis, it may be reasonable to suggest a correction factor for the mean diameter input into the model to account for the existence of a fundamentally shorter length scale in the composite geometry.

It is also interesting to note that a short duration overshoot in pressure is observed in the case of the strongest shock in Figure 5.26. Pressure profiles were observed with PVDF stress gauges, which spatially average the pressure across the area. It is possible that a more robust method of measuring particle velocity (via velocity interferometry) would result in the visualization of a more significant offshoot and shorter rise time. An examination of the degree of energy redirection due to interface reflections is undertaken in the next section.

5.1.2.3 Reverse Ballistics Examination of Particle Velocity Overshoot

The change in shock structure across the range of bead diameters warrants further investigation. The larger particle velocity overshoot above the steady state particle velocity is significant, in that it seems to imply that secondary reflections may catch back up with the shock front. Along those lines, the composite material itself should not be damaged to a degree high enough to preclude transmission of secondary reflections. A series of reverse ballistic simulations were undertaken to examine the possibility of secondary reflection.

A reverse ballistics experiment is similar to a standard plate impact experiment, where the material of interest is the flyer plate, and the target serves only as a witness plate to generate a high pressure condition in the flyer and provide a surface on which to make a measurement. A schematic of a reverse ballistic experiment is presented below in Figure 5.27. The representative

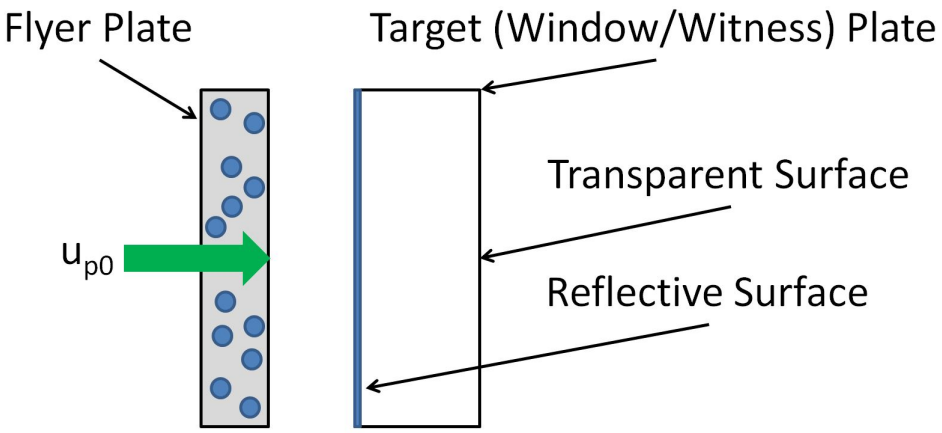

Figure 5.27: Schematic of a reverse ballistic impact experiment.

reverse ballistic experiment above is optimized for use in a powder gun, where the composite sample would be launched down the gun barrel into the window on the right. The window allows for interferometer monitoring of the impact face, denoted by "Reflective Surface". A window is made of a material transparent to the wavelength of the interferometer beams at pressures from ambient to the maximum encountered in the experiment, and thick enough to keep the target under compression throughout the duration of the experiment. Monitoring the impact face allows for the observation of the magnitude of primary reflection stress waves.

The simulations in this study are similarly arranged. A randomly generated composite geometry is situated uprange and coincident with a PMMA window and given an initial velocity sufficient to drive pressures equivalent to those seen in the standard forward ballistics experiments previously completed. A series of tracers located 0.1 mm from the interface were then used to extract the velocity history and monitor reflections. A simulation geometry schematic for 500 μm glass beads in a PMMA matrix is presented in Figure 5.28. In the following simulations, the initial velocity of the

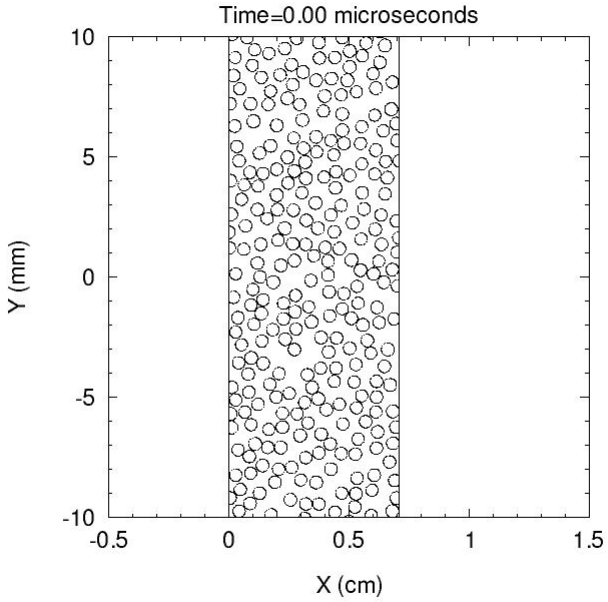

Figure 5.28: Schematic of a reverse ballistic impact simulation geometry.

composite section from X = 0 to X = 0.7 cm is 1400 $^{m}/_{s}$, striking a pure PMMA window occupying the space from X = 0.7 to X = 1.7 cm. Pressure maps clearly illustrate the scattering behavior as seen before in Figures 5.6 - 5.8. A series of pressure maps at 0.6 μs to 1.0 μs after impact are presented in Figures 5.29 - 5.33.

In order for secondary reflections to pile-up at the shock front, sufficient primary reflection activity should be seen and possess sufficient re-compression wave velocity to catch up with the lead shock front. Consider the compressive primary reflection wave fronts near +2.0 mm and −2.0 mm in Figures 5.29 - 5.33 moving in the positive X direction. These wave fronts coalesce and catch up

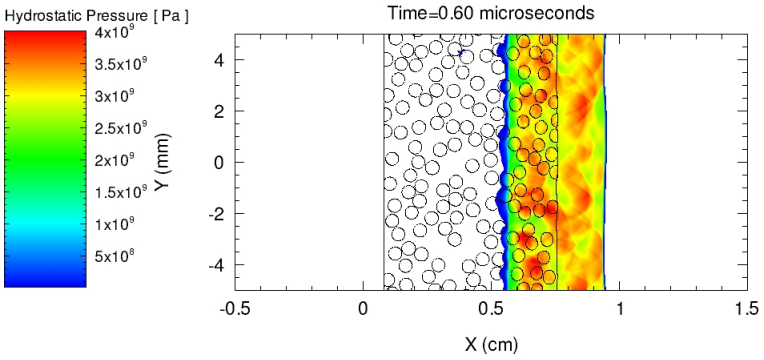

Figure 5.29: Reverse ballistic simulation pressure contours at 0.6 μs after impact into a PMMA window at 1400 $^m/_s$.

with the shock front propagating in to the window/witness plate material.

The wave fronts are 1 - 2 GPa above the symmetric plate impact pressure observed between two PMMA plates (green contours in the reverse ballistic pressure contour plots). Assuming that the impedance mismatch remains near the value at ambient pressure Equation 2.32 suggests that almost 40% of the primary reflected energy is turned around back toward the shock front, propagating into the undisturbed composite as secondary reflections. At higher interface densities (in the cases of smaller beads when volume fraction of glass is held constant) there are more reflection sites, and as such, overshoot magnitude increases with smaller bead size.

The frequency of reflections is clearly visible when particle velocity time histories at the interface between the composite and witness plate are examined. Two reverse ballistics simulations are presented in Figures 5.34 and 5.35 for 500 μm beads and for 1000 μm beads at 40% glass by volume. Impact speeds were identical between the two cases at 1400 $^m/_s$ in order to develop similar pressures as were generated by a 1000 $^m/_s$ impact with 6061-T6 aluminum alloy.

Large stress oscillations are clearly visible in the 500 μm reverse ballistics simulation. Each oscillation is a discrete reflection event, and the oscillations persist until release waves from the

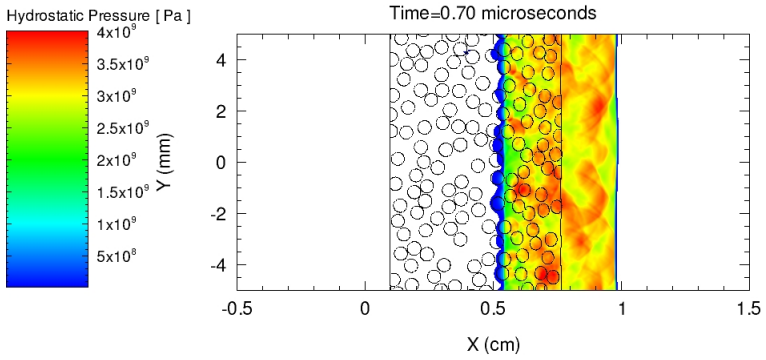

Figure 5.30: Reverse ballistic simulation pressure contours at 0.7 μs after impact into a PMMA window at 1400 $^{m}/_{s}$.

outside diameter edge reach the target centerline. An oscillatory stress time history is not observed in the 1000 μm simulation. Therefore, it is clear that particle velocity overshoot in composites with small beads is due to secondary reflections and reflected wave interference. Higher interface densities drive higher levels of overshoot. In periodic composites, a higher interface density also drove the rise time/overshoot response and oscillation magnitude. Steeper shock fronts and larger oscillation amplitudes were observed [64].

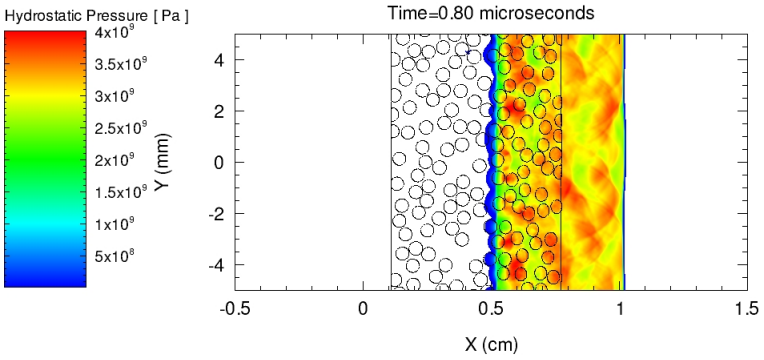

Figure 5.31: Reverse ballistic simulation pressure contours at 0.8 μs after impact into a PMMA window at 1400 $^{m}/_{s}$.

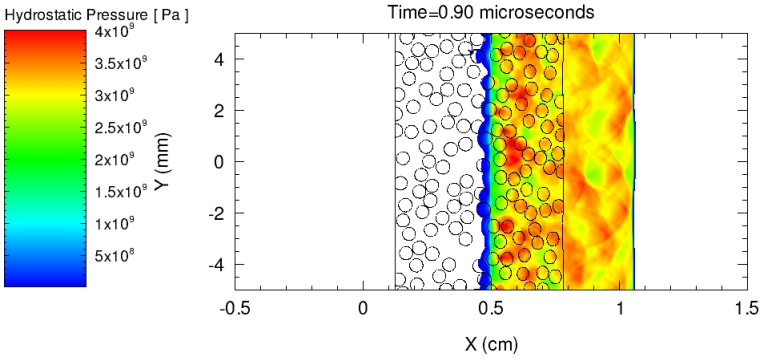

Figure 5.32: Reverse ballistic simulation pressure contours at 0.9 μs after impact into a PMMA window at 1400 $^{m}/_{s}$.

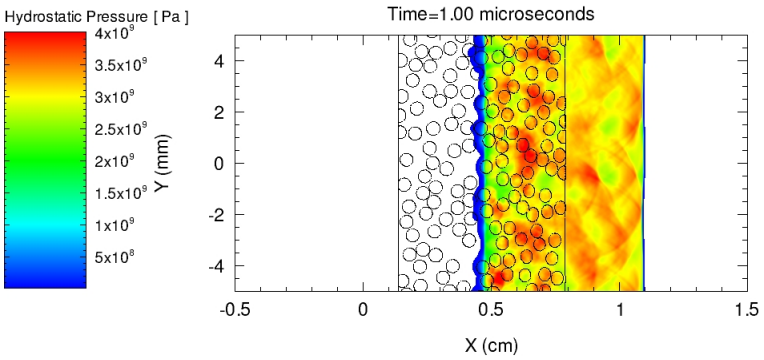

Figure 5.33: Reverse ballistic simulation pressure contours at 1.0 μs after impact into a PMMA window at 1400 $^{m}/_{s}$.

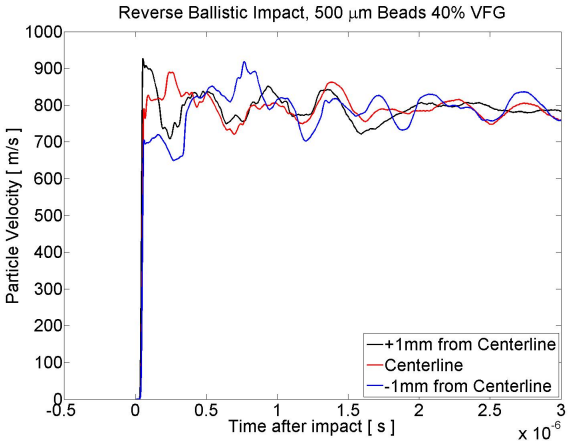

Figure 5.34: Interface time histories for 40% volume fraction 500 μm glass beads in a PMMA matrix reverse ballistics simulation. Impact is against a PMMA window at 1400 $^{m}/_{s}$.

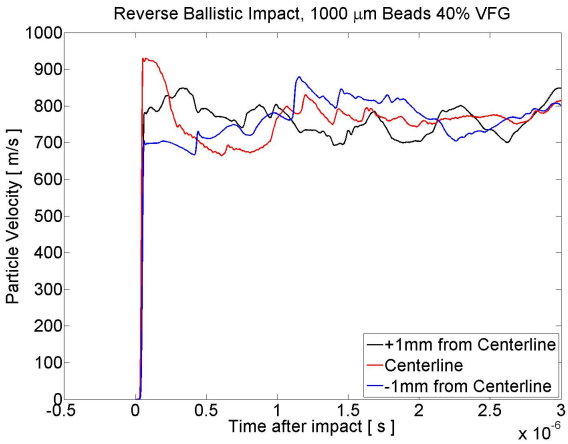

Figure 5.35: Interface time histories for 40% volume fraction 1000 μm glass beads in a PMMA matrix reverse ballistics simulation. Impact is against a PMMA window at 1400 $^{m}/_{s}$.

5.2 Bi-Modal Bead Size Distributions

A series of experiments were conducted and simulated to determine the level of shock front modification at volume fractions of 40% glass by volume. It was necessary to depart from a single mode monodisperse bead size distribution in order to prevent composite degradation due to thermal expansion mismatch and residual stresses causing cracking to achieve higher volume fractions. The two step heat treating process described in Section 3.1.4 reduces the likelihood of failure, but it was necessary to remake several of the composites since they could not be completely stress relieved, and would slowly delaminate from the outside diameter inwards.

An experiment matrix is designed using the 30% glass by volume single mode and 40% glass by volume single mode bead diameter observations as a basis of comparison. Each bi-mode composite consists of a base bead mix at 30% by volume, with smaller diameter interstitial beads added in increments of 10% glass by volume. Rise times are compared for 40% glass by volume single mode and bi-mode composites, as well as for simulation results.

5.2.1 Experiment Matrix

Three base bead mixes were chosen for this study: 500 μm, 700 μm, and 1000 μm at 30% by volume. To these base mixes were added 100 μm, 300 μm, 500 μm, and 700 μm diameter interstitial beads. Table 5.8 summarizes the experiments completed in this study.

Base Beads [μm]	Interstitial Beads [μm]	0% Interstitial	10 %	20%
500	100	X	X	X
500	300	X	X	X
700	300	X	X	X
1000	300	X	X	X
1000	500	X	X	X
1000	700	X	X	-

Table 5.8: Bi-Mode bead diameter distribution composites used in present study.

X's denote completed experiments. 1000 μm base with 700 μm interstitial beads at 20% by volume was omitted due to the large bead sizes and high volume fraction causing significant cracking and separation of the matrix material from the beads during cooling. Preliminary simulation results

indicated that the addition of smaller beads than the base mix as interstitials reduced shock wave rise time by an appreciable amount. This trend persisted in composites with a large diameter difference between base and interstitial. The trend was not nearly as strong when base and interstitial beads were similar in size. Increasing composite heterogeneity resulting in decreasing shock thickness was an unexpected outcome. An experimental study was undertaken to clarify the actual material behavior of bi-mode composites.

5.2.2 Experimental Results

Simulation geometries were generated as 30% by volume composites, and then smaller interstitial beads were added to the geometries to bring the total volume fraction of inclusions to the correct level. A gauge of heterogeneity in the geometry and rise time is given by generating three idealizations of bead distributions for each experimental case. A representative rise time is taken from each of the three idealizations, and then a standard deviation for each case is computed. These rise times are then plotted with a single mode, 30% glass by volume simulated rise time as a basis of comparison to determine a trend for rise times as the space between the largest beads is replaced with smaller glass beads instead of PMMA binder. Descriptions of geometry generation processes and material parameters are available in Section 4.

For reference, a horizontal line has been added to each plot showing the rise time associated with a single mode rise time for 40% glass by volume of the base bead size. This will allow for the determination of whether or not a bi-modal distribution is a more effective shock front disrupter than a simple single mode bead diameter distribution composite. Further, it shows how much more effective increasing the glass volume fraction is at shock front disruption. Each simulation result is paired side by side with a corresponding experimental result. Reported experimental rise times and uncertainties are based on three particle velocity traces on the rear surface of a single target. This ensures that the rise time uncertainty is due solely to spatial heterogeneity effects, as opposed to subtle changes in impact velocities. All measured impact velocities were between 1000 $^{m}/_{s}$ and 1010 $^{m}/_{s}$.

The first bi-mode composite examined consists of a 500 μm base at 30% by volume, with addition of 100 μm interstitial beads. Rise times for the simulation and experiments are shown in Figure 5.36.

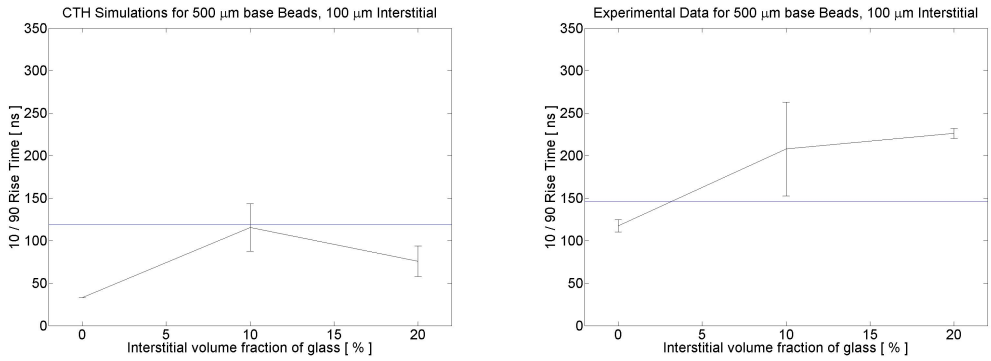

(a) Simulation results

(b) Experimental results

Figure 5.36: Simulation and experimentally observed shock rise times for 30% volume fraction 500 μm glass beads base with 100 μm interstitial glass beads in a PMMA matrix. Impactor is 6061-T6 aluminum.

The simulation results in Figure 5.36a show that as the volume fraction of smaller particulates is increased, rise times at first increase, and then decrease. The experimental observations disagree, showing a consistent increase in rise time with the addition of smaller particulates up to a total of 50% glass by volume. The use of smaller interstitial particles resists the tendency of the shock front to steepen as it otherwise would when passing through the large regions in between the base beads.

As the size difference between the base beads and the interstitials decreases, the experimental and simulation results better correlate. The composite shock rise time response behaves in a similar fashion to simply adding more particulates of a single size, as seen in Figure 5.37. The estimated rise times underestimate those that are observed, similar to what was seen in the single mode particle results. As heterogeneity is increased, sharp localized reflection interaction and tension become more significant, and interface degradation may begin to play a larger role.

As the difference in bead diameter increases back towards that in Figure 5.36, the underestimation of shock wave rise time again increases as seen in Figure 5.38. The 50% glass by volume bi-mode composite increases the shock rise time over the rise time seen in a 40% glass by volume single mode composite by a considerable margin. The 700 μm - 300 μm bi-mode composite is the final composite

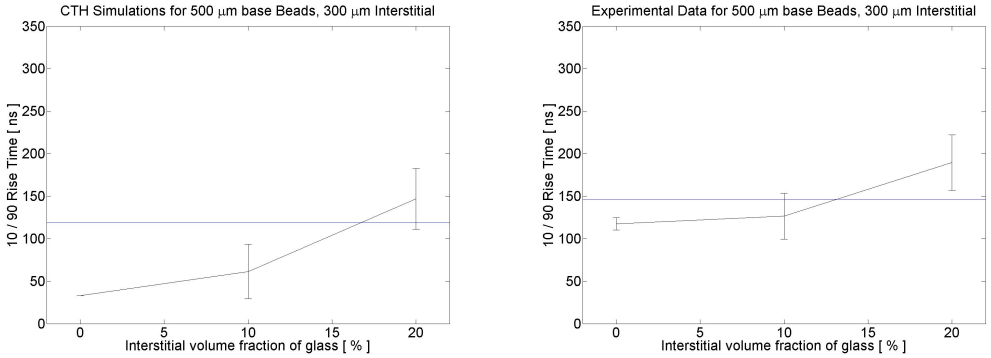

(a) Simulation results (b) Experimental results

Figure 5.37: Simulation and experimentally observed shock rise times for 30% volume fraction 500 μm glass beads base with 300 μm interstitial glass beads in a PMMA matrix. Impactor is 6061-T6 aluminum.

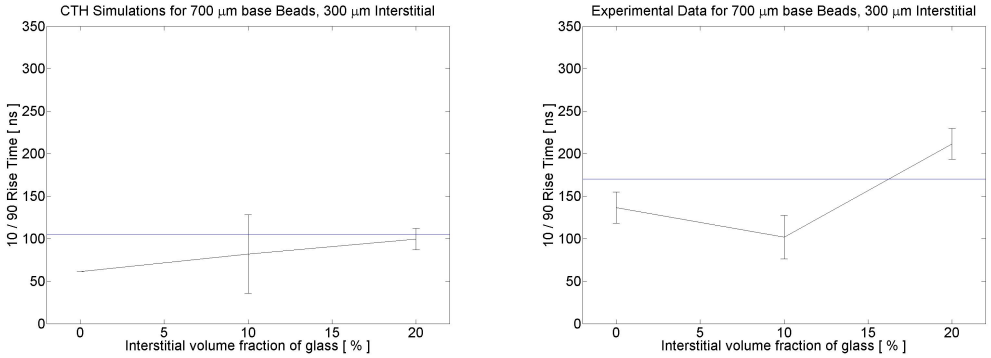

(a) Simulation results (b) Experimental results

Figure 5.38: Simulation and experimentally observed shock rise times for 30% volume fraction 700 μm glass beads base with 300 μm interstitial glass beads in a PMMA matrix. Impactor is 6061-T6 aluminum.

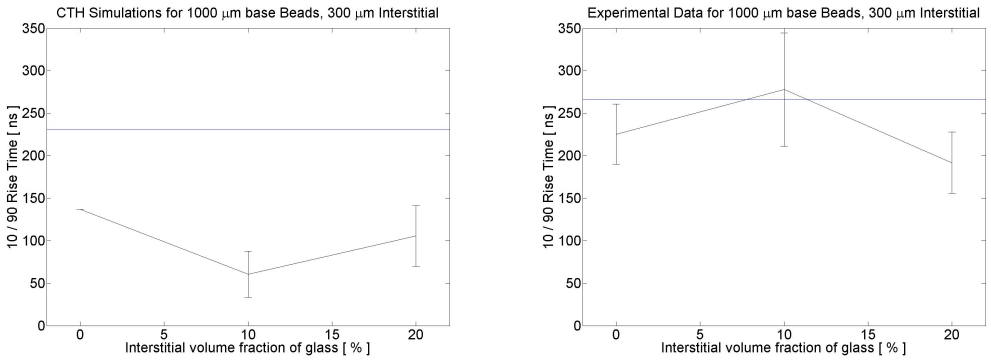

(a) Simulation results (b) Experimental results

Figure 5.39: Simulation and experimentally observed shock rise times for 30% volume fraction 1000 μm glass beads base with 300 μm interstitial glass beads in a PMMA matrix. Impactor is 6061-T6 aluminum.

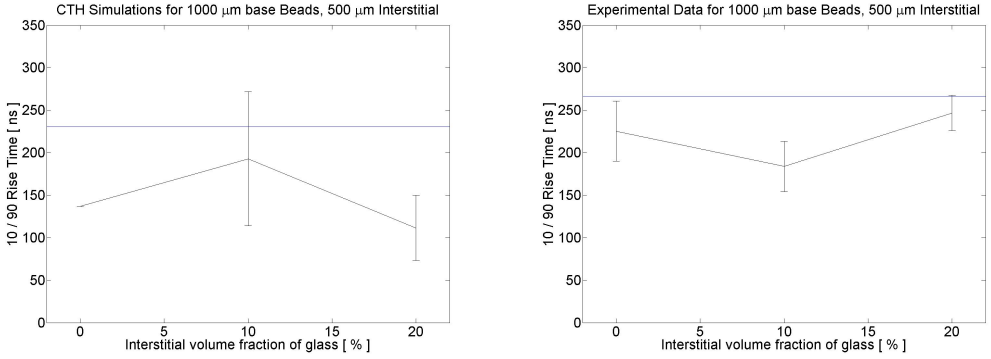

(a) Simulation results (b) Experimental results

Figure 5.40: Simulation and experimentally observed shock rise times for 30% volume fraction 1000 μm glass beads base with 500 μm interstitial glass beads in a PMMA matrix. Impactor is 6061-T6 aluminum.

to display a large rise time increase over the 40% glass by volume single mode result. The base mix beads, at 700 μm in diameter, are still small relative to the wavelength of the incoming wave to be scattered, so that the effect of scattering is enhanced with the addition of smaller beads.

Figures 5.39 and 5.40 show the rise time dependence of a 1000 μm base mix at 30% glass by volume with either 300 μm or 500 μm interstitials. While the bi-mode composites demonstrate rise time increases with the addition of smaller interstitials to some degree, the 1000 μm bi-mode composites do not show significant rise time increases above the 40% glass by volume single mode case. Rise times appear to approach a maximum or saturated value. Moving to larger and larger beads will not produce a significant change in rise time, and as the spacing between beads increases

with increasing mean diameter. It is possible that a higher volume fraction of smaller interstitial beads is required to effect an increase in shock rise time in composites with a large mean diameter dominating base mix. The 1000 μm beads may be approaching the limit of scattering effectiveness, as postulated by Rayleigh and described in Equation 2.33 in the case of elastic scattering. Much the same as having inclusions of a smaller/similar diameter as the shock thickness in the pure matrix material reduces scattering effectiveness, having oversize particulates may also result in reduced scattering efficiency, as the the tendency for shocks to steepen in homogeneous materials is not balanced by reflections at interfaces.

Due to the structure of the solver and meshing in CTH, resolving the interfaces in these highly complex composites becomes increasingly challenging. It is possible that the smoothing of interfaces due to volume fraction based material property averaging within cells that include interfaces results in reduced scattering effectiveness in the simulation results. It is clear from the single mode composite results that increasing interface density increases both primary and secondary stress wave reflections. These waves interact, and cause high local hydrostatic and shear stresses. It is likely that matrix damage, interface separation, and crushing of glass beads add an additional heterogeneous "phase" that is not accounted for in the current CTH simulations.

Chapter 6

Conclusions

6.1 Summary

An examination of shock wave structure as a function of microstructure in particulate composites similar to UHPC concretes and polymer bonded explosives was undertaken to determine the effects of particle size and density on scattering effectiveness and shock front thickening. A model particulate composite, with an impedance mismatch ratio falling within the range bounded by polymer bonded explosives on the low end and concretes on the high end was developed to match interface bonding conditions of the engineering materials of interest and provide a simple repeatable geometry to model. The model particulate composite consisted of finely graded glass spheres in a matrix of PMMA polymer, and was fabricated using a vacuum assisted compression molding process. The glass spheres used in the composite fabrication process were sorted through the use of stainless steel mesh sieves to generate five mono-disperse bead diameter distributions in over a 100 μm to 1000 μm diameter range. Residual stresses were relieved with a two-step heat treating process, which first relieved axial stresses and then radial stresses before slowly cooling.

Composites were fabricated with a variety of bead sizes, with glass bead loading of 30%, 40%, and 50% by volume. Plate impact loading was used to generate strong planar shocks in the composites (5 GPa), whose profiles were monitored with heterodyne velocimetry on the rear surface to determine the degree of shock profile modification.

Shock hydrocode simulations were undertaken to determine the appropriate bead diameters for

exploration, the degree of mono-dispersity required for reasonable results, and confirming that the structured waves were steady. Experiments were then completed with single mode and bi-mode bead diameter distributions and compared by using shock wave rise time as a metric. Statistics were generated by using multiple points on the rear of each composite target to account for spatial heterogeneity in shock response due to random placement of particulates. Shock thickness was found to scale linearly with particle diameter, with a constant of proportionality equal to the shock wave speed for composites with mono-disperse particle diameter distributions. This simple one parameter model may be used to predict shock rise times for a variety of materials, since the mechanical mismatch and impact velocity information is contained within the Lagrangian shock speed.

Chapter 2 of the thesis covers the theory and assumptions behind the propagation of 1D steady shock waves in condensed materials. Shock wave theory allows for the computation of estimated shock stress, density, strain, and energy change subject to a constitutive relation and measurement of two of five shock state properties. In the case of composite materials that are dispersive and scatter shock energy, the assumption of an infinitesimally thin shock front is no longer valid. It is useful, however to estimate average pressure states when the properties of the impactor plate are known.

Composite material response to shock loading is highly dependent on loading rate, and care must be taken to ensure that the wave propagation is steady. Low velocity impacts do not generate steady waves, and shock thickness grows with propagation distance due to viscous attenuation. Previous work examining Hugoniot states and strain rate dependence on pressure are discussed. Once a steady wave is generated with an impact of sufficient velocity in a plate impact experiment, a balance between the tendency of shocks to steepen with propagation distance in a homogeneous material, wave reflections, and viscous dissipation develops. These forces are dependent upon the composite microstructure and mechanical property mismatch of the constituents.

The shock structure of several composite systems is examined. The previous work found in literature falls into two subsets characterized by the impedance mismatch ratio of the constituents and the mean particle size. Potting compounds found in electronics subject to impact loading are

characterized by small, monodisperse particles that are very dense and have wave speeds much higher than the matrix materials. The bulk of the remaining studies were completed on low impedance mismatch ratio composites, with largely poly-disperse particle size distributions.

The model particulate composites in this study seek to bridge the gap of understanding that exists in low impedance mismatch composites such as concrete and polymer bonded explosives that are monodisperse in particle size distribution. Chapter 3 describes the experimental arrangement and process parameters critical to composite fabrication and particle velocity extraction during plate impact experiments. A 36 mm smooth bore powder gun is used to accelerate 6061-T6 aluminum alloy plates to 1 $^{km}/_{s}$ into the composite samples. A custom built 4 channel heterodyne laser velocimeter provides three particle velocity time histories from discrete points on the rear surface of the target, as well as an impact velocity within 1% accuracy. Particle velocity records were reduced to provide statistical rise time information for each experimental case.

A series of numerical simulations were performed using a special purpose numerical code, CTH, to provide an additional understanding of how the wave reflection within the material was influencing shock structure and thickness. Primary and secondary wave reflections were examined, as well as rear surface morphology in an effort to explain the experimentally observed shock wave structures. Once a comprehensive single mode bead diameter study was completed in CTH and validated against experimental data, the heterogeneity level of the composites was increased by moving to bi-modal bead diameter distributions and increased volume fractions of glass beads within the composites. In these highly heterogeneous materials, simple CTH simulations are unable to replicate the observed shock wave rise times due to unaccounted for interface degradation and resolution limitations.

After many unsuccessful VISAR [20] measurement attempts, it is clear from these studies that the use of heterodyne velocimetry as a diagnostic is robust to rear surface rippling and reflector degradation. This capability will be instrumental to further examination of heterogeneous materials where rippling and out-of-plane motion may compromise and complicate rear surface velocity measurements.

6.2 Future Work

Examination of shock wave structure experimentally and with CTH simulations raised as many questions as it has answered. One peculiar shock structure artifact that was observed was a significant short duration, large magnitude, particle velocity overshoot above the steady state particle velocity in composites composed of small (100 μm - 300 μm diameter) glass beads. A secondary wave reflection hypothesis was suggested in this work. The high interface density of the small particulate diameter composites produces more reflections, and the ones that propagate back toward the shock front pile up and drive a particle velocity overshoot. This overshoot was not observed for the largest bead diameters.

A preliminary reverse ballistics simulation was completed. Particle velocity oscillations were observed emanating from the composite material into the window in the case of smaller particulates. These fluctuations are 1 - 2 GPa above mean pressure in the window, and are thought to be sufficiently strong to drive re-compression waves back toward the shock front if they were to interact with another interface. Due to time constraints and infrared light transmission issues with windows available in the laboratory, reverse ballistics experiments were not completed. It would be ideal if the preliminary CTH simulations could be validated with reverse ballistics experiments. The simulations could then be tuned to match the magnitude and frequency of primary reflected waves emanating from the composite sample. Once that is completed, an examination of momentum or energy flux immediately behind the shock front may be completed with the validated and tuned CTH model. A positive value of flux would indicate that the overshoot phenomena is dependent on interface density, which is driven by particulate diameter at a fixed volume fraction.

The precise composite manufacturing process developed in 3.1 affords future researchers the opportunity to precisely vary particle diameter distribution as well as volume fraction. The present bi-mode bead diameter study clearly demonstrates the inadequacies of current hydrocode models in regard to interface resolution and wave scattering. The present data will provide bench mark data for model validation. Generation of additional permutations of bi-mode composites and the development of tri-mode or more complicated composites will serve as additional validation points

for modelers in addition to providing insight into the magnitude of the shock wave front disruption as a function of microstructure. The available data may be used to develop and tune damage models to account for interface degradation, matrix failure, and particulate crushing due to the complex stress states generated by multiple wave reflections.

The composite manufacturing process has one other advantage in that it can be changed in a simple manner to change the initial interface properties from a strong, perfectly bonded state to a relatively weak interface. Instead of long periods at elevated temperature to effect residual stress relaxation without incurring damage, composites may be subjected to a controlled quenching process to induce particle-matrix separation. The shock thickness/rise time as a function of particle diameter results may be re-evaluated experimentally, and new models developed to account for the difference in interface strength.

Until the technology behind high speed cameras advances to the point that full-field techniques such as digital image correlation may be used in plate impact experiments, the shock physicist will be left using some form of interferometry to measure particle velocities in the laboratory. The complex wave reflections call the uniaxial pressure wave propagation assumption in to question. Spherical particles may direct some shock energy laterally, in addition to the direction of mean shock front propagation. In order to better understand the magnitude of energy redirection in the lateral directions, a modification to the heterodyne velocimeter constructed for this study has been completed to allow for diffraction assisted transverse velocity measurements. The modification to a standard heterdyne velocimeter system (Heterodyne Transverse Velocity Interferometer, HTVI) is described in Appendix A.4. A standard plate impact experiment can be modified by the addition of a thin witness plate added to the rear surface, on which an appropriate grating may be etched.

The grating must be etched into a specular metal surface to survive the extreme conditions encountered in a shock wave experiment. The diffracted first order beams may be collected with passive PDV probes to provide both normal and transverse velocity information, while the normal incidence probe can provide an independent PDV confirmation record of normal velocity. While the current interferometer architecture only supports one direction of transverse velocity measurement,

and additional passive heterodyne interferometer system may be readily implemented and a two dimensional grating fabricated to provide a full characterization of particle velocity at the point of interest. Given a sufficiently thin witness plate, the complex velocity state will not be significantly attenuated, and the pressure/particle velocity in the sample back calculated. If exploration of material response under more complex loading conditions is desired, the HTVI may be employed in pressure shear experiments to probe strength of the composites. This novel approach will provide simulation groups and modelers additional velocity information which may then be used to further refine models of heterogeneous materials under shock loading.

Appendix A

PDV Fabrication Process

This section covers the plans and assembly processes used to construct the PDV system. For simplicity, the components have been divided up into three groups: Laser Drive and Target interrogation, Heterodyne Reference, and Multiplexing and Sensing. While only a small portion of the fabrication is presented, similar practices can be used to complete the whole assembly. It is recommended to start from the drive laser input of the interferometer system and gradually add components one at a time. It is also far simpler to identify improper connections and defective components when losses are incrementally checked against the losses listed on component specification sheets. A calibrated laser source and separate power meter is required to complete a build in such a manner.

A.1 Schematics

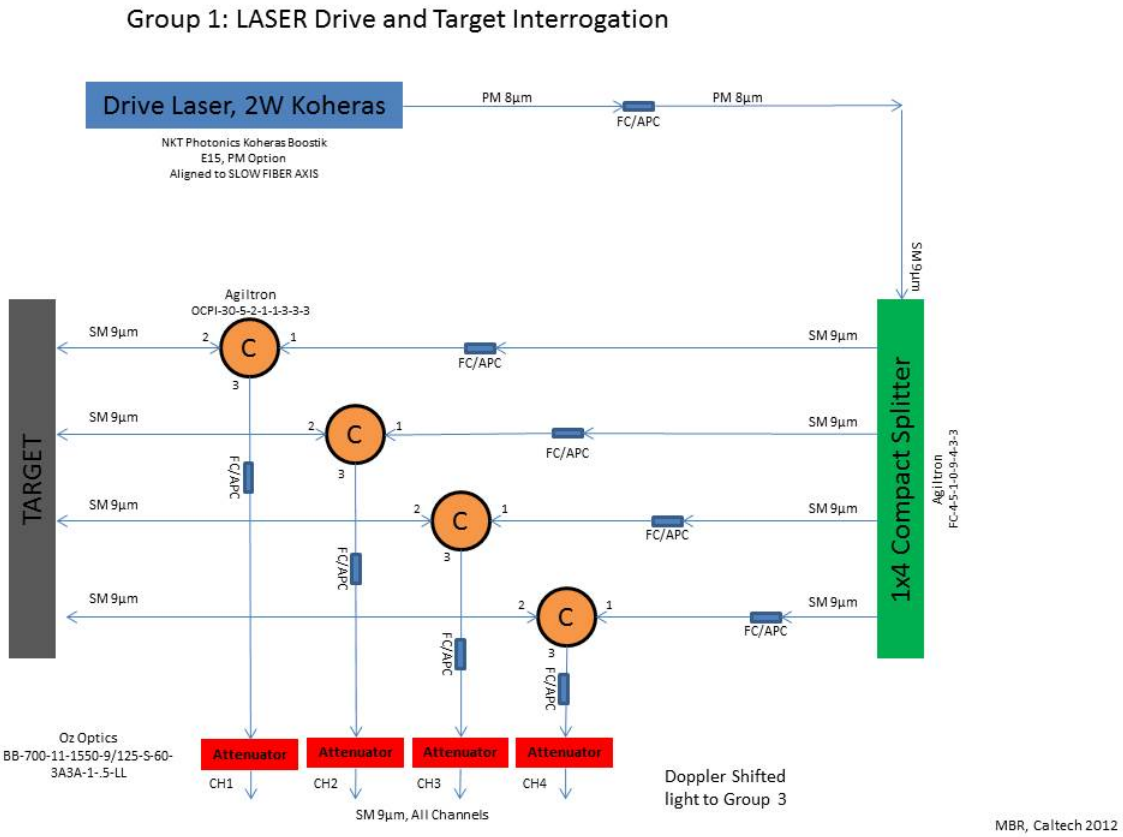

Figure A.1: PDV schematic - Component Group 1.

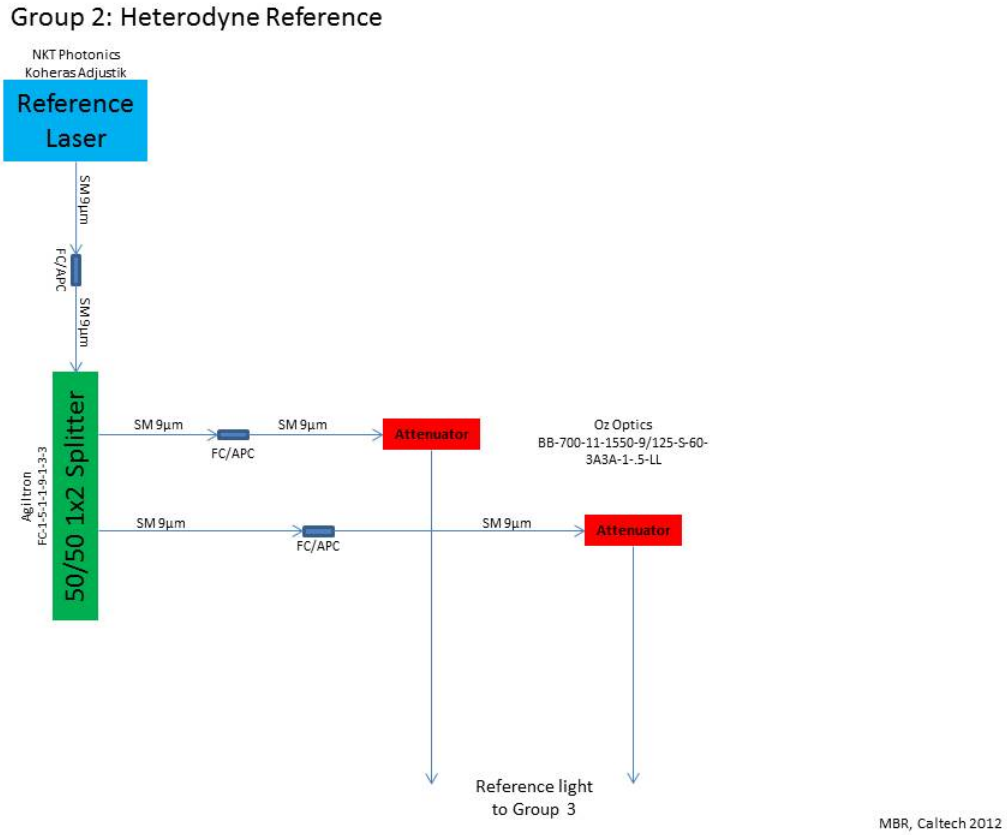

Figure A.2: PDV schematic - Component Group 2.

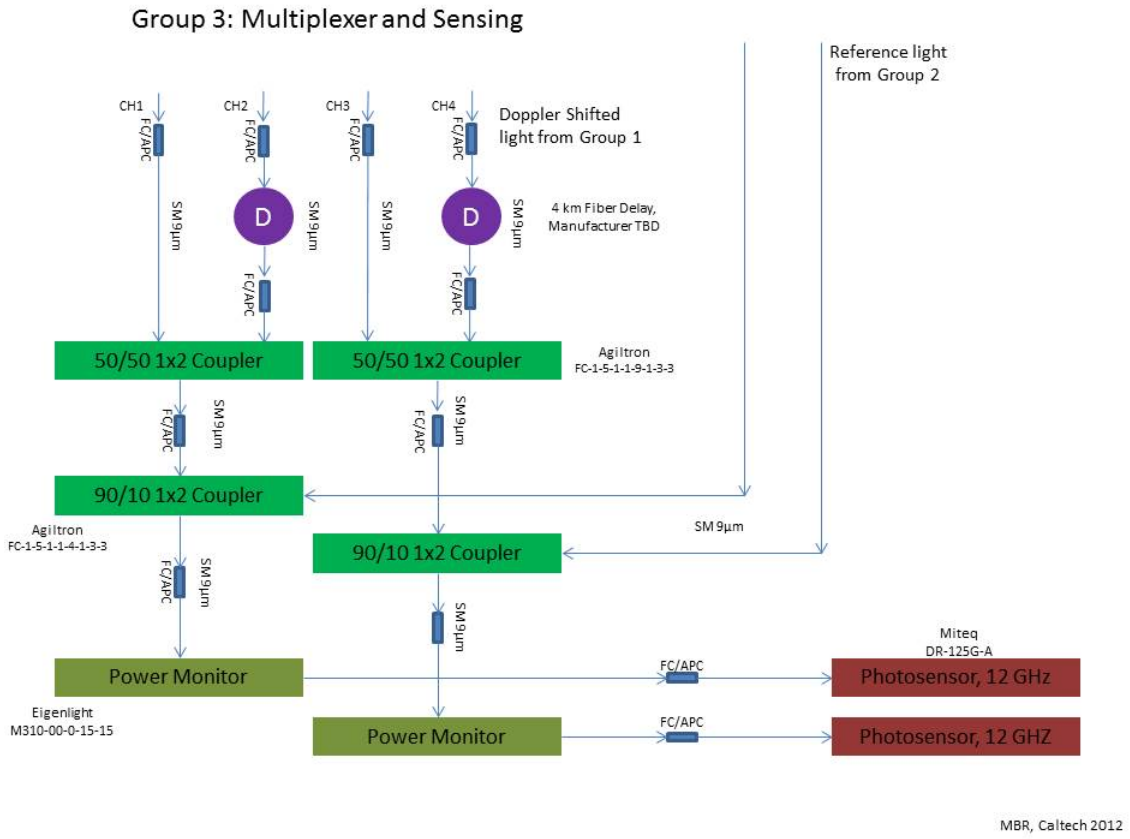

Figure A.3: PDV schematic - Component Group 3.

A.2 Assembly Procedures

As with free space optics, dust in the PDV system is a serious concern. Thankfully, once the fiber optic cables are assembled, there is very little risk of dust intrusion. So long as the connectors are not separated, no cleaning or maintenance is required before using the PDV, as the fiber ends have been cleaned before the first assembly. The only reason to separate connections inside the PDV box is if there is a verified failure of one of the components. All connections to probes must be done on the sacrificial patch cables connected to channels 1-4 on the front panel of the device. That way the fiber ends of the expensive components inside are always protected. It is imperative to verify that the two fiber ends are clean and free from scratches and oil from your hands. If there is a bad connection, the high optical power of the laser can burn the fiber ends or the dust/dirt can scratch the cables as they are tightened.

Compressed air can be used to clean out the spare FC-APC bulkhead fittings before inserting the patch cable ends. Compressed air should not be used on the front connections of the PDV box. There are extra bulkhead fittings available to attach the purchased or fabricated PDV probes and isolators to the PDV input patch cables. These are the only connections that should have to be made during routine use. The fiber ends must still be verified as clean before attachment. Dirt can be removed with an Opti-pop cotton strip cleaner (NTT-AT, Kanagawa, Japan).

A.2.1 Maintenance

Under normal circumstances, the PDV itself should require no outside maintenance or modification. The only user serviceable components inside the box are the Eigenlight (Somersworth, NH) power meters. The batteries that power those two devices are intended to give several years of use. When the batteries require replacement, a low battery message will appear on the screen during use. Figure A.4 shows the interior layout of the PDV box, minus the photosensors:

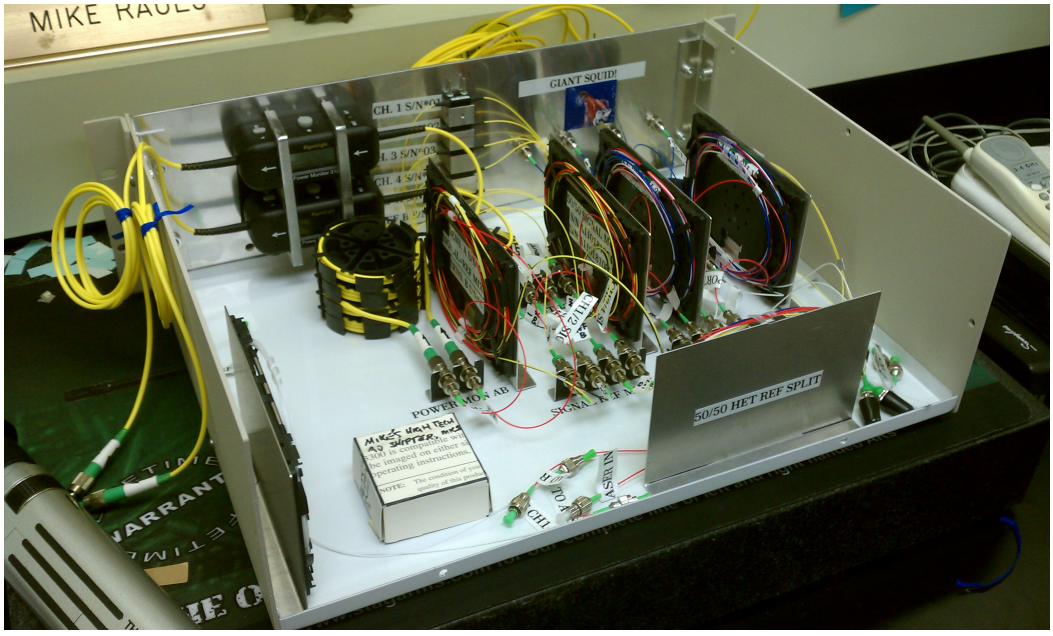

Figure A.4: PDV box interior layout.

To replace the batteries, follow the procedure below:

1. Disconnect, cover, and label the four optical cables going to and from the 4 km Cable Delay.

2. Loosen, but do not remove the two screws affixing the Delay box to the support rails.

3. Slide the Delay box up to remove, and then set it aside.

4. Remove the top cover (White Panel) of the PDV box.

   (a) Note: Do not remove the front panel of the PDV, the optical cables connected to the pass throughs are short, and may be damaged if strained.

5. Remove the Power Meter alignment bracket by removing the six stainless screws from the front of the Front Panel.

6. Carefully move the Power Meters as necessary to reach the battery compartments - the cables to the Power Meters and Attenuators are fragile.

7. Assembly is the reverse of the above.

A.3 Major Components

A.3.1 Fiber Lasers and Amplifier

A compact 2 watt boosted laser system for use in the drive group of the interferometer is provided by NKT Photonics (Birkerød, Denmark). The reference laser is also provided by NKT, and is a 40 mW version of the seeder laser with an extended tuning range and no booster module. The seeder laser is located above the booster module, with the reference laser above both in the interferometer equipment rack. The completed rack and oscilloscope are shown in Figure A.5.

The interlock ports on both the seeder and booster modules require special plug ends which should be removed to prevent unauthorized use when experiments are not running. The seeder and reference interlock plugs are simply bypasses; the laser interlocks are required to see a short circuit across the two leads on the interlock port. A LEMO 2-pin connector is provided with an internally shorted wire to accomplish this task. The seeder/reference plug (silver) and booster plug (black) are shown below in Figure A.6. Details on interlock function for future upgrades may be found in the appropriate manual provided by NKT Photonics.

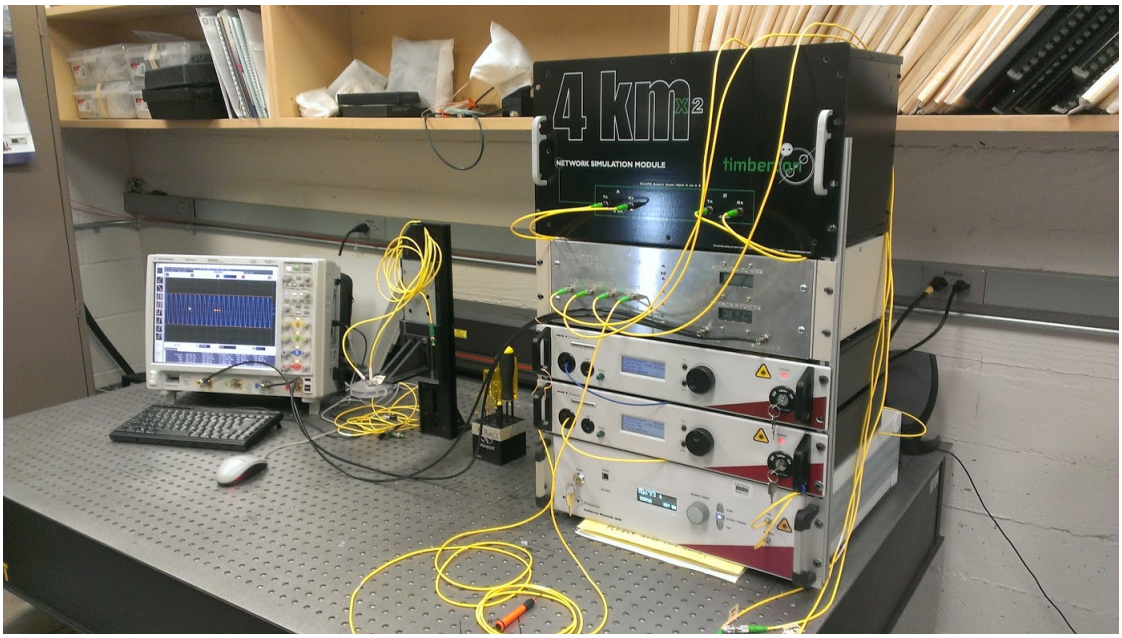

Figure A.5: Completed PDV Rack with boosted laser, reference, interferometer, and delay.

Both laser units require 120V AC power, and no additional cooling if the rear exhaust ports are kept clear of obstructions. Master switches are located on the rear, next to the power cord receptacle. These may be kept on, and the modules should be powered on to warm up before use. A 30 minute warm up period is required so that the thermally modulated laser cavity can reach operating temperature and maintain the desired wavelength. It is customary to keep the keys set to the Laser Off position for 30 minutes in order to allow the laser cavity to warm up to operating temperature. A Low Temperature warning will be active until the cavity heats up enough to emit at the chosen laser wavelength. It is possible that a unit that has not adequately warmed before use can have a sufficiently large wavelength difference from the other independent laser that the beat frequency lies outside of the oscilloscope bandwidth. Verify the cavity temperature and wavelength stability on the front panel. Laser power is controlled from the same front panel once the interlock overrides are installed into their respective ports.

Upon power up, the laser modules may display warnings or errors, which can be cleared manually. The explanations are available in the laser documentation. If the booster and seeder are powered on in the wrong order, the booster may display Warning: LIP. This is not listed in the laser manual,

Figure A.6: NKT laser interlock attachments.

but simply means low input power. To avoid seeing the LIP message, the seeder laser must be on before the booster can be made active. Cycle the laser key on the booster to clear the warning once the seeder is on.

The calibration documents list 5 mW of seeder power as the reference for the factory tests. The seeder is capable of 40 mW of output power. The power is set at the maximum output into the booster to increase the signal to noise ratio of the seeder light wavelength. The calibration at 5 mw is done to show that the booster will still operate in less than ideal conditions, but putting in higher power reduces high frequency noise. Main laser power is controlled by varying the pump current on the booster module. A calibration curve for 5 mW is shown below in the Booster Module section. The reference laser is patched in directly to the Miteq sensors. The Miteqs are easy to overdrive, and must not see over 1 mW of total power. Consequently, the reference laser will usually remain set at around 20 mW and still need to be attenuated by the adjustment on the front panel to avoid overdriving the Miteq sensors.

A choice of laser wavelength is available in the seeder. The components within the PDV box have been specified for 1550nm laser light, with a varying bandwidth per component. To ensure

best performance, the seeder laser should be set as close to 1550nm (1550.12nm) as possible. There is a single fiber patch cable that starts from the front of the seeder module box. It is marked with a "LASER APERTURE" tag, and it must be connected by a clean FC-APC barrel. A low temperature warning is possible on start up, but does not persist in use. Clear the warning, and let the laser warm up for a reasonable amount of time before measurement use.

Output power for the entire drive laser system is set by the booster module. When there is laser intensity detected at the input, the current to the cavity can be activated. It is slightly counterintuitive, but the only indicator of output intensity will be the amperage provided to the cavity. Under no condition should the handheld power meters be used to indicate the output power of the main laser, or even its split channels 1-4. Figure A.7 below is the best indicator for approximate output power. The precision of this output is more than adequate for our purposes: for prepared target surfaces, 100 - 500 mW total output should be more than sufficient. Start at 100 - 200 mW output power, and use the attenuators on the front panel to limit returned light. The booster output

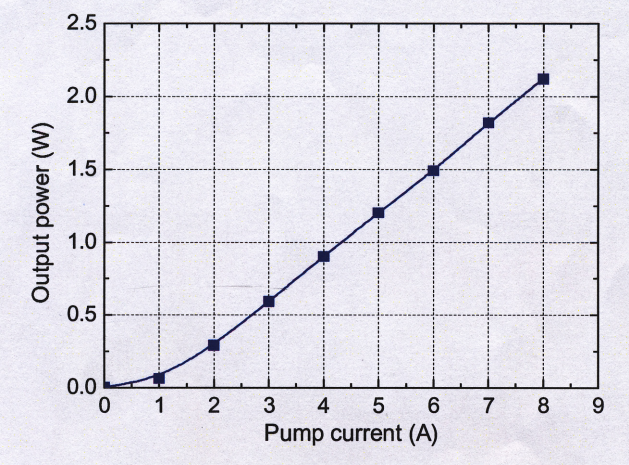

Figure A.7: Boosted laser output as a function of drive current for NKT Boostik.

should never have to be removed from the PDV box. The cleanliness of this connector is critical, as any dirt between the fiber faces can cause scorching due to the high laser power and permanent damage to the fibers. Thus, it's best to leave them together to avoid having to clean them thoroughly before every assembly.

A.4 Transverse Velocimetry Modification to Heterodyne PDV

The emergence of PDV into the forefront of shock physics experiments has come about mainly due to the introduction of very high bandwidth oscilloscopes, as previously mentioned. This fact bears repeating, especially considering that VISAR [20] [40] and other interferometric techniques for measuring surface motion were devised to reduce the necessary bandwidth for high velocity impact studies. Displacement interferometers generate one "fringe", or cycle between light and dark, for every increment of motion of the target surface proportional to one half of the wavelength ($^{\lambda}/_{2}$) of the illuminating light. Consequently, it was important to desensitize interferometers for shock physics use to sensitivities on the order of $^{\lambda}/_{2} - 10\lambda$.

The study of heterogeneous and anisotropic materials and non normal impact geometries necessitated the development out of plane velocity measurements. These measurements were subject to the same bandwidth limitations as those faced by normal velocity interferometers. Just as VISAR provided a solution for normal motion, one of several designs implemented to desensitize transverse displacement interferometers for use with slow recording equipment is the Variable Sensitivity Displacement Interferometer (VSDI) developed at Brown University [35]. VSDI is a diffraction assisted displacement interferometer capable of resolving both normal and transverse motion of a grating affixed to the rear surface of a target plate in gas gun experiments. Its primary use is to determine the structure and magnitude of a shear wave pulse traveling through a solid material undergoing combined pressure and shear loading. This experimental arrangement, known as Pressure Shear Plate Impact (PSPI) generates combined loading in a thin foil of a material of interest sandwiched between two high shock impedance anvils. The surface normal of the composite stack is then inclined relative to the direction of impact. A keyed gas gun is then used to propel a similarly inclined flyer plate, which generates normal and transverse motion in the target plate due to the impact direction being inclined relative to the impact surfaces.

In-plane motion measured in PSPI experiments may then be used to evaluate material strength parameters and yield surfaces. With the current interest in heterogeneous materials, observation of in-plane motion during shock loading has become a limiting factor in experiment design. The

magnitude of in-plane motions may give insight into scattering phenomena in particulate composites, as well as energy re-direction in blast protection schemes. Measuring both the transverse and normal velocity components at a single point would then be ideal.

Typical VSDI interferometer designs employ open beam arrangements and visible light to make these measurements. A modification to an existing multi-channel PDV system is proposed to extract transverse motion similar to Transverse Displacement Interferometry (TDI) [43] in addition to high resolution normal motion. The advantage of the new system as proposed is that it also allows for simultaneous PDV at the exact same point being observed. This new device is called the Heterodyne Transverse Velocity Interferometer (HTVI).

The illuminating probe is located normal to the surface, and illuminates the grating immediately in front of it on the target surface. The illuminating probe is not used for HTVI, but light collected back by the illuminating probe may then be directly used for PDV. The grating diffracts the light falling on it, and the 1^{st} and -1^{st} order diffracted beams are collected and coupled into optical fiber, using commonly used PDV collimating probes. The diffracted light is then mixed with a stationary reference. The architecture of an upshifted PDV device allows for this specific light path, provided that the emission from the probes collecting the diffracted light can be eliminated. The remaining downstream components of the PDV system match identically a stand-alone HTVI.

Changing an existing PDV device should not compromise its capability to be used as originally intended, nor should the conversion involve disassembling the device every time the experimenter wishes to use HTVI. Repeated disassembly and reassembly can introduce dirt particles between the faces of the optical lines. At high laser power, scorching of dirt between the fiber faces will cause permanent damage and performance degradation. An additional piece of telecom and scientific equipment now in common use is the electronically activated fiber shutter and beam stop. With the addition of two shutters, the interferometer may be readily changed from PDV to HTVI with the flip of a switch, and no accumulated damage after each conversion back and forth. Test instrumentation will remain compact and out of the way of the blast chamber, with no additional optical cables to run.

A.4.1 Diffraction Optics and Target Arrangement

It is a requirement of HTVI that a grating is applied to the rear surface of the target face. As opposed to the PDV case where a diffusely reflective surface is required for optimal performance, the target surface must be prepared in such a way that it is specular when coated with a reflector. Probe placement, interferometer sensitivity, and diffraction efficiency are all dependent both on line count and wavelength of the laser light used to illuminate the target. Assuming that the illuminating beam is oriented normal to the target surface, the first order diffracted beams will be be emitted from the that surface at an angle θ away from the normal given below:

$$\sin(\theta) = \lambda p \tag{A.1}$$

Wavelength is given by λ, and p is the grating pitch in lines per millimeter. Rear surface visibility constraints and the illumination wavelength limit the maximum diffraction angle in the target chamber. Target holding setups that leave the rear surface of the target more exposed can be capable of higher angles. Here, the diffraction angle will be set to 40°. Choosing 40° for the diffraction angle increases the resolution of transverse displacement measurement, since displacement per fringe is inversely proportional to the number of lines per unit distance of the grating. In other words, so long as a first order beam can be diffracted at the illuminating wavelength, the resolution of the interferometer is only dependent on the pitch of the grating. For the target holding apparatus in the catch tank at this time, 40°is readily attainable, and does not sacrifice much in the way of normal measurement resolution, as will be seen later.

The first order diffracted beam is chosen to maximize efficiency and ensure that adequate light is collected by the probes. For reasons explained in Section 3.3.1, the PDV operates at $\lambda = 1550$ nm. Substituting,

$$\sin 40^\circ = 1550 \times 10^{-6}\ mm \times p \tag{A.2}$$

$$p = 414.7\ LPmm \tag{A.3}$$

Microfabrication techniques including photolithography and ion etching are in common use in university laboratories. Parts suppliers can also create masks with nearly any line pitch for the desired diffraction angle. With the diffraction angle now known, the phase imparted on the diffracted beams during target motion can now be quantified.

A.4.2 Interference Calculation

The approach for examining phase accumulation and its relationship to displacement and velocity will be much the same as for the normal, unmodified PDV case. To determine our approach, construct a case where there is only normal target motion being observed by the probe collecting the diffracted beam. Normal motion is given by the quantity $u(t)$, and θ is the diffraction angle. In Figure A.8, the reflector moves to the right from position A to position B. The dotted line

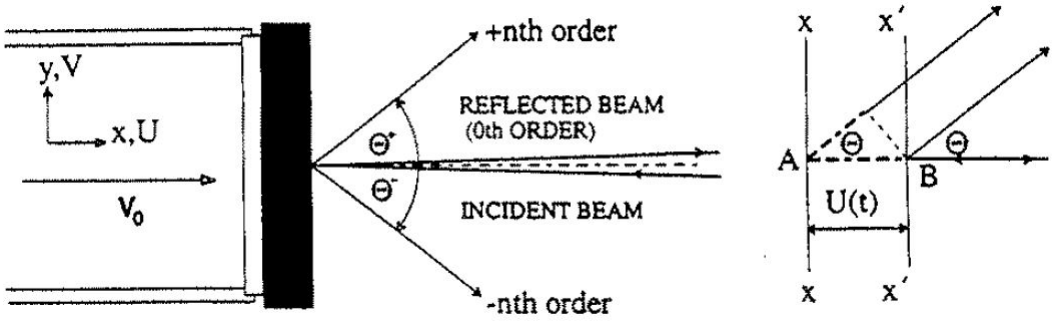

Figure A.8: Phase imposed by normal target motion. Adapted from [35].

perpendicular to the diffracted beams passing through Point B is the reference line, after which the original and post motion beams accumulate the same amount of phase as they propagate into space and out of the figure. The difference in phase is then given by the lines BA and A to the dotted line. One leg is simply $u(t)$, and since the diffraction angle is known, the other is $u(t)\cos\theta$. Converting into optical phase space,

$$\Delta\phi = \frac{2\pi}{\lambda}u(t)(1+\cos\theta) \tag{A.4}$$

With that in mind, composing the combined phase change for a normal and transverse motion is readily accomplished. The transverse motion is accounted for with the quantity $v(t)$. We may

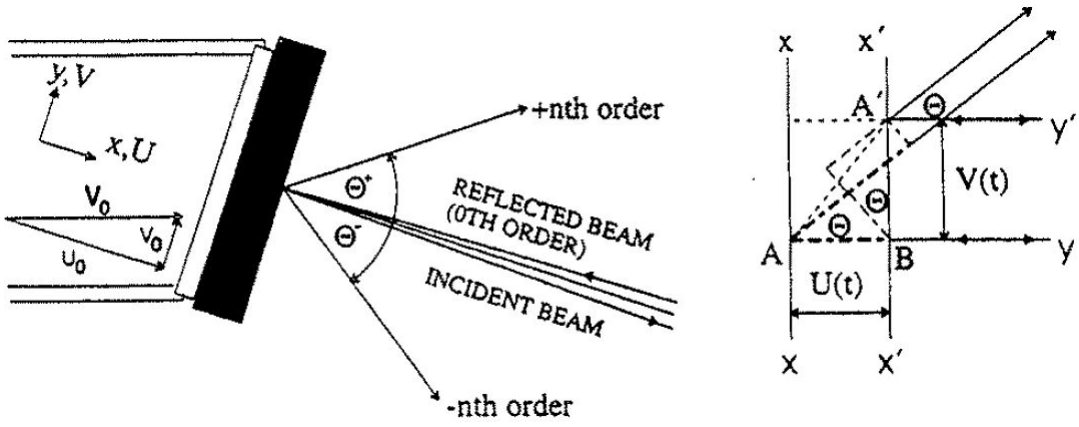

Figure A.9: Phase imposed by combined normal and transverse target motion. Adapted from [35].

use a similar construction line based technique to compute the additional phase added by transverse motion. Since the point of motion accounted for by normal motion is known, a reference line is drawn through Point A', parallel to the line passing through Point B (perpendicular to the diffracted ray). The distance between these parallel lines is then the added phase. Employing the properties of angles between parallel and intersecting lines, the change in optical phase is,

$$\Delta\phi = \frac{2\pi}{\lambda} v(t) \sin\theta \tag{A.5}$$

The change in phase is positive in this case. For the opposite order diffracted beam, there would be less phase accumulation, and the sign of the right hand side of Equation A.5 would be negative. Consequently, the combined phase change for both beams for arbitrary motion is given by,

$$\begin{aligned} \Phi^{+} &= \frac{2\pi}{\lambda} \left[u(t)(1+\cos\theta) + v(t)\sin\theta\right] + \phi_0^{+} \\ \Phi^{-} &= \frac{2\pi}{\lambda} \left[u(t)(1+\cos\theta) - v(t)\sin\theta\right] + \phi_0^{-} \end{aligned} \tag{A.6}$$

In the VSDI technique, the above diffracted beams were interfered with a normally reflected beam from the same target surface. Due to the way in which phase is also accumulated in the normal beam at the same time, the interference pattern produced results in fewer fringes per unit of displacement. This de-sensitization of the instrument was advantageous during the dark ages of low bandwidth oscilloscopes. Changing the grating pitch is a simple means of varying the level of de-sensitization,

and could be used for experiments where higher velocities were expected, or bandwidth was not available. Current measurement capabilities have removed the bandwidth limitation that motivated VSDI. The proposed design uses the same stationary, tunable reference found in many PDV devices in common use in shock physics laboratories.

When interfered with the target light, the tunable reference beam may be considered as a plane wave, with an electric field of the following form:

$$\mathbf{E}^R(\mathbf{r},t) = A^0 e^{i(\mathbf{k}_R\cdot\mathbf{r}-\omega_R t-\phi_R(t))} \tag{A.7}$$

Since the reference is stationary, the imposed phase as a function of time remains constant such that $\phi_R(t) = \phi_R$, independent of time. Subsequently, the diffracted beam electric fields are given,

$$\begin{aligned}\mathbf{E}^+(\mathbf{r},t) &= A^+ e^{i(\mathbf{k}_T\cdot\mathbf{r}-\omega_T t-\Phi^+(t))}\\ \mathbf{E}^-(\mathbf{r},t) &= A^- e^{i(\mathbf{k}_T\cdot\mathbf{r}-\omega_T t-\Phi^-(t))}\end{aligned} \tag{A.8}$$

For clarity in Equations A.7 and A.8, light coming from the reference and light coming from the target have been separated with subscript identifiers R and T, respectively. Diffracted beams are identified with superscript $\pm$ as well. The time varying phase terms, $\Phi^i(t)$, in Equation A.8 are shorthand for the information in Equation A.6. This plane wave formulation makes it simple to determine what happens in the 2x2 fiber combiner, as was done in Section 3.3.1. The combined field is then,

$$\begin{aligned}\mathbf{E}_1 &= \mathbf{E}^+ + \mathbf{E}^R\\ \mathbf{E}_2 &= \mathbf{E}^- + \mathbf{E}^R\end{aligned} \tag{A.9}$$

For simplicity's sake, only the interference pattern for $\mathbf{E}_1$ will be computed. The phase information may not be directly observed due to the high angular frequency of the light itself; we observe the time averaged intensity, as defined in Equation 3.16. The multiplication of the combined $\mathbf{E}$ field with its complex conjugate yields constant intensity terms along with an oscillatory portion that is

visualized as "fringes" on the oscilloscope screen. Simplifying,

$$I_1 = I_R + I_T + 2\sqrt{I_R I_T}\cos(\psi_R - \psi^+(t)) \tag{A.10}$$

Define ψ as the argument of the cosine term,

$$\psi = \psi_R - \psi^+(t) = (\mathbf{k}_R - \mathbf{k}_T)\cdot\mathbf{r} + (\omega_T - \omega_R)t + (\phi_R - \frac{2\pi}{\lambda_T}(u(t)(1+\cos\theta) + v(t)\sin\theta) - \phi_0^+) \tag{A.11}$$

ψ contains all of the phase change measured by the oscilloscope, and is a linear combination of the u and v displacement of the rear surface. There are also fringes generated at zero target motion when $\omega_T \neq \omega_R$. In shock experiments, analysis is typically done with surface velocity as opposed to its displacement. If surface velocity is desired without numerical differentiation of displacement data, we may assume that for a short enough observation period, the velocity of the target surface is approximately constant. With this in mind, extracting ${}^{\Delta\psi}/_{\Delta t}$ directly with an FFT or wavelet approach can immediately give the surface velocity. Begin by multiplying the displacement induced phase change term by one, ${}^{\Delta t}/_{\Delta t}$.

$$\psi = (\mathbf{k}_R - \mathbf{k}_T)\cdot\mathbf{r} + (\omega_T - \omega_R)t + (\phi_R - \frac{2\pi}{\lambda_T}(u(t)(1+\cos\theta) + v(t)\sin\theta)\frac{\Delta t}{\Delta t} - \phi_0^+) \tag{A.12}$$

Compute the change in phase accumulated between time t and $t+\Delta t$,

$$\Delta\psi = \psi(t+\Delta t) - \psi(t) = (\omega_T - \omega_R)\Delta t - \frac{2\pi}{\lambda_T}((u(t+\Delta t) - u(t))(1+\cos\theta) + (v(t+\Delta t) - v(t))\sin\theta)\frac{\Delta t}{\Delta t} \tag{A.13}$$

In the limit of Δt going to zero, the instantaneous angular frequency is given as follows:

$$\omega_s^+ = \lim_{\Delta t\to 0}\frac{\Delta\Phi}{\Delta t} = \lim_{\Delta t\to 0}\left((\omega_T - \omega_R) - \frac{2\pi}{\lambda_T}\left((1+\cos\theta)\frac{u(t+\Delta t) - u(t)}{\Delta t} + \sin\theta\frac{v(t+\Delta t) - v(t)}{\Delta t}\right)\right) \tag{A.14}$$

$$\omega_s^+ = (\omega_T - \omega_R) - \frac{2\pi}{\lambda_T}\left((1+\cos\theta)u'(t) + \sin\theta v'(t)\right) \tag{A.15}$$

With the identity $\omega = 2\pi f$, transform the interference into frequency space and the apparent frequencies from each diffracted beam become,

$$\begin{aligned} f^+ &= (\omega_T - \omega_R) - \frac{1}{\lambda_T}((1+\cos\theta)u'(t) + \sin\theta v'(t)) \\ f^- &= (\omega_T - \omega_R) - \frac{1}{\lambda_T}((1+\cos\theta)u'(t) - \sin\theta v'(t)) \end{aligned} \tag{A.16}$$

Therefore, extracting frequency from the two time history records gives two velocity traces, which may then be added and subtracted to separate normal and transverse velocity components. Having a carrier frequency present assists in removing ambiguity from velocity reversals, as well as improving time resolution by decreasing the necessary FFT window length to extract frequency information. Separating the velocity components and removing the carrier yields:

$$\begin{aligned} u'(t) &= -(f^+ + f^-)\frac{\lambda_T}{2(1+\cos\theta)} \\ v'(t) &= -(f^+ - f^-)\frac{\lambda_T}{2\sin\theta} \end{aligned} \tag{A.17}$$

Appendix B

Raw Experimental Data

B.1 Single Mode Particle Velocity Time Histories

The additional particle velocity time histories for single mode bead distributions with 30% glass beads by volume are presented below on Figures B.1, B.2, B.3, B.4, and B.5. Analysis of the information in these wave profiles is located in Section 5.1.2.2.

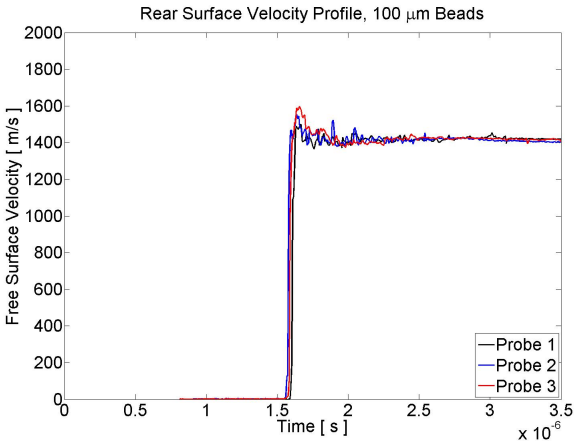

Figure B.1: Particle velocity time history for 30% volume fraction 100 μm glass beads in a PMMA matrix. Impactor is 6061-T6 aluminum with impact velocity 1006 $^{m}/_{s}$.

B.2 Bi-mode Particle Velocity Time Histories

Time histories of bi-mode bead diameter distribution composites are presented in Figures B.6, B.7, B.8, B.9, B.10. A detailed analysis of these wave profiles is available in Section 5.2.

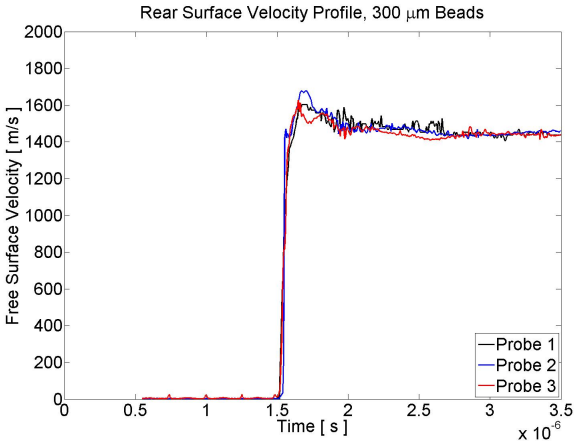

Figure B.2: Particle velocity time history for 30% volume fraction 300 μm glass beads in a PMMA matrix. Impactor is 6061-T6 aluminum with impact velocity 1019 $^{m}/_{s}$.

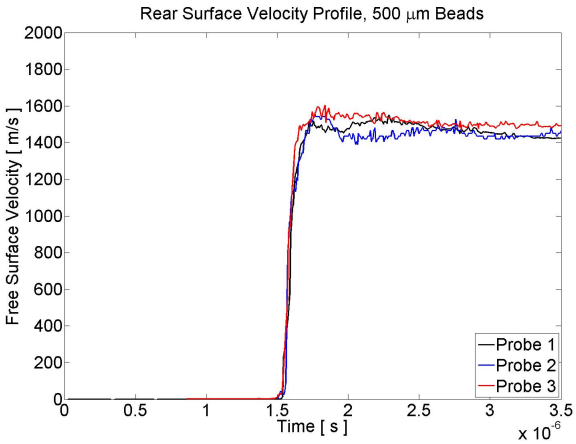

Figure B.3: Particle velocity time history for 30% volume fraction 500 μm glass beads in a PMMA matrix. Impactor is 6061-T6 aluminum with impact velocity 1009 $^{m}/_{s}$.

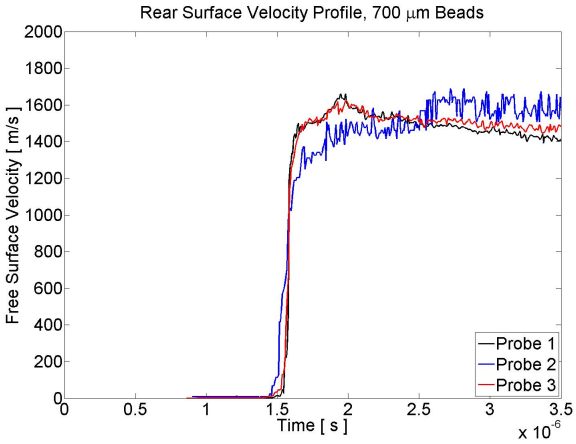

Figure B.4: Particle velocity time history for 30% volume fraction 700 μm glass beads in a PMMA matrix. Impactor is 6061-T6 aluminum with impact velocity 1009 $^{m}/_{s}$.

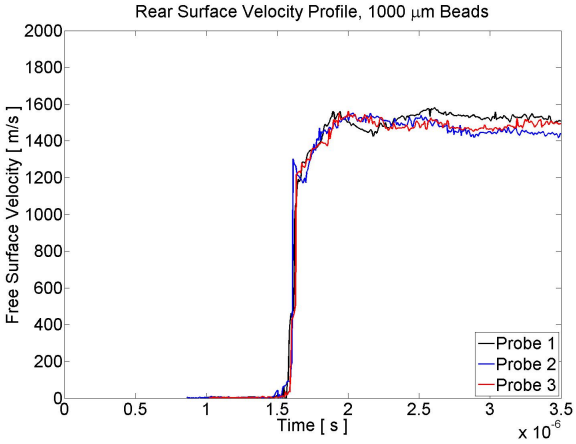

Figure B.5: Particle velocity time history for 30% volume fraction 1000 μm glass beads in a PMMA matrix. Impactor is 6061-T6 aluminum with impact velocity 1009 $^{m}/_{s}$.

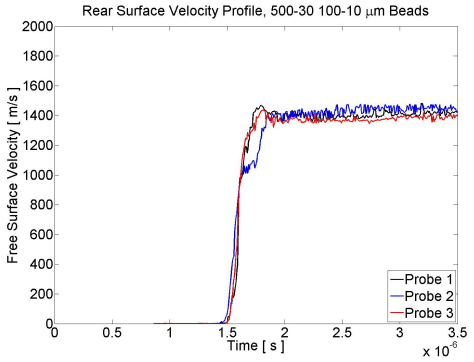

(a) 30% volume fraction 500 μm glass beads - 10% volume fraction 100 μm glass beads. Impactor is 6061-T6 aluminum with impact velocity 1007 $^{m}/_{s}$.

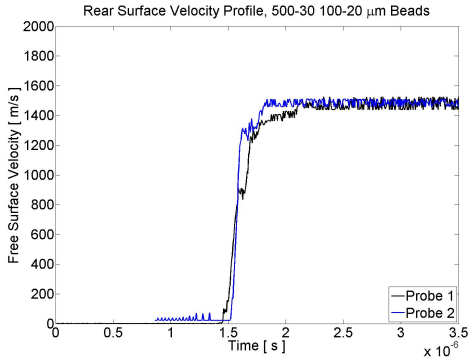

(b) 30% volume fraction 500 μm glass beads - 20% volume fraction 100 μm glass beads. Impactor is 6061-T6 aluminum with impact velocity 1010 $^{m}/_{s}$.

Figure B.6: Time histories for 30% volume fraction 500 μm glass beads base and 100 μm interstitial glass beads in a PMMA matrix.

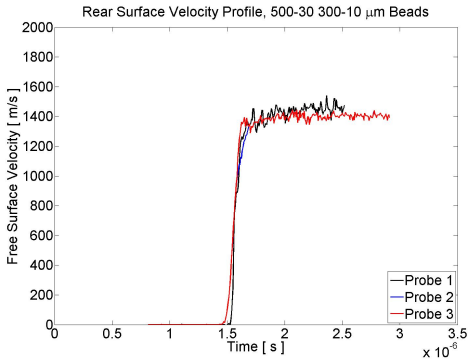

(a) 30% volume fraction 500 μm glass beads - 10% volume fraction 300 μm glass beads. Impactor is 6061-T6 aluminum with impact velocity 1004 $^{m}/_{s}$.

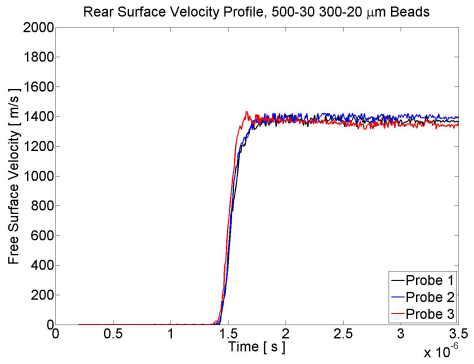

(b) 30% volume fraction 500 μm glass beads - 20% volume fraction 300 μm glass beads. Impactor is 6061-T6 aluminum with impact velocity 1005 $^{m}/_{s}$.

Figure B.7: Time histories for 30% volume fraction 500 μm glass beads base and 300 μm interstitial glass beads in a PMMA matrix.

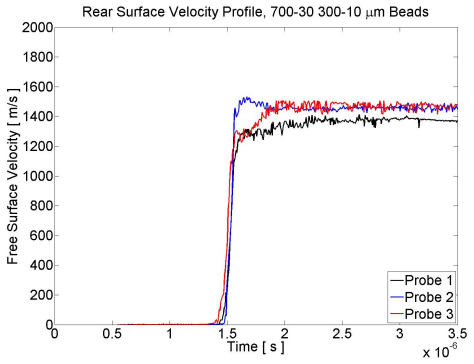

(a) 30% volume fraction 700 μm glass beads - 10% volume fraction 300 μm glass beads. Impactor is 6061-T6 aluminum with impact velocity 1008 $^{m}/_{s}$.

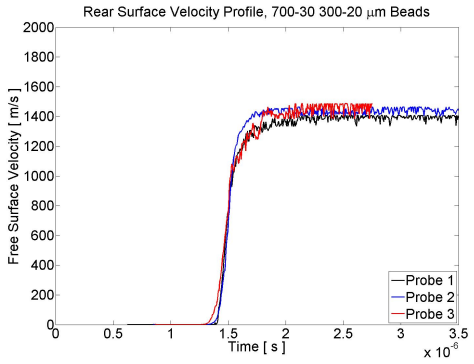

(b) 30% volume fraction 700 μm glass beads - 20% volume fraction 300 μm glass beads. Impactor is 6061-T6 aluminum with impact velocity 1008 $^{m}/_{s}$.

Figure B.8: Time histories for 30% volume fraction 700 μm glass beads base and 300 μm interstitial glass beads in a PMMA matrix.

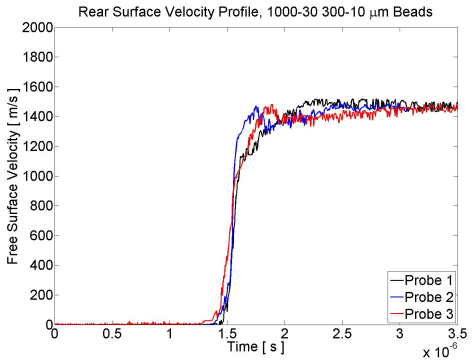

(a) 30% volume fraction 1000 μm glass beads - 10% volume fraction 300 μm glass beads. Impactor is 6061-T6 aluminum with impact velocity 1008 $^{m}/_{s}$.

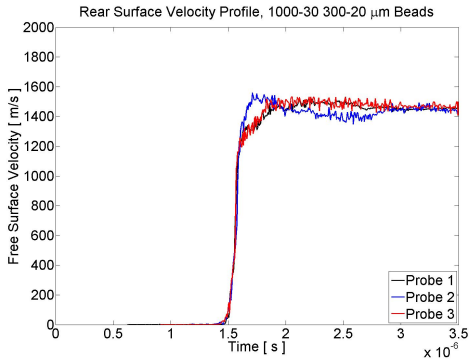

(b) 30% volume fraction 1000 μm glass beads - 20% volume fraction 300 μm glass beads. Impactor is 6061-T6 aluminum with impact velocity 1010 $^{m}/_{s}$.

Figure B.9: Time histories for 30% volume fraction 1000 μm glass beads base and 300 μm interstitial glass beads in a PMMA matrix.

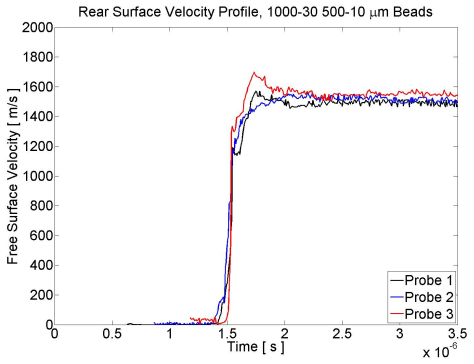

(a) 30% volume fraction 1000 μm glass beads - 10% volume fraction 500 μm glass beads. Impactor is 6061-T6 aluminum with impact velocity 1013 $^{m}/_{s}$.

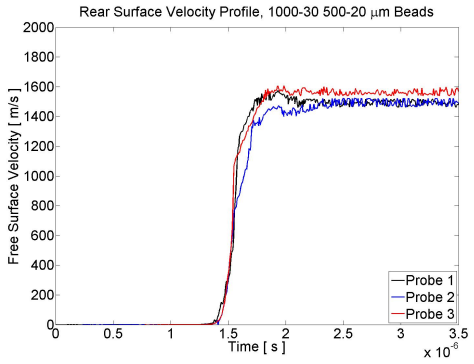

(b) 30% volume fraction 1000 μm glass beads - 20% volume fraction 500 μm glass beads. Impactor is 6061-T6 aluminum with impact velocity 1014 $^{m}/_{s}$.

Figure B.10: Time histories for 30% volume fraction 1000 μm glass beads base and 500 μm interstitial glass beads in a PMMA matrix.

Bibliography

[1] *Agilent Infiniium 9000 Series Oscilloscopes Data Sheet.*

[2] *CTH Eos Package: Introductory Tutorial.*

[3] *CTH Reference Manual: The Steinberg-Guinan-Lund Viscoplastic Model.*

[4] *CTH Reference Manual: The Viscous-Elastic-Plastic (VEP) Model.*

[5] *Dynasen Inc. Shorting Pins Data Sheet.*

[6] *Pin Mixer Model CS2-50-300 Instruction Manual.*

[7] *Papers on Mechanical and Physical Subjects.* Cambridge University Press, 1903.

[8] *Quantitative Microscopy.* McGraw-Hill, 1968.

[9] *Plastics Engineering Handbook.* Van Nostrand Reinhold Company, 1976.

[10] *Applied Statistics.* Allyn and Bacon, 1978.

[11] *Los Alamos Scientific Laboratory Shock Hugoniot Data.* University of California Press, 1980.

[12] *Plastics Processing Data Handbook.* Van Nostrand Reinhold Company, 1990.

[13] *Dynamic Behavior of Materials.* John Wiley and Sons Inc., 1994.

[14] *Plastics Materials.* Butterworth-Heinemann, 1999.

[15] *Physics for Scientists and Engineers.* Prentice Hall, 2000.

[16] *Practical Stereology.* Kluwer Academic / Plenum Publishers, 2000.

[17] *Fundamentals of Shock Wave Propagation in Solids*. Springer, 2008.

[18] M. R. Baer. Modeling heterogeneous energetic materials at the mesoscale. *Thermochimica Acta*, 2002.

[19] L. M. Barker and R. E. Hollenbach. Shock-wave studies of pmma, fused silica, and sapphire. *Journal of Applied Physics*, 1970.

[20] L. M. Barker and R. E. Hollenbach. Laser interferometer for measuring high velocities of any reflecting surface. *Journal of Applied Physics*, 1972.

[21] D. R. Bland. On shock structure in a solid. *Journal of the Institute of mathematics and Its Applications*, 1965.

[22] John P. Borg and Tracy J. Vogler. Aspects of simulating the dynamic compaction of a granular ceramic. *Modelling and Simulation in Materials Science and Engineering*, 2009.

[23] John P. Borg and Tracy J. Vogler. Rapic compaction of granular material: characterizing two- and three-dimensional mesoscale simulations. *Shock Waves*, 2013.

[24] Justin L. Brown. *High Pressure Hugoniot Measurements in Solids Using Mach Reflections*. PhD thesis, California Institute of Technology, 2011.

[25] David James Chapman, Daniel E. Eakins, David Martin Williamson, and William Proud. Index of refraction measurements and window corrections for pmma under shock compression. In *SHOCK COMPRESSION OF CONDENSED MATTER - 2011: Proceedings of the Conference of the American Physical Society Topical Group on Shock Compression of Condensed Matter*.

[26] X. Chen and N. Chandra. The effect of heterogeneity on plane wave propagation through layered composites. *Composites Science and Technology*, 2004.

[27] R. Cheret. The life and work of pierre henri hugoniot. *Shock Compression of Condensed Matter*, 1990.

[28] Rodney Clifton. Stress waves in solids course notes.

[29] William C. Davis. High explosives: The interaction of chemistry and mechanics. *Los Alamos Science*, 1981.

[30] J. J. Dick, A. R. Martinez, and R. S. Hixson. Plane impact response of pbx 9501 below 2 gpa. In *Proceedings of the 11th Symposium on Detonation.*

[31] D. H. Dolan. Accuracy and precision in photonic doppler velocimetry. *Review of Scientific Instruments*, 2010.

[32] Daniel Dolan. Extreme velocity: Pdv in cylindrical compression experiments. In *7th Annual Photonic Doppler Velocimetry (PDV) Workshop 2012.*

[33] J. Edwards, K. T. Lorenz, B. A. Remington, S. Pollaine, J. Colvin, D. Braun, B. F. Lasinski, D. Reisman, J. M. McNaney, J. A. Greenough, R. Wallace, H. Louis, and D. kalantar. Laser driven plasma loader for shockless compression and acceleration of samples in the solid state. *Physical Review Letters*, 2004.

[34] Russell Ellis. Explanation of reflectrion features in optical fiber as sometimes observed in otdr measurement traces. Technical report, Corning Incorporated, 2007.

[35] H. D. Espinoza, M. Mello, and Y. Xu. A variable sensitivity displacement interferometer with application to wave propagation experiments. *Journal of Applied Mechanics*, 1997.

[36] Reginald A. Fessenden. Wireless signalling. *US Patent 706740*, 1902.

[37] Dennis E. Grady. Scattering as a mechanism for structured shock waves in metals. *Journal of the Mechanics and Physics of Solids*, 1998.

[38] Dennis E. Grady. Structured shock waves and the fourth-power law. *Journal of Applied Physics*, 2010.

[39] C. A. Hall, L. C. Chhabildas, and W. D. Reinhart. Shock hugoniot and release states in concrete mixtures with different aggregate sizes from 3 to 23 gpa. In *Shock Compression of Condensed Matter - 1997.*

[40] Willard F. Hemsing. Velocity sensing interferometer (visar) modification. *Review of Scientific Instruments*, 1979.

[41] B. J. Jensen, D. B. Holtkamp, P. A. Brigg, and D. H. Dolan. Accuracy limits and window corrections for photon doppler velocimetry. *Journal of Applied Physics*, 2007.

[42] Jennifer L. Jordan, Eric B. Herbold, Gerrit Sutherland, Andrew Fraser, John Borg, and D. Wayne Richards. Shock equation of state of multi-constituent epoxy-metal particulate composites. *Journal of Applied Physics*, 2011.

[43] Kyung-Suk Kim, Rodney J. Clifton, and Prashant Kumar. A combined normal- and transverse-displacement interferometer with an application to impact of y-cut quartz. *Journal of Applied Physics*, 1977.

[44] Marlin E. Kipp, Lalit C. Chhabildas, and William D. Reinhart. Elastic shock response and spall strength of concrete. In *Shock Compression of Condensed Matter - 1997*.

[45] Wei-Zhong Li, Vincent Au-Yeung, and Qing-Dong Guo. Optical circulator. *US Patent 25532045*, 1997.

[46] Bradley Martin. Dynamic characterization and size effect of concrete materials. In *Society of Experimental Mechanics 2014*.

[47] Albert A Michelson and Edward W Morley. On the Relative Motion of the Earth and the Luminiferous Ether. *American Journal of Science*, 34:333–345, 1887.

[48] J. C. F. Millett, N. K. Bourne, and J. Akhavan. The response of soda-lime glass-hydroxyterminated polybutadiene composites to shock loading. *Journal of Applied Physics*, 2005.

[49] Stanley Minshall. Properties of elastic and plastic waves determined by pin contactors and crystals. *Journal of Applied Physics*, 1955.

[50] Christopher Neel. Reverse ballistics experiments of cor-tuf concrete. AFRL/RW Internship 2013.

[51] Christopher Neel and Naresh Thadhani. Shock hugoniot of composites of thv polymer matrix with 25 vol % 10 μm al_2o_3 or zrc particles. In *Shock Compression of Condensed Matter - 2009*.

[52] Christopher Neel and Naresh N. Thadhani. Shock compression response of alumina-thv composites. *Journal of Applied Physics*, 2011.

[53] Jacob K Notbohm. *Dynamics of Cell-Matrix Interactions in Three Dimensions*. PhD thesis, California Institute of Technology, 2013.

[54] R. E. Setchell and M. U. Anderson. Shock compression response of an alumina-filled epoxy. *Journal of Applied Physics*, 2005.

[55] R. E. Setchell, M. U. Anderson, and S. T. Montgomery. Compositional effects on the shock compression response of alumina-filled epoxy. *Journal of Applied Physics*, 2007.

[56] O. T. Strand, D. R. Goosman, C. Martinez, T. L. Whitworth, and W. W. Kuhlow. Compact system for high-speed velocimetry using heterodyne techniques. *Review of Scientific Instruments*, 2006.

[57] Shigehiko Tateno, Kei Hirose, Yasuo Ohishi, and Yoshiyuki Tatsumi. The structure of iron in earth's inner core. *Science*, 2010.

[58] K. Tsembelis, J. C. F. Millet, W. G. Proud, and J. E. Field. The shock hugoniot properties of cement paste up to 5 gpa. In *Shock Compression of Condensed Matter - 1999*.

[59] K. Tsembelis, W. G. Proud, G. R. Willmott, and D. L. A. Cross. The shock hugoniot properties of cement paste and mortar up to 18 gpa. In *Shock Compression of Condensed Matter - 2003*.

[60] Tracy J. Vogler, C. S. Alexander, J. L. Wise, and S. T. Montgomery. Dynamic behavior of tungsten carbide and alumina filled epoxy composites. *Journal of Aplied Physics*, 2010.

[61] Tracy J. Vogler, John P. Borg, and Dennis E. Grady. On the scaling of structured steady waves in heterogeneous materials. *Journal of Applied Physics*, 2012.

[62] Peter D. Washabaugh. *An Experimental Investigation of Mode-I Crack Tip Deformation*. PhD thesis, California Institute of Technology, 1990.

[63] Erin S. Williams, Stephen S. Graham, Paul A. Reed, and Todd S. Rushing. Laboratory characterization of cor-tuf concrete with and without steel fibers. Technical report, US Army Corps of Engineers Engineer research and Development Center, 2009.

[64] Shiming Zhuang, Guruswami Ravichandran, and Dennis E. Grady. An experimental investigation of shock wave propagation in periodically layered composites. *Journal of the Mechanics and Physics of Solids*, 2003.